OPEN ACCESS

University of BRISTOL

This electronic thesis or dissertation has been downloaded from Explore Bristol Research, http://research-information.bristol.ac.uk

Author:
Wood, Nick H

Title:
Hard Sphere Nucleation Rates

General rights
Access to the thesis is subject to the Creative Commons Attribution - NonCommercial-No Derivatives 4.0 International Public License. A copy of this may be found at https://creativecommons.org/licenses/by-nc-nd/4.0/legalcode This license sets out your rights and the restrictions that apply to your access to the thesis so it is important you read this before proceeding.

Take down policy
Some pages of this thesis may have been removed for copyright restrictions prior to having it been deposited in Explore Bristol Research. However, if you have discovered material within the thesis that you consider to be unlawful e.g. breaches of copyright (either yours or that of a third party) or any other law, including but not limited to those relating to patent, trademark, confidentiality, data protection, obscenity, defamation, libel, then please contact collections-metadata@bristol.ac.uk and include the following information in your message:

• Your contact details
• Bibliographic details for the item, including a URL
• An outline nature of the complaint

Your claim will be investigated and, where appropriate, the item in question will be removed from public view as soon as possible.

HARD SPHERE NUCLEATION RATES

NICHOLAS WOOD

A dissertation submitted to the University of Bristol in accordance with the requirements of the degree of Doctor of Philosophy in the Faculty of Science, School of Physics.

May 2019

40,347 Words

DECLARATION OF AUTHORSHIP

I declare that the work in this dissertation was carried out in accordance with the requirements of the University's Regulations and Code of Practice for Research Degree Programmes and that it has not been submitted for any other academic award. Except where indicated by specific reference in the text, the work is the candidate's own work. Work done in collaboration with, or with the assistance of, others, is indicated as such. Any views expressed in the dissertation are those of the author.

Signed: _____

Nicholas Wood

Date: _____

ABSTRACT

Chemistry is hard. Simulating the full quantum-chemical interactions involved in any complicated physical process is often impossible, due to the huge amount of computing power required. Instead, model systems which interact in simpler ways can be studied. The simplest model is known as the ideal gas. This model consists of point particles which only interact through elastic collisions. Even a model this abstract gives us the ideal gas law, one of the most prized equations in all of physical chemistry. Moving one step further in complexity, we can give the particles a diameter and prohibit them from overlapping. This is the hard sphere model. This extra step in complexity gives hard spheres a richer behaviour than the ideal gas. Hard spheres form the familiar liquid and solid phases, with a full thermodynamic transition between the two, just like real materials. This existence of the freezing transition has been known since the 1950s, and new simulation techniques have measured its speed (the nucleation rate). Ten years earlier, experiments on particles suspended in a solvent (colloids), had shown that the hard sphere model could be realised in experiment. However, the experimental nucleation rates disagreed spectacularly with the simulations, by up to 13 orders of magnitude. This discrepancy has been described as the second worst failure in physics.

In this thesis, we attempt to resolve the discrepancy. First, we examine the impact of the sedimentation in the experiments, and show that it can create a substantial change in the nucleation rates. Then we examine the density fluctuations in the experimental system. We demonstrate that they are significantly larger than in the simulations. A detailed investigation into the cause of the increased fluctuations is undertaken. We conclude that they are due to the particle tracking methods applied in studying colloids, revealing an important experimental limitation which has not been previously described. Finally, we develop a new method for studying nucleation rates using confocal microscopy, increasing the sample size by several orders of magnitude. This allows us to measure the most extended nucleation barriers ever seen experimentally. Unfortunately these barriers essentially agree with previous experiments, leading us to conclude that the nucleation rate discrepancy remains unresolved.

PUBLICATIONS

The full results of chapter three and the key results of chapter four have previously been published as:

N. Wood, J. Russo, F. Turci, C.P. Royall. "Coupling of sedimentation and liquid structure: Influence on hard sphere nucleation" *The Journal of Chemical Physics* **149** (2018) p. 204506

CONTENTS

LIST OF FIGURES

LIST OF TABLES

Part I

INTRODUCTION

1

LITERATURE REVIEW

1.1 HARD SPHERES

Hard spheres are the second simplest model for atoms. One step up in complexity from the point particles of the ideal gas, hard spheres add an excluded volume. They interact similarly to billiard balls, when they are not touching they do not interact, yet they are forbidden from overlapping. The potential is zero at all points $r \geqslant \sigma$, and goes to ∞ when $r = \sigma$. as shown in equation 1.1.

$$U_{HS}(r) = \begin{cases} \infty & r < \sigma \\ 0 & r \geqslant \sigma \end{cases} \tag{1.1}$$

Despite this incredible simplicity, the physics exhibited by hard spheres is rich[1]. Many model systems which include strongly repulsive short range forces can be approximated by the hard sphere system[2]. For example, the structure factor $S(\mathbf{k})$ of the Lennard-Jones model is very well approximated by hard spheres[3]. By finding an effective hard sphere packing fraction (Φ_{eff}) through matching the structure factors, the dynamics of many systems also collapse to that of hard spheres[4]. This "quasi universality" of hard spheres can be understood by thinking of the structure and dynamics of simple liquids as essentially determined by the packing of the molecules, determined by the strongly repulsive potential. Meanwhile the attractive interactions can be seen as providing a background potential that gives the liquid a cohesive energy but does not affect its structure[5].

1.1.1 Phase Diagram

The phase behaviour of hard spheres in completely determined by a single parameter, the packing fraction Φ. Φ can be expressed in terms of the number density n and the particle radius r as in equation 1.2

$$\Phi = \tfrac{4}{3}\pi r^3 n \tag{1.2}$$

This results in a simple one dimensional phase diagram. Hard spheres are a liquid below the freezing volume fraction, Φ_f. Above

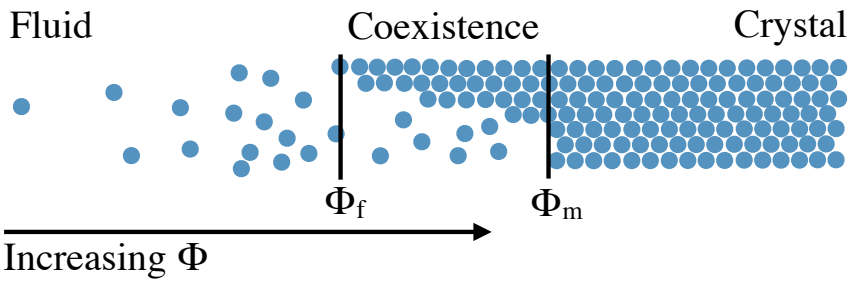

Figure 1.1: The equilibrium phase diagram of hard spheres. $\Phi_f = 0.491$ and $\Phi_m = 0.543$. This is the equilibrium phase diagram, but in fact at higher packing fractions the crystal forms only incredibly slowly, as the system has undergone vitrification.

this packing fraction, they undergo a first order phase transition to a crystalline state. They exhibit coexistence between a liquid and crystal phase for $\Phi_f < \Phi < \Phi_m$ and are fully crystal for $\Phi > \Phi_m$, where Φ_m is the melting volume fraction. The typical quoted values for Φ_f and Φ_m are 0.494 and 0.545, as determined by Hoover and Ree[6]. More recent simulation work, however has measured slightly lower coexistence lines, at about $\Phi_f = 0.491$ and $\Phi_m = 0.543$[7,8].

Above around $\Phi > 0.58$ hard spheres become glassy (if they avoid crystallisation)[9]. This transition to a glass is characterised by a rapid increase in the relaxation times and the formation of a disordered solid.

1.1.2 Crystallisation Mechanism

The first order phase transition to a crystal in hard spheres may initially seem counter-intuitive in the absence of any attractive forces. Most systems crystallise because the enthalpy gain from forming the crystal outweighs the decrease in entropy caused by forming the more ordered crystal. That is, $T(S_{Liquid} - S_{Solid}) < H_{Liquid} - H_{Solid}$. However, in the case of hard spheres, the potential energy is always zero, meaning the enthalpy cannot change upon crystallisation. Therefore, the hard sphere solid must have lower entropy than the liquid at the same volume fraction. At first sight, this seems impossible, as under the common interpretation of entropy as a measure of "disorder", the ordered crystal structure must have less entropy than the disordered liquid. However, the more accurate definition of entropy is related to the number of microstates which can correspond to the observed macrostate as $S = k_B \ln W$. Under this definition, the crystal can have more entropy if more microstates correspond to the crystal phase

than the liquid phase. That this is plausible can be seen from a simple argument related to the close packing volume fractions. For the FCC or HCP lattice $\Phi = 0.74$[10], whilst for random close packing $\Phi = 0.64$[11,12]. The RCP structure is jammed, the particles have no space in which to move and therefore the entropy, $S = 0$. If we imagine expanding the close-packed FCC or HCP lattice into a larger volume such that the volume fraction becomes $\Phi = 0.64$, the particles now have space to move and a finite entropy. We therefore expect an entropy-driven transition into the crystal lattice at some volume fraction below $\Phi = 0.64$[13].

Kirkwood predicted hard sphere freezing in 1953[14], but its existence proved controversial. In fact, even the papers which are now seen as decisive written by Alder and Wainwright[15] and Wood and Jacobson[16] were not enough for many. After the presentation of both sets of results at a conference in New Jersey in 1957, a show of hands of the attendees showed that half remained unconvinced that the transition was real[17]. Only later, after the results from Molecular Dynamics and Mote Carlo simulations had been completely reconciled, did the existence of the transition become uncontroversial.[18].

1.1.2.1 Classical Nucleation Theory

Simply cooling a liquid down past its freezing point does not result in instantaneous freezing. Water can be stored at $-10°C$ without crystallising into ice[19], for example. Water in this state is metastable, kinetically trapped in a thermodynamically unfavourable state[20]. This happens because there is a free energy barrier that the system must overcome before crystallising, caused by the surface energy of the nucleating droplet. In fact, all first order phase transitions must overcome an energy barrier[21].

Classical Nucleation Theory (CNT), was developed throughout the 1920s and 1930s. The original goal was to describe the condensation of the liquid phase from the vapour, but the theory can also be applied to the formation of the solid from the supercooled liquid. Indeed, some elements of CNT are used in almost every simulation of the nucleation of crystals[22].

The crucial assumption underlying CNT is *capillarity*[23]. Under this assumption, the nucleus is seen as a sphere, with the properties of the bulk crystal phase, surrounded by the bulk liquid, with a sharply defined interface between the two. This interface has a well defined surface energy, equal to the product of the planar interfacial tension between the two phases and the surface area of the cluster[23]. With the

capillarity assumption, the change in energy caused by the formation of a nucleus is given by equation 1.3.

$$\Delta G = 4\pi r^2\gamma - \frac{4\pi}{3}\rho_s r^3 \Delta\mu \tag{1.3}$$

Where r is the radius of the nucleus, $\Delta\mu$ is the chemical potential difference between the two phases and γ is the planar interfacial tension between the phases. For small values of r, the droplet energy is dominated by the r^2 term, and climbs rapidly with increasing r. For larger values, however, the r^3 term dominates, and the droplet energy begins to fall with increasing r. Between these two, there is a maximum crossover point, the energy of which which defines the energy barrier. The height of this barrier is given by equation 1.4[24].

$$\Delta G_{max} = \frac{16}{3}\frac{\pi\gamma^3}{\rho_s \Delta\mu^2} \tag{1.4}$$

The higher the barrier, the more rare a nucleation event will become. In fact the rate of nucleation events depends exponentially on the negative of the barrier height, as in equation 1.5[25,26].

$$I = \Gamma e^{-\beta \Delta G_{max}} \tag{1.5}$$

with Γ, the kinetic prefactor, describing the rate of growth of the nucleus[27].

1.1.2.2 Non-Classical Crystallisation

Classical Nucleation Theory has been successful in giving a general framework through which nucleation can be understood and analysed, but its predictions are difficult to test[28]. Where it has been tested, CNT has often been contradicted by experimental or simulation results. For example, capillarity suggests that the interfacial surface tension between the liquid and crystal nuclei should simply be equal to the bulk value, but simulation work shows the the surface tension increases with increasing supersaturation[29]. This effect can be recovered by considering that the interface is not a sharp distinction, but has a lengthscale over which the liquid and crystal are not completely distinct[30,31]. CNT also predicts that nuclei should lower their surface energy as much as possible by remaining compact spheres, but this has been contradicted by experimental work which found highly non-spherical critical nuclei[32]. Again, CNT can be extended to include these effects. For example, a version of CNT which included fluctuations of surface area can give highly non-spherical nuclei[33].

Another issue with CNT is the fact that it considers only a single reaction co-ordinate (the radius of the largest nucleus). This means that it is unable to capture more complex nucleation pathways, such as those which occur in two steps. Whilst CNT predicts that all the order parameters which change during nucleation do so at the same time, there is much evidence that the liquid first forms crystal precursors, from which the nuclei are generated. There is a great deal of literature exploring this two-step nucleation pathway for hard spheres, which can crudely be split into density-first and an order-first perspectives. "Density first" suggests that initially a high density region is formed, from which structurally ordered nuclei emerge[34], whilst "order first" suggests that the initial precursors are in fact no denser than the liquid, but instead have a high degree of crystal like bond orientational order, and these then become more dense[35,36]. It appears that there is now more support for the order-first perspective[28], but it also has been argued that to take a binary view of structure first or density first is misleading, and that the two-step process involves a complex interplay of both[37]. Either way, the notion that nucleation in hard spheres is a multistep process is now becoming widely accepted[38,39]

1.1.2.3 Density Functional Theory

Alternatively to CNT, a different formalism has been developed in Density Functional Theory (DFT)[40]. DFT overcomes the capillarity assumption that the crystal nuclei have a constant density equal to the bulk density of the crystal. Instead of choosing a single parameter, the radius of the nucleus, r, DFT considers the density profile $\rho(r)$. The free energy is then a functional dependent on the profile, and the critical nucleus size of CNT becomes a series of critical density profiles in DFT. These profiles are saddle points in the overall density-profile space which separate growing clusters and shrinking clusters[19]. It is then possible to determine rates by finding the free energy of the critical nucleus[23], and taking the kinetic prefactor from CNT. This has been done for the gas-liquid transition for a Yukawa attraction[41] and the Lennard-Jones potential[42,43], with results differing from CNT by up to 5 order of magnitude[23].

1.2 STRUCTURAL MEASUREMENTS

1.2.1 Radial Distribution Function

Liquids do not have a clear structure in the way crystals do. Instead spacially averaged quantities may are used. The most fundamental

of these is this pair correlation function, or $g(r)$. The $g(r)$ describes the likelihood of a particle being at a given distance, r, from a test particle at the origin. For a system of N particles, with potential energy $U_N(r_1, ..., r_N)$, the probability of a configuration in which the positions of n particles are found in positions $r_1, ..., r_n$ is given by equation 1.6[44].

$$P^{(n)}(r_1, ..., r_n) = \frac{1}{Z_N} \int ... \int e^{-\beta U_N} dr_{n+1} ... dr_N \tag{1.6}$$

Where Z_N is the normalising configurational integral, as in equation 1.7.

$$Z_N = \int ... \int e^{-\beta U_N} dr_1 ... dr_N \tag{1.7}$$

Assuming identical particles, we arrive at the n-particle density $\rho^{(n)}$.

$$\rho^{(n)}(r_1, ..., r_N) = \frac{N!}{(N-n)!} P^{(n)}(r_1, ..., r_n) \tag{1.8}$$

$\rho^{(1)}$ simply equals $\frac{N}{V} = \rho$ as expected (everything cancels with the configurational integral, aside from $\frac{1}{\int dr_1} = \frac{1}{V}$). For an ideal gas, the particles are uncorrelated, and so $\rho^{(2)}(r_1, r_2) = \rho^{(1)}(r_1)\rho^{(1)}(r_2) = N(N-1)/V^2 \approx \rho^2$.

We can now define $g(r_1, r_2) = \rho^{(2)}(r_1, r_2)/\rho^2$[45], the deviation from the ideal gas result. For an isotropic liquid, all that matters is the distance between r_1 and r_2, and so $g(r_1, r_2) = g(r)$. A schematic figure of a typical liquid structure and a $g(r)$ is shown in Fig. 1.2.

Calculating the radial distribution function involves solving the Ornstein–Zernike equation[46]. It is only in the case of hard spheres that the an exact analytic solution has been found[47], using the Percus-Yevick approximation[48,49].

1.2.2 Topological Cluster Classification

Whilst the radial distribution function and the static structure factor measure quantities averaged across an entire system, many analysis methods have been developed for measuring local structure. These include Voronoi analysis[50], common neighbour analysis[51], and bond orientation order[52]. This work uses the Topological Cluster Classification (TCC), developed by Stephen Williams and Alex Malins[53]. The TCC breaks systems down into a number of local structures, which correspond to minimum-energy structures for a given number

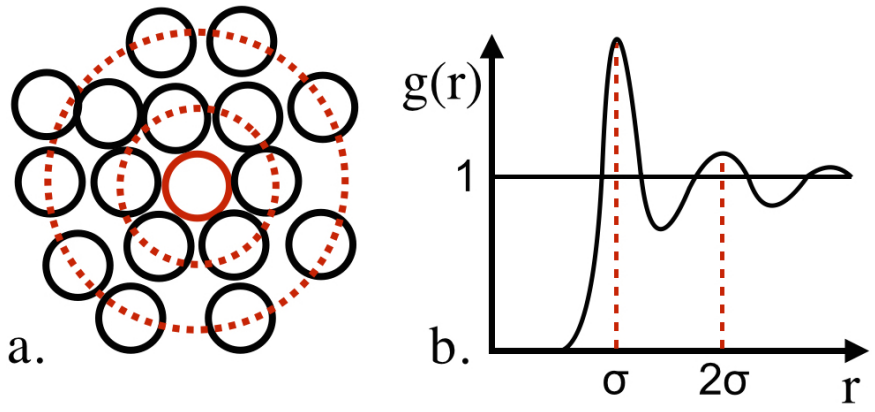

Figure 1.2: **a.** A typical liquid local structure around a test particle (red). Dashed red lines denote shells around the test particle at distances of σ and 2σ. **b.** An example radial distribution, showing the characteristic peaks at multiples of σ.

.

of particles (in isolation) for a variety of different potentials. These potentials include the Lennard-Jones potential, the Morse potential, the Wahnstrom and Kob-Anderson model glassformers, and the $N = 6$ minimum energy cluster from the Dzugutov model[53,54].

The algorithm begins with a modified Voronoi analysis to build a neighbour bond network. Each point of space is assigned to the nearest particle, creating Voronoi polyhedra around each particle. Particles are designated as neighbours if both their Voronoi polyhedra share a face and the centre-centre line between the particles intersects that face. The particles must also be closer than some cut off, here we use 1.4σ, and the results shown are not sensitive to changing this threshold.

This bond network is then broken down into the shortest path rings with 3, 4 and 5 members. By shortest path rings, we mean that the shortest path through the bond network between any two particles within the ring must be entirely contained within the ring[55]. A final parameter is introduced, the f_c parameter, which allows for some degree of asymmetry in the particularly sensitive 4-membered rings[56]. The TCC then proceeds to hierarchically identify gradually larger locally favoured structures from these precursor rings[54].

The TCC has been applied to a wide variety of problems, including glassformers[57], emulsions[58] and gels[59]. Most importantly for this work, the TCC has been used to study the hard sphere model. The TCC demonstrated the importance of five-fold symmetric local order on both the dynamic slowdown involved in vitrification[60], and in the suppression of crystallisation[61]. The TCC has also been used to help

match colloidal hard sphere experiments with simulation[62], which can otherwise be fiendishly difficult[63].

1.3 COLLOIDS

Insoluble particles suspended in a liquid without sedimenting are known as colloids. The entire mixture of colloid and solvent is often known as a colloidal suspension[64]. A colloidal suspension can be thought of as existing between solutions, in which molecules are dissolved in a solvent and will never settle, and suspensions, in which particles much larger than molecules are dispersed in a solvent but will eventually be dragged down by gravity[65]. Colloids are a very common form of matter, being found in nature (blood, milk) as well as in many artificial materials such as paints. Colloids are ultimately defined by their size, to remain in suspension they must be smaller than around $1\mu m$, and the minimum size considered colloidal is about $1nm$, but these length scales are somewhat arbitrary[66] . This length scale also determines the most important cause of their dynamics - Brownian motion.

1.3.1 Colloids as Model Systems

Colloids can be used as experimental model systems. This approach has a long history, starting with Jean Baptiste Perrin experimentally measuring the density of colloids as a function of their height in a container, and discovering the barometric distribution[67]. This distribution is also obeyed by gas molecules in an atmosphere - meaning that the much larger colloids are described by the same statistical physics as much smaller molecules[68]. The rigorous justification from the treatment of "colloids as atoms" comes from the solution theories of McMillan and Mayer[69] and Buff and Kirkwood[70].

Colloids have now been used to study many different phenomena including gels[71], glasses[72], liquid-liquid and crystal-crystal transitions[73] as well as many others. One of the first uses of colloids as a model for basic thermodynamic processes was Pusey and van Megen's mapping of the hard sphere phase diagram with PMMA colloids[74]. Subsequent to this, light scattering studies began to give a detailed picture of hard sphere crystallisation, beyond what was capable in simulation at that time (see section 1.4).

1.3.2 Colloidal Forces

1.3.2.1 Van der Waals Forces

The Van der Waals forces comprise a collection of several intermolecular, distance dependent forces. Van der Waals forces are attractive between particles made from materials of the same type, and are occasionally repulsive between particles made from different materials[75].

Van der Waals forces are not very important in the work described in this thesis. Generally, the steric stabilisation (see section 1.3.2.3) and electrostatic forces are enough to stop the colloids from getting close enough to feel the attraction[76]. Furthermore, the refractive index matching between the solvent and the particles substantially reduces the magnitude of the Van der Waals interactions.[77,78]

1.3.2.2 Electrostatic Forces

Colloidal dispersions inevitably feel some degree of electrostatic interaction. Colloids acquire surface charges due to chemical processes such as self-dissociation, where surface groups dissociate and ions pass into the solvent[79]. The charges on the surface then attract counterions, which form a double layer structure and screen the charge. The overall effect of this double layer force is captured in the Derjaguin, Landau, Verwey and Overbeek (DLVO) theory[80]. For low ion concentrations, as in non-aqueous solvents, it suffices to use the Debye-Hückel linearised equations[76,81], which results in a Yukawa potential, as in equation 1.9.

$$\beta U_{Yuk}(r) = \epsilon_{Yuk} \frac{e^{-\kappa(r-\sigma)}}{r/\sigma} \tag{1.9}$$

Where ϵ_{Yuk} is the contact potential, given in equation 1.10.

$$\epsilon_{Yuk} = \beta \frac{Z^2}{(1+\frac{\kappa\sigma}{2})^2} \frac{\lambda_B}{\sigma} \tag{1.10}$$

β is $\frac{1}{k_T}$, Z is the colloid charge, σ is the diameter of the particles, κ is the inverse Debye length and λ_B is the Bjerrum length, which represents the distance at which two particles have an interaction energy of $k_B T$. These final two properties are given by equations 1.11 and 1.12

$$\kappa = \sqrt{4\pi\lambda_B \rho_{ion}} \tag{1.11}$$

$$\lambda_B = \frac{e^2}{4\pi\epsilon_0\epsilon_r} \tag{1.12}$$

Where ρ_{ion} is the number density of monovalent ions, ϵ_0 is the permittivity of free space and ϵ_r is the solvent dielectric constant. Equation 1.11 shows that we can control the Debye length and therefore the length of the attraction by adding monovalent ions in the form of salt. Whilst the Debye length generally falls with increased salt, recent results have suggested that at high salt concentrations equation 1.11 can break down, and this relationship becomes inverted[82].

Given the above equations, almost every parameter is known either a known constant, can be found in the literature (ϵ_r), or can easily be measured (σ, ρ_{ion}). Only Z remains. Z can be measured using electrophoresis[83], and results show that it can very wildly over particle synthesis, time, and solvent batch[84]. In the absence of detailed electrophoresis measurements, a rough rule of thumb estimation for the colloid charge is $Z\lambda_B/\sigma = 6$[76].

1.3.2.3 Steric Forces

Colloids can be stabilised using steric forces. This is done by grafting polymer chains to the surface of the colloidal particles. When the particles approach each other, their chains eventually make contact, increasing the local polymer density in the contacting region. This creates a repulsive force, both through the increase in the osmotic pressure in the overlap region, and through the decrease in the configurational entropy of the polymer chains[85]. This interaction creates very high repulsions at lengths on the range on nanometers[86], and so can be used to model the sharp hard sphere potential, so long as there are no other contributions to the potential[74].

1.4 NUCLEATION RATE DENSITY - THE DISCREPANCY

Hard spheres are known to crystallise at the volume fractions shown in Fig.1.1. This is an equilibrium phase diagram, but a very interesting property is the *nucleation rate density*, which measures the rate at which the system falls into the crystal equilibrium phase from the non-equilibrium liquid. This quantity can be understood as the number of nuclei above the critical size which form per unit volume per unit time[87]. The nucleation rate density in hard spheres has been measured using both experimental scattering techniques, and a variety of simulation techniques.

1.4.1 Scattering Methods

The time and length scales inherent in colloidal suspensions makes them ideal for study with light scattering techniques[88]. Since the early 90s, much light scattering data has been taken on the nucleation of hard sphere colloids[89–93]. The light scattering techniques employed are Bragg Scattering (BS) and Small Angle Light Scattering (SALS). BS occurs at large angles and is due to scattering from crystal planes, whilst SALS measures long wavelength density fluctuations at very small angles[94]. In order to measure the nucleation rate, the necessary quantities are $X(t)$, the crystallinity of the sample at time t, and $R(t)$, the average radius of the crystallites at time t. From these the nucleation rate density can be found as $J = X(t)/\frac{4}{3}\pi R(t)^3 t$. $X(t)$ and $R(t)$ can be measured independently by BS and SALS[91].

Focussing first on BS, the experimental measurement is the intensity of scattered laser light $I(q,t)$ at a wavevector q and at time t after it passes through a refractive-index matched colloidal dispersion. The static structure factor $S(q,t)$ is then given by $S(q,t) \propto I(q,t)/P(q)$[95], where $P(q)$ is the single particle form factor. This can be measured as the intensity at very low dilution (where $S(q) = 1$)[93,95]. In the case where refractive index matching[92] or solvent leeching[96], precludes the accurate measurement of the form factor, it can instead be estimated by dividing the intensity profile either by the known Percus-Yevick liquid structure factor at the relevant volume fraction[92], or simply by an early measurement of the intensity profile (although this will limit later calculation of the crystal structure factor)[96]. The crystal structure factor $S_c(q,t)$ is found by subtracting the liquid structure factor S_l, which it is presumed to be equal to the earliest measurement of the overall structure factor $S(q,0)$, before any nuclei were formed. The average crystal size is then related to the width of the Bragg peak at half its maximum height, and the crystallinity to the area under the peak[92,96].

SALS, meanwhile, probes intermediate length scales of tens to hundreds of microns[97]. Ackerson and Schatzel[89] first used SALS to ring patterns related to the depletion zone around forming crystal nuclei. The intensity pattern is SALS is normalised by the the peak intensity $(I(q_m)$, and the average radius is given by $1.8148/q_{\frac{1}{2}}(t)$[96], where $q_{\frac{1}{2}}(t)$ is the scattering wavevector at half the maximum intensity. Average radii measured by SALS agree reasonably well, with the BS results although SALS radii can be larger by up to a factor of 2[91,96].

1.4.2 Simulation Techniques

Standard simulation techniques can be used to probe the nucleation free energy barrier[98]. For example, a brute force molecular dynamics simulation (MD) of supercooled hard spheres will eventually see the formation of a crystal nucleus[22], as will a Brownian dynamics simulation[99]. However, the key issue for conventional techniques is that at low-moderate supercooling, the nucleation barrier becomes very high, and the formation of a critical nucleus becomes correspondingly rare[100,101]. Enhanced techniques are therefore needed.

1.4.2.1 Umbrella Sampling

The traditional Monte-Carlo simulation approach is to sample phase space, with the chance a particular configuration is sampled related to its Boltzmann factor. For rare events like crystal nucleation at low supercooling, the issue is that configurations with very low Boltzmann weights contribute strongly to the ensemble average of the quantity of interest, the cluster size distribution in the case of nucleation[99,102,103]. However, the system can be biased to explore these configurations by changing the weighting function to use a different potential, the bias potential. For nucleation, the biasing potential used is related to the size of the largest cluster $n(r^N)$ as $\omega[n(r^N)] = \frac{1}{2}k_n[n(r^N) - n_0]^2$[103,104]. The simulation then samples a window of cluster sizes with width k_n, centred around a cluster of size n_0. By taking many windows of increasingly larger clusters, the nucleation barrier can be fully measured to high precision[99,105].

1.4.2.2 Forward Flux Sampling

Forward flux sampling was introduced in 1995 by Allen *et al.*[106]. The strategy for measuring rare events involves drawing interfaces in phase space which correspond to increasing values of some reaction co-ordinate[107,108] (in the case of nucleation, the size of the largest cluster is usually chosen[109]). The difference in the reaction co-ordinate between two sequential interfaces is chosen such that a transition from one to the next is not a rare event, and the probability of the transition can then be readily measured. The probability of transitioning from the liquid to the critical cluster size is then simply the product of the probabilities of every transition between the reaction co-ordinate values[99].

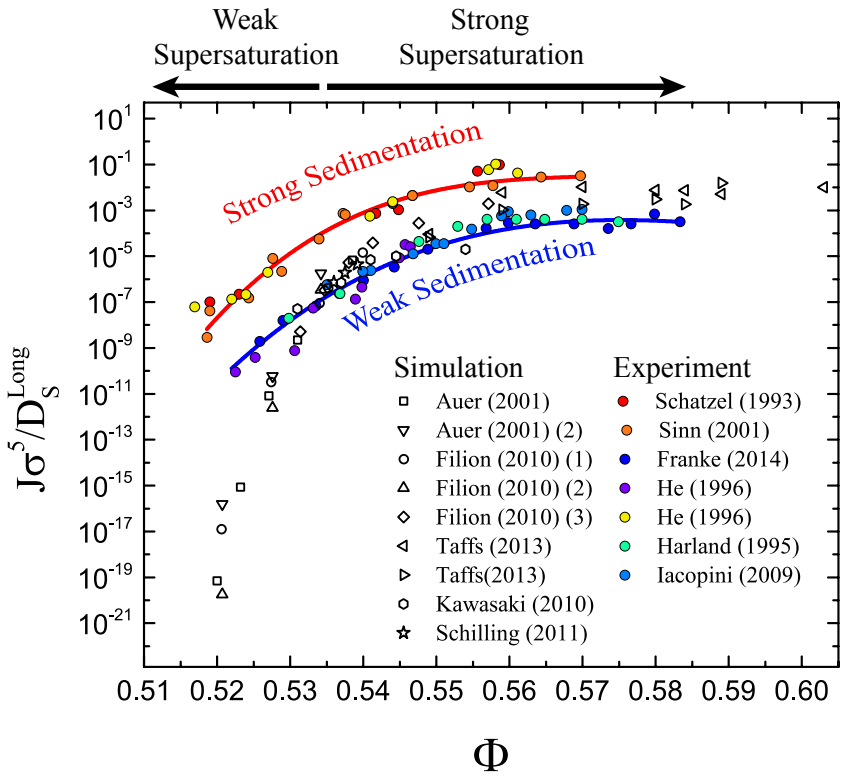

Figure 1.3: The nucleation rate density of hard spheres, across the literature. Shown in coloured points is the experimental data, all taken from scattering experiments. Shown in white points is simulation work, which uses umbrella sampling, forward flux sampling and brute force brownian simulations. The experimental data can be split into two regimes, the first with Péclet numbers of around 0.2 nucleate very quickly,[89–91] (shown in red-yellow), the second have a Péclet number of around 0.01[90,92,93](shown in blue-purple). Simulation data can be found at Refs.[35,62,99,105,110,111].

.

1.4.3 Literature Measurements

Shown in Fig 1.3 are the current literature results for nucleation rate densities of hard spheres. It can be seen that in the less deeply supercooled regime, close the the freezing line, a very large gap opens up between simulation calculations and the experimental measurements. At the lowest volume fraction reached by experiments, $\Phi = 0.52$, this gap is over 10 orders of magnitude, described as the second worst disagreement between experiment and theoretical prediction in physics[112].

1.4.4 Comparing Rates

When using SI units, different experiments will nucleate at different rates. This is due to the relative speeds of the experiments being scaled by the size of the particles, the viscosity of the solvent and other experimental parameters. In order to compare across experiments, and between experiments and simulation, a reduced dimensionless nucleation rate density is used[88]. This is given by equation 1.13.

$$J^* = \frac{J\sigma^5}{D_0} \tag{1.13}$$

D_0 is given in units of m^2s^{-1}. Therefore the scaling factor $\frac{\sigma^5}{D_0}$ is in units of m^3s. Multiplying through by the nucleation rate density, units $m^{-3}s^{-1}$ therefore returns a dimensionless number.

Choices of the relevant diffusion coefficient differ. Early work chose the diffusion coefficient at infinite dilution[105]. Later work, however, moved to the long time self diffusion coefficient[111], which scales the diffusion constant as equation 1.14.

$$D_L = D_0(1 - \Phi/\Phi_{Glass})^\nu \tag{1.14}$$

Where the experimental glass transition occurs at $\Phi_{Glass} = 0.58$ and with $\nu = 2.6$. This value of ν comes from the mode coupling prediction which fits the experimental data well[113]. It should be noted that the choice of diffusion coefficient does not effect the discrepancy between simulation and experiments, as both are affected by the shift in the diffusion constant.

1.5 POSSIBLE EXPLANATIONS

1.5.1 Softness

There is some possibility that the experimental potentials are not the same as those in simulation, and this might be affecting the rates. Importantly, the experiments are almost certain to be softer than the experiments. The PHSA layer which gives the hard steric repulsion is characterised by a length scale over which the repulsion increases. Measurements of the repulsion using surface force apparatus find that this length scale is around 15-20nm[86]. This is a small but appreciable softness, especially for the smallest experimental systems in Figure 1.3, for which it is around 0.05σ[90].

There are several problems with the potential as a potential explanation for the discrepancy, however. Firstly, the particles which should have the most soft potential are those which are smallest - the PHSA chains are longer relative to their diameter. Moreover, any residual repulsion caused by charge should also affect smaller particles more as, for smaller particles, the Debye length is larger relative to the diameter of the particles. This means smaller particles should exhibit a larger nucleation rate density discrepancy - but in fact the opposite is true, the smaller particles tend to agree with simulations better than experiment. A second issue with this explanation is that small pertubations to the potential seem to make only a small difference to the nucleation rates. Whilst the first simulations with a nearly hard sphere potential (the Weeks Chandler Anderson potential) showed a sharp increase in the nucleation rates relative to hard spheres[35], later work corrected this finding, showing very little difference between the WCA nucleation rates and those of hard spheres, for several different simulation methods[99]. In fact the original WCA prediction was later corrected due to an error in the calculated volume fractions[110].

Auer *et al.*[114] also checked for the effect of the steric stabilisation. They matched the measured freezing and melting lines of Pusey and van Megen[74] with those calculated for a PSHA-stabilised system and found that the required repulsion was a longer ranged by a factor of two to three than than had previously been measured[115,116]. They concluded that the discrepancy was likely due to charging, but when simulating systems with the new longer ranged potential, found only a modest 1-2 orders of magnitude increase in the nucleation rate densities.

1.5.2 Hydrodynamics

A substantial difference between experiment and simulation of hard spheres is that in experiment the colloids are suspended in a solvent, whilst the simulations have no solvent. This means that there will be some degree of hydrodynamic interactions in the experiments which are not present in the simulations[117]. The interactions themselves can expressed with the mobility tensors of Oseen, which finds the induced velocity at a distance from a moving particle, and of Rotne-Prager[118], which extends this result to two particles[119]. Describing the behaviour of more particles is possible using the Rotne-Prager-Yamakawa approximation, but this assumes pairwise interactions, ignoring the complex multi-particle interactions[120]. Both the Oseen and Rotne-Prager tensors show a decay in the induced velocity which

falls off as $\frac{1}{r}$ - a long ranged interaction which is completely missing from most simulation work.

The role of hydrodynamics in hard sphere crystal nucleation has been directly studied by Schilling and Radu[121]. This work used multi-particle collision dynamics to simulate an explicit solvent and event driven molecular dynamics for the particle dynamics. The nucleation rate was found by measuring the average induction time of a large crystal cluster (80 particles). In order to study the effect of the hydrodynamics, the solvent viscosity was tuned. Crucially, the nucleation rate density did not scale with the inverse of the viscosity, as would be expected if the viscosity were simply reducing the diffusion constant. In fact, at high viscosities the nucleation rate declined less than would be expected. When the diffusion constant is measured and scaled out, this corresponds to an increase in the nucleation rate density caused by the solvent viscosity of up to one order of magnitude. The effect of the viscosity increased with decreasing packing fraction, which is in the correct direction for explaining the nucleation rate gap, which also grows with decreasing packing fraction. This work did not reach the deeply supercooled regime where the discrepancy becomes huge, and so there is some possibility that the influence of hydrodynamics could grow large enough to explain the gap. However, later in the work it is demonstrated that the hydrodynamics make little difference to the structure of the nuclei, and therefore the effect of the hydrodynamics appears to be constrained to the kinetic prefactor, not the nucleation barrier. This would mean that the hydrodynamics would have to change the dynamics of the colloidal systems by many orders of magnitude to be explanatory. Whilst the kinetic prefactors determined in experiments are known to disagree with simulation[122], the disagreement is not this large.

1.5.3 Polydispersity

Polydispersity, the tendency for collections of particles to not be all of perfectly the same size, has been discussed as a potential explanation of the nucleation rate density gap[88]. The polydispersity of a sample is defined as the standard deviation of the particle diameters divided by the mean particle diameter[123], assuming a normal diameter distribution. Polydispersity could change the nucleation rates in two ways. Firstly, polydispersity could be changing the positions of the coexistence lines, leading to incorrect volume fractions. We discuss this possibility in section 1.5.5.1. Secondly, the polydispersity could be altering the nucleation barriers themselves.

However, the experimental data seems to contradict this. The data which disagrees most with simulation is taken with particle systems of relatively low polydispersities - Schatzel *et al.*[89] has $s = 0.05$, He *et al.*[90] has $s = 0.05$ and Sinn *et al.*[91] has $s = 0.045$. Meanwhile, the experiments which have better agreement with simulations have similar or higher polydispersities. Iacopini*et al.*[93] has $s = 0.065$, Harland *et al.*[92] has $s = 0.05$ and the smaller He *et al.*[90] data has $s = 0.05$. Therefore, when it comes to polydisperisty, the experiments that model the monodisperse hard spheres of simulation the worst tend to agree with those simulations better, whilst the "best" experiments agree more poorly. This appears to make polydispersity an unpromising avenue for explaining the gap. Furthermore, as discussed in Section 1.5.5.1, simulation work shows that polydispersity tends to make little difference to the nucleation rates, once the volume fractions are correctly scaled. If polydispersity were to play a role, it would therefore need to be coupling to some other property of the experiments.

1.5.4 Sedimentation

A further aspect of experiments which is not included in the biased Monte Carlo simulations is the sedimentation of the colloidal particles. The colloids are made of a different material to the solvent, meaning there is a density mismatch between the two. This density mismatch means the particles have an effective weight, and will undergo some degree of sedimentation. This effect is especially pronounced in earlier experimental work, which used quite large PMMA particles (around $1\mu m$ in diameter) in tetralin/decalin solvent mixtures[89–91]. The solvent composition is tuned to give a good refractive index match, which lowers the likelihood of multiple scattering events which hinder the interpretation of the data[124]. However, tuning for a good refractive index match ignores the density matching. Taking the proportions given by He *et al.* which have a 46% tetralin 54% tetralin mix (by weight) results in a final solvent density of $0.93 g cm^{-1}$, in comparison with the density of PMMA of $1.18 g cm^{-1}$[125]. More recent work[90,92,93] used either smaller PMMA particles[91,92] which are less affected by sedimentation (around $0.5\mu m$ in diameter), or polystyrene microgels. These microgels use ethyl-naphthalene as a solvent, which matches the refractive index very well and gives a reasonable density match ($\rho_{EN} = 0.992 g cm^{-1}, \rho_{PS} = 1.05 g cm^{-1}$). This density match is improved further by the microgel particles swelling in the solvent[126] down to a density of $\rho_{Part} = 1.01 g cm^{-1}$.

1.5.4.1 The Péclet number

The sedimentation of colloids can be characterised by their Péclet number, which is the ratio of the time a particle takes to diffuse its radius and the time it takes to sediment its radius. The time to diffuse a radius a is given by equation 1.15, using the Stokes - Einstein form of the diffusion coefficient, D_0[66].

$$t_d = a^2/D_0 = 6\pi\mu_f a^3/k_B T \tag{1.15}$$

Where a is the particle radius, μ_f is the dynamic viscosity of the liquid, and $k_B T$ is the thermal energy. The time to sediment a radius is given by the time taken for a particle to move a radius whilst travelling at the Stokes velocity given in Equation 1.16,

$$v_s = \frac{2a^2\Delta\rho g}{9\mu_f} \tag{1.16}$$

Where $\Delta\rho$ is the difference in density between the colloid and the solvent. The Péclet number then reads as in Equation 1.17.

$$Pe = \frac{t_d}{t_s} = \frac{12\pi g\Delta\rho a^4}{9k_B T} \tag{1.17}$$

We therefore expect that in the regime where Pe « 1, diffusion dominates and determines the structure of the liquids, whereas at Pe » 1, sedimentation will dominate. The above equations are valid in the regime of low Reynolds number, which for colloidal dispersions of the type studied in this thesis ($\sigma < 100\mu m$) is a reasonable assumption[127].

Table 1.1 shows the literature experiments, alongside their Péclet numbers and nucleation rate density discrepancy. The two set of experiment sort into two fairly distinct groups, the first have high Péclet numbers (around 0.2) and also very high discrepancies, of 10-12 order of magnitude. The second group are the experiments with low Péclet numbers (around 0.01) and smaller discrepancies, of around 3-6 orders of magnitude. The Péclet number is the only experimental parameter which splits the experimental data into the two clear discrepancy groups, with no exceptions.

1.5.4.2 Literature Work on Sedimentation

Studying the effects of sedimentation therefore appears to be a very promising route to take to understand the discrepancy. Some work has explored this aspect of the problem. Russo *et al.* (2013)[112] use simulations to probe the effects of sedimentation on the nucleation rate.

Table 1.1: Experimental systems previously used in the literature. The crucial parameter for sedimentation is the Péclet number, which measures the relative importance of sedimentation and Brownian effects. The final column shows the discrepancy in the nucleation rate density from the simulation values for each experiment. Unless otherwise stated the discrepancy shown is that reported at $\Phi = 0.52$. Otherwise we take the nearest data point. Work with a "not applicable" discrepancy have no data points which reach the regime where the discrepancy emerges.

Author	Citation	Minimum phi	Péclet Number	Discrepancy (10^x)
Schatzel (1993)	[89]	0.52	0.1868	12
Sinn (2001)	[91]	0.518	0.179	10
He (1996)	[90]	0.517	0.1723	12
He (1996)	[90]	0.522	0.0075	6
Harland (1997)	[92]	0.53	0.006	3 ($\Phi = 0.53$)
Iacopini (2009)	[93]	0.535	0.018	n/a
Franke (2014)	[128]	0.525	0.009	3 ($\Phi = 0.53$)
Taffs (2013)	[62]	0.54	0.001[81]	n/a

This work uses Brownian dynamics simulations and the nearly hard sphere WCA potential. The work uses periodic boundary conditions in the dimensions perpendicular to the applied gravitational field, and places hard walls made of a frozen liquid equilibrium configuration at the top and bottom of the box. The result of this work is that nucleation is sped up dramatically in the presence of sedimentation, enough to completely resolve the discrepancy. The mechanism for this acceleration is a substantial density profile created by the gravitational field. The density profile means that towards the bottom of the low Φ simulations exist regions at a much higher volume fraction. Nucleation then proceeds highly preferentially from these regions. In fact, even a small region of liquid at around $\Phi = 0.55$ is enough to almost completely dominate the nucleation rate density, given how much lower the nucleation barrier is in these regions.

It seems unlikely that the situation described in this work explains the speed of nucleation of the experiments, for several reasons. Firstly, whilst the authors choose to measure the effect of the equilibrium sedimentation profile, it is far from clear that this is reached in the experiments. Before readings are taken by small angle light scattering, the samples are shear melted, destroying any existing sedimentation profile. From here, the particles will take a long time to settle to their

equilibrium profile. For example, Schatzel[89] quotes a free particle sedimentation speed of around 0.1mm/h. This will be lowered by hydrodynamic effects. The extent is captured in the Richardson-Zaki law, $v_s/v_s^0 = (1-\Phi)^n$ with $n \approx 6.6$[129], which applies even down to low Péclet numbers[130]. The Richardson-Zaki law predicts a reduction in the sedimentation speed at a volume fraction of 0.52 of around a factor of 100. Meanwhile, the time scale of crystallisation in these experiments is quoted as 10^3s. Therefore, within the time scale of the experiments the particles will have sedimented by only a few diameters. The samples themselves are on the order of centimeters in length (for example those used by Sinn[91] are 20mm by 10mm by 5mm), so there is not enough time for the mass transport required to generate the equilibrium density profiles.

Secondly, the simulations are taken at a relatively high Péclet number, 0.32, and so the equilibrium profiles that exist in the scattering experiments will be less pronounced than those in the simulations. Only a small change in the profile is enough to completely change the likely result, the difference between a profile having a maximum $\Phi = 0.53$ or $\Phi = 0.54$ will be enough to change the nucleation rate by around five orders of magnitude. However it should be noted that this discrepancy between the Péclet numbers used by Russo *et al.* and those quoted here could be due to choices made in their calculation, such as choosing a or σ as the relevant length scale.

Finally, even if the equilibrium sedimentation profile were reached, and it was large enough to explain the nucleation rate, it should have been noticed in the scattering experiments. Unlike the simulations, the entire scattering cell is not measured, only the section of the cell in the path of the beam contributes to the signal. Generally, this means that less than one third of the height of the cell is included (although the exact details of the set up can be hard to find in the original papers, but see the methods section of Harland[92] and Iacopini[131]). This means that the entire profile will not be seen by the scattering, only a small section. There are then two possibilities, either the laser is focussed at the very bottom of the sample (quite unlikely, as this risks the beam missing the sample), in which case the bottom of the profile is measured, and the deviation from the bulk volume fraction should be noticed in the structure factor. Alternatively, the laser is focussed somewhere closer to the centre of the sample and therefore is in fact looking at a liquid with a much closer density to the prepared density, which should not nucleate especially quickly. It's possible that nuclei from the bottom of the sample could grow sufficiently to enter the

laser path, but the emergence of only a few very large nuclei would be noticed in a sudden increase in the average crystallite size.

The second piece of work which examined sedimentation is that of Ketzetzi *et al.* (2018)[132]. This work used confocal microscopy and relatively large PMMA spheres of diameter 2μm, sedimenting with Péclet number 0.9. The authors found that sedimenting samples tended to nucleate faster than density matched samples. However, the sedimentation is studied in a similar way to that of Russo *et al.* (2013), in that there exists a strong density profile. In the confocal experiments, the image box is only a small fraction of the sample size, and so only a part of the profile is seen. It appears that the region imaged is towards the bottom of the sample, as the average volume fraction in the sample climbs throughout the experiment. In fact, the sedimentation is so pronounced that a sample prepared at $\Phi = 0.54$ finishes with an average density of around $\Phi = 0.60$. This settling process is likely to be dominating the nucleation rates, hence why only a very small change is seen in the measured nucleation rates with decreasing volume fraction, even all the way down to $\Phi = 0.52$.

In fact, the authors argue against the conclusions of Russo *et al.* (2013), who show that their nuclei preferentially emerge from regions of high local volume fraction. Ketzetzi *et al.* measure the size distribution of nuclei at different *local* volume fractions and show that they collapse onto each other. This also means that the nucleation barriers for every region of every sample they study are essentially the same, disagreeing with simulations which predict a strong Φ dependence. The nuclei are therefore just as likely to emerge from a region that has a low volume fraction as from a region that has a high volume fraction. This seems very surprising - essentially this means that particles forming nuclei must be affected by the average volume fraction of the entire sample, which may vary over the scale of hundreds of diameters, rather than the local region with which particles have some degree of positional correlation. In fact it is likely that this analysis does not warrant this conclusion, as the local volume fraction appears to be determined *after* the formation of the nuclei. The collapse of size distribution in fact shows that the local volume fraction of the liquid is not influenced by the presence of a nucleus, not *vice versa*. It could be argued that the local volume fraction after the emergence of the nucleus should correlate well with the volume fraction prior to the emergence, but as the authors wish to rule out the role of transitory density fluctuations, this does not seem clear. It should also be noted that the analysis is very susceptible to small errors - results past nuclei sizes of 10 particles invariably rely on the existence of just a single

cluster, and lower nuclei sizes also rely on small samples. For example, for $n = 5$, the 0.58 curve would agree well with the simulation barrier if 15 nuclei had been measured rather than the 8 that were seen. These numbers will be very sensitive to choices made in, for example, the cutoffs used to determine nuclei, or the distance chosen to determine the local volume fraction. As such, whilst the results in Ketzetzi *et al.* are intriguing, further work is necessary to fully understand the role of sedimentation in hard sphere nucleation.

1.5.5 Accuracy of Volume Fractions

Whilst most work has focussed on understanding possible errors in the y-axis of Figure 1.3, errors in the x-axis could also play a part. Measuring accurate volume fractions can be very difficult[76], and the difference in nucleation rate densities between experiments and simulations appears to be a matter of a few percent in the volume fraction.

1.5.5.1 Choosing the Correct Freezing Line

Pusey *et al.*[133] say that an error in the original Auer and Frenkel paper[105] which first demonstrated the nucleation rate gap is the explanation for the discrepancy. Auer and Frenkel took the experimental nucleation rates directly from Schatzel's 1993 work[89], which scaled the volume fractions to $\Phi_F = 0.494$. However, later work determined that the freezing line for hard spheres with a polydispersity of 0.05, as in the Schatzel work, is in fact rather higher[134]. In the words of Pusey *et al.*:

"...experimental volume fractions were calculated assuming freezing to occur at $\Phi_F = 0.494$, the value for a monodisperse system. In fact ... the appropriate value for s = 0.05 is $\Phi_F = 0.508$. Thus ... all the experimental data should be shifted to higher volume fractions by the factor 0.508/0.494 = 1.028. This operation leads to quite reasonable agreement between experiment and theory for s = 0.05".[133]

Given this claim, we need to examine the experimental procedure used in the literature experiments to measure the volume fraction. Scattering work like that of Schatzel[89], due to a variety of systematic errors on the volume fraction, finds measured volume fractions which do not match the true phase behaviour of hard spheres. As such, they simply rescale their volume fractions. This is done by following Ackerson and Paulin[135] sedimentation experiments, which measure the crystallinity of a sample at a particular volume fraction. By measuring the crystallinity of each of their samples, and linearly interpolating

down to the highest value of Φ which would give zero crystal, the freezing line ($\Phi_{f(meas)}$) is measured. Then all volume fractions are rescaled by the factor $\frac{\Phi_{f=0.494}}{f_{meas}}$ to arrive at the given volume fractions. Pusey's argument is that this value of 0.494 is incorrect, and should be 0.508. This argument applied to the original Auer and Frenkel work, but the argument itself would also apply to all future work on the nucleation rate problem. The result of this argument is to shift all the experimental data in Fig. 1.3 by 3% of the volume fraction, which would result in an excellent agreement.

The scaled volume fractions, however, are important because they can be used to compare the *distance from the phase boundary* of a given sample. Experiments can never truly model hard spheres, there will always be experimental imperfections. If we were to measure systems at the same true volume fraction, we would see that the polydisperse experiments nucleate very slowly, or not at all, relative to the simulations. This is simply due to the fact that, at a given volume fraction, the polydisperse experiments are more supercooled than the simulations relative to their freezing line. A more reasonable comparison would be to compare the experiments and simulations at a given distance from their freezing line. By measuring the freezing line of their systems and rescaling their volume fractions such that the measured freezing line matches the hard sphere freezing line, the experimentalists achieve this. Their quoted volume fractions are "effective" hard sphere volume fractions.

There are some caveats to this procedure however. It assumes that the effect of polydispersity is to simply rescale the volume fractions of hard spheres,without making a difference to the nucleation process itself. At some level of polydispersity, this assumption must break down, as highly polydisperse systems fail to nucleate at all. We need a test to know when a polydisperse system can be reasonably compared to a monodisperse system after a simple volume fraction rescale. A sensible test is whether, in simulation, hard spheres at a given polydispersity nucleate at the same rate as monodisperse hard spheres, after the appropriate scaling. For the experimental polydispersities this does appear to be the case, as the original Auer and Frenkel work also plotted the rate curve for an unscaled polydisperse system, which is almost exactly the same as the monodisperse curve scaled by the factor 1.028. After scaling, this polydisperse nucleation curve would agree very well with the monodisperse system. Indeed, the Pusey paper[133] itself demonstrates this - in Figure 5c the nucleation curves for a variety of polydispersities (up to 0.06) are shown to collapse onto a master curve when the volume fractions are scaled by the

distance from the freezing line. We can therefore be confident that the rescaling procedure performed in the scattering work results in a fair comparison between the polydisperse systems they study and the monodisperse simulations. The discrepancy persists.

1.5.5.2 Statistical Uncertainty in the Volume Fraction

The difficulties of determining the correct volume fraction in experiments are profound[76]. The random error on the volume fraction in Fig. 1.3 is likely to be at least ± 0.004[88]. This means that the experimental data could all lie within a reasonable error of the simulation predictions. Indeed, Schilling *et al.*[111] state "the previously observed discrepancy between simulation and experiment does not necessarily imply 'missing physics'. It can be explained by uncertainties and statistical errors."

It appears, however, that whilst errors in the volume fraction may well explain part of the gap, they do not explain all of it. Whilst there is random error associated with each set of data of around ± 0.004, all of the experimental data is systematically offset from the simulations in one direction. If discrepancies were due to errors in measuring the volume fractions, we would expect some data to nucleate more quickly than the simulations, and other data to nucleate more slowly. Furthermore, the experimental work of He (1996)[90] uses two PMMA species of different sizes, and measures two quite different nucleation rates. However, the synthesis method and materials, characterisation technique, and nucleation measurement method were identical for these two different species. Any systematic error on the volume fraction should therefore be equal between these two sets of particles, and yet one set nucleated 10^3 times faster than the other.

Filion *et al.*[99] also examine the claim that statistical error may explain the gap. They point out that "the very large discrepancy between experimental and numerical nucleation rates at lower densities cannot be accounted for by a simple rescaling of the density axis." That is, the behaviour of the experiments is *qualitatively* different rather than merely quantitatively different. This can be seen clearly by examining the slopes of the nucleation rate curves. The simulation work very rapidly dives to incredibly small nucleation rate densities at low supercooling, whereas the experimental curves are much shallower.

2

EXPERIMENTAL TECHNIQUES

2.1 OVERVIEW

This section will introduce and explain the experimental and analysis techniques used throughout the results chapters. The majority of experimental work involves the preparation and analysis of PMMA confocal experiments.

2.2 EXPERIMENTAL SYSTEM

Throughout this work we make use of a PMMA colloidal model system originally developed by Yethiraj and van Blaaderen[136]. This system uses a mix cis-decalin and cyclohexyl bromide, the composition of which can be tuned to provide both density matching and refractive index matching. The refractive index matching ensures that attractive Van der Waals forces are minimised[77,78]. The particles are sterically stabilised using short chains of PHSA[137], which gives a short ranged hard interaction over a length scale of just a few nanometers[86]. However, these are both low dieletric constant solvents ($\eta_r(cis-decalin) = 2.21$[138], $\eta_r(\mathrm{CHB}) = 7.9$[139]), and so there is a substantial degree of charging present[76]. This charging can be controlled through the addition of the salt tetrabutyl ammonium bromide (TBAB), which screens the charge, and gives a reasonable approximation to hard sphere behaviour[76,136]. However, as the charge is not screened perfectly, the effective hard sphere diameters of the colloids will be slightly larger than just their diameter added to the length of the steric screening. As volume fractions depend on the radius cubed, it is therefore important to carefully measure the true volume fractions of the system, for example by measuring the coexistence lines.

2.3 SOLVENT PREPARATION

CHB is prepared with 4mM of salt to screen out charge. Generally this is prepared by adding 0.0048g of Tetrabutylammonium bromide (TBAB) to 5 g of CHB. This is a supersaturated solution, so the mixture is left to sit for several days in a water bath at $40^{\circ}\cdot$C. The solvent is

removed from the water bath only when there are no visible signs of salt flakes remaining in the vial.

2.4 DENSITY MATCHING

Generally our colloidal particles are stored in a single component solvent, cis-decalin. To density match the solvent to the particles, they are centrifuged with an Eppendorf 5415r Centrifuge at 13400 RPM (relative centrifugal force $\approx 10^4 g$) for around 10 minutes, after which time they have formed a sediment which will be at $\Phi = 0.64$ to good approximation[140,141]. The supernatant is withdrawn with a series of pipettes of decreasing capacity, 1ml, followed by 100µl followed by 10µl. This ensures that almost all supernatant is withdrawn. The eppendorf is then weighed, and the weight of the pellet is calculated by subtracting the initial weight of the eppendorf. By taking a rough density of 1.077g/ml ($0.64\rho_{pmma} + 0.36\rho_{cisdecalin}$) the volumes of both the PMMA and cis-decalin can be calculated. CHB is added to be twice the volume of the volume of cis-decalin, giving a reasonable start point for density matching. This mixture is then centrifuged at 13400RPM for 15 minutes. If particles have risen to the top, this indicates that the solvent is too dense, and so additional cis-decalin is added. If they sink to the bottom, then the solvent is not dense enough and additional CHB is added. The particles are then redispersed with a vortex IKA ms 3 basic This is repeated with increasingly small amounts of additional solvent until no noticeable movement up or down has occurred after centrifugation. This entire process is then repeated with a centrifuge time of 30 minutes, though usually this only requires a small number of iterations.

The speed of sedimentation of spherical particles is given by equation 2.1, where ρ_p is the density of the particles, ρ_{sol} is the density of the solvent, μ is the dynamic viscosity of the fluid and a is the radius of the particles.

$$v = \frac{2}{9}\frac{\rho_p - \rho_{sol}}{\mu} g a^2 \tag{2.1}$$

Taking a worst case scenario that any bulk particle movement which is less than 5mm will not be noticeable, this procedure will give a solvent with a density error smaller than 0.01% of the PMMA density for 2µm particles and within 0.1% for 600nm particles.

2.5 PREPARING SAMPLES AT A KNOWN VOLUME FRACTION

The behaviour of Hard Spheres is controlled by a single parameter, the volume fraction Φ. We therefore need to be able to establish the volume fraction in our samples. There are several ways of doing this, and the most immediate is to prepare samples with a known weight of PMMA, and a known weight of solvent. By dividing these quantities by their densities, we arrive at the volumes of the components, and the ratio of these volumes gives the volume fraction. However, PMMA is ideally stored in solvent, and both systems used in this work are stored at low Φ in cis-Decalin, so simply weighing a known amount of PMMA and a known amount of solvent is not possible.

Instead we take advantage of the fact that monodisperse hard spheres at random packing have a $\Phi = 0.64$[11,142]. First we density match the sample using the procedure detailed in section 2.4. Then the density matching is broken by heating the sample up to 36°C in a temperature controlled centrifuge. At this temperature the solvent becomes slightly less dense than the colloids, which sediment given enough time. Forming a well sedimented pellet on the bottom of the container takes between 90 minutes and 2 hours. This sediment will be at random close packing, and will therefore have a $\Phi = 0.64$. The supernatant solvent can be withdrawn with a pipette, and weighing the remaining pellet gives the volume V_{Pellet}, with the density given by $\rho_{PMMA} = 1.18$. This volume multiplied by 0.64 gives the volume of PMMA, V_{PMMA}.

With the volume of the random close packing pellet established, previously withdrawn density matched solvent can be reintroduced to the sample, diluting the PMMA to the desired volume fraction $\Phi_{Desired}$. The volume of solvent required for a given volume fraction is given by equation 2.2.

$$V_{Solvent} = \frac{V_{PMMA} - (\Phi_{Desired} V_{Pellet})}{\Phi_{Desired}} \tag{2.2}$$

In practice this preparation method results in a PMMA suspension reasonably close to the desired volume fraction. It is not perfect, as there are multiple possible random and systematic errors[76]. When density matching, there can sometimes be small amounts of PMMA residue that become trapped on the walls and near the lid of the container. This will be counted as part of the pellet, despite not contributing to the density of the final sample, reducing the true Φ from the preparation Φ. Similarly, small amounts of solvent can remain clinging to the walls of the container, which will increase reducing the

true Φ from the preparation Φ. This second effect can be reduced with repeated centrifugation after the initial withdrawal of the supernatant solvent

PMMA itself can have slightly different densities depending on synthesis technique, and each batch of PMMA produced by a given technique will have slightly different densities[143]. However, if the sample is density matched, it turns out that using the incorrect density for the PMMA does not change the final prepared volume fraction. This is because no volumes are actually measured during the procedure. Weights are taken for both the PMMA/solvent $\Phi = 0.64$ pellet, and for the additional diluting solvent which is added. As long as the PMMA and the solvent are at the same density, the weight ratio of additional solvent and the pellet will be the same as the volume ratio, with the density being a cancelled common factor. This means that we do not need to worry about measuring precise densities to have consistent and accurate volume fractions.

With some particle systems, however, the densities *within* the system can differ. This become apparent when density matching - as the density of the solvent approaches the mean density of the PMMA, eventually some particles begin to move down whilst others move up. The PMMA densities can be made more homogeneous by drawing off those particles which rise to the top of the sample with a pipette. None of the work detailed here, however, uses systems of this type. Particles in this work never split - meaning that the width of the distribution of densities within the system is within the error on the density of the matched solvent. Even if they did split, so long as the distribution of the densities is symmetric about the mean, the measured volume fractions should remain accurate.

2.6 CAPILLARIES

The capillaries used to throughout this work are supplied by Vitrocom. Square capillaries are cross-section mm by mm and rectangular capillaries are cross-section mm by mm. The length of the capillaries is generally between one and two centimeters, and they are cut down from the longer stock capillaries using a diamond tip glass cutter. Using smaller capillaries saves both the glass itself, as well as precious PMMA sample. If the PMMA sample is re-diluted and place back into a stock, very small amounts of dried PMMA can be made to last for dozens of experiments, as each capillary only has a tiny volume.

The capillaries are filled by simply placing one end into a suspension of colloidal particles made up at a known volume fraction. They are

then sealed using either an 2-component epoxy glue which is mixed up before the capillary is filled. Alternatively, a Norland 63 Optical Adhesive UV glue can be used, which cures under a standard low-wattage UV light in around 5 minutes. The UV glue has the advantage of not having a mix-up procedure which must be carefully timed with the filling of the sample. In this work, only very early experiments used an epoxy glue, with Norland 63 being used for the vast majority of the rest. Using this glue, samples are air tight for at least several weeks. This is clear from observing samples which are improperly sealed - the sections of the sample nearest to the leak will bear clear signs of the solvent evaporation. Often a meniscus can be seen at the new air-solvent interface, for example, or particles simply stop moving as they become confined to a smaller and smaller region of the capillary. When samples are properly sealed however, neither of these effects are seen, even when imaging weeks later.

2.7 CONFOCAL IMAGING

Colloidal particles tend be between a few hundreds of nanometers and a few microns in diameter. This means their length scale is on the order of visible light, so optical microscopy techniques can be used[144]. However, conventional light microscopy faces problems with samples at high volume fractions, as the light scatters off multiple colloids on its path to the lens, blurring the image. Marvin Minsky, whilst attempting to image dense 3d networks of neurons, made two crucial improvements changes to the conventional optical microscope. Firstly, his microscope only imaged a single point of the specimen at a time, avoiding the detection of light scattering from the points which are not being imaged[145]. This eliminates some stray light, but not that which has been scattered from the point of interest and then again from another point. To eliminate most of this light, Minsky placed a pinhole before the detector, which rejected light that was out of focus. The illuminated point is then scanned across the entire sample, and an image is gradually built up. The fact that the out of focus light is rejected means that each two dimensional image is highly confined to a single plane, and so multiple two dimensional images focussed on slightly different planes can be taken to build up a full three dimensional 'z-stack'. Further improvements to Minsky's original design include using a laser as the illumination source, which gives brighter point illumination[146]. Fluorescently dyed samples further improve the imaging, as light emitted from the dye after excitation by the laser is at a different wavelength to the laser itself. By filtering

the signal entering the lens to just that at the emission wavelength, all light from the illumination source can be removed from the final image[147].

When taking confocal images of our colloids we generally have a choice of several imaging parameters. We may decide to average either with frame averaging over multiple images of the same region or line averaging over multiple scans of the same scanning line, which are then stitched together to form the final image, or both. These generally improve the final image, so long as the particles move with a Brownian time much longer than the imaging time. If this criterion is not met the images will be blurred. In practise this means that images of liquids at low packing fractions cannot be averaged, whilst supercooled liquids, crystals and glasses can be averaged to increasing degrees. Excitation and emission laser frequencies are determined by the excitation and emission wavelengths of the relevant dye. Aperture size and signal gain are chosen to ensure that the image is not under or over sampled. This is achieved by ensuring that the distribution of pixel intensities is Gaussian, preferably with essentially zero saturated pixels (intensity = 255) and few pixels of 0 intensity. We choose a zoom on the image according to the necessary image region size. For some applications, for example particle resolved experiments that require accurate particle centre tracking this might be relatively small, around 20σ in x and y. For qualitative experiments (checking by eye to see if a sample has crystallised for example), or experiments with intensive analysis that does not require particle tracking, a larger box can be chosen of around 50σ. We also choose the size of the distance moved by the focal plane between each z step. This is a "pixel size" in the z dimension, and it is chosen to be equal to the pixel size in x and y. This aids tracking and further analysis.

2.8 PARTICLE TRACKING

2.8.1 Crocker and Grier

The algorithm originally developed to extract colloidal particle positions from microscope images was developed by Crocker and Grier in 1995[148]. The algorithm relies on finding local maxima within the image - a pixel is a candidate particle if there are no brighter pixels in a neighbouring region, and if it is in the brightest 30% of particles in the image. In order to suppress the effects of noise Crocker and Grier convolve their image with a Gaussian kernel, which smooths and blurs the image. To further improve the position accuracy, the algorithm

calculates the brightness-weighted centre of the region surrounding the brightest pixel. If this is more than half a pixel from the brightest point, the candidate centre can be moved slightly in the direction of the brightest-weighted centre, and the brightest-weighted centre of the new local environment can be calculated. The process is repeated until the centroid centre is close to the candidate centre, and then the centre is accepted. This can result in particle positions accurate to within one tenth of a pixel length[148,149]

2.8.2 Colloids Multiscale

The Crocker and Grier algorithm works well for large monodisperse particles. However for polydisperse particles, especially highly polydisperse particles, the algorithm can fail. This is because for polydisperse particles there is not a clear choice of Gaussian kernel size which can pick out all the particles. The code developed by Mathieu Leocmach[150], the “Colloids" package, includes a “multiscale” particle tracker. This code implements the scale-invariant feature transform (SIFT) developed by Lowe[151]. It moves beyond Crocker and Grier by using a series of Gaussian convolutions of different kernel sizes. As a Gaussian convolution discards high frequency information, by taking the difference of Gaussian-blurred images blurred with slightly different kernel sizes the final image essentially only frequency information that exists between those frequencies filtered out by the two Gaussian blurs, that is, corresponding to a particular length scale. Particles can be located by taking the local minima of these “difference of Gaussian" images, in a similar way to the Crocker and Grier algorithm, but now the scale at which the minima is lowest corresponds to the size of the particles.[150]

2.8.3 Tracking in Practice

In order to extract particle positions from our experimental images, we use the Colloids Multiscale python package[152]. The code has several tuneable parameters which can be chosen to improve tracking results for different soft matter systems. The most important is k, which controls the size of the Gaussian kernels used in the difference of Gaussians part of the algorithm, and therefore sets the size of the smallest particle which can be detected. There is a further parameter, the number of octaves used, which sets the maximum scale of particles which can be detected. As our systems are quite monodisperse, we find changing the number of octaves makes very little difference to the number of detected particles or their positions, and invariably

leave this parameter unchanged at 1 octave. The final parameter is the "remove overlaps" option. The multiscale tracking has a tendency to find overlapping particles, for example if noise exists which gives a single particle two maxima the code can find the original particle and a much smaller particle overlapping it. Also, if a particular cluster of particles is particularly bright the code can find the entire cluster as a single, very large particle, as well finding the smaller particles with which it is comprised. The remove overlaps feature finds all pairs of particles which have centres closer than the radius of the larger particle, and then removes the particle which has the lowest intensity. We find that removing overlaps improves the quality of the final co-ordinates.

This leaves k as our only free parameter in the tracking. Shown in Fig. 2.1 is the behaviour of the number of particles we detect, expressed as the volume fraction of particles found, as we change k. k begins at 1.2 because this is the advised lowest value in the documentation, choosing k lower than this would likely result in the detection of noise as particles.

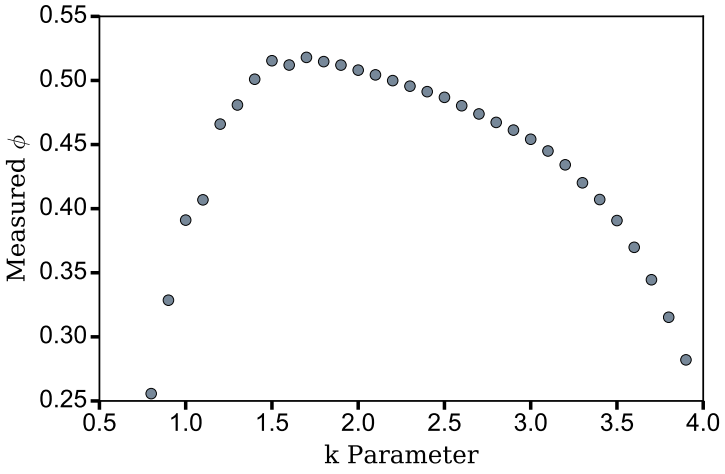

Figure 2.1: The effect of changing the adjustable parameter on the measured volume fraction for a sample prepared at $\Phi = 0.52$. There is a peak at around k = 1.6, and this peak is the feature used to choose k. At this value the volume fraction agrees well with our expected volume fraction from the weight of the PMMA and solvent.

2.9 SINTERING CAPILLARIES

When conducting experiments on crystallisation, it is important to control the boundaries of the system. Crystallisation can occur either heterogeneously, when a crystal nucleates from a wall or a large seed,

or homogeneously, when the crystal nucleus is formed spontaneously in the bulk liquid[24]. Heterogeneous nucleation occurs with a much higher nucleation rate density than homogeneous nucleation. This can be understood within the framework of classical nucleation theory by considering that at a wall, the symmetry within the system is broken and so a nucleus need not be spherical. Partial spheres will have lower surface areas than spheres of the same volume, and therefore have a lower surface tension and free energy barrier[153]. The nucleation rate density depends exponentially on the barrier height, and so even small differences in the barrier height result in huge changes to the nucleation rate density. This means that in our experimental technique, with a bulk colloidal fluid suspended in a capillary, the crystal will nucleate preferentially from the walls. This will happen so quickly as to render measuring the relevant homogeneous nucleation rate densities essentially impossible.

In the case of non-flat walls, however, the situation is significantly more complicated. Nucleation can be either favoured or disfavoured depending on the wall curvature and texture. Walls with patterns which are commensurate with the structure of the crystal phase will tend to increase the nucleation rate, whereas patterns incommensurate with the crystal structure will slow nucleation or prevent it altogether[154]. The introduction of impurities, spheres of larger size than the liquid particles that act as seeds, is also complicated. Generally it is plausible that very large seeds, which approximate flat walls will increase nucleation rates, whilst smaller seeds will inhibit nucleation, as their high curvature creates too much internal stress for the growing crystallite. Sandomirski *et al*[155] state that for a seed diameter $\sigma_{seed} < 20\sigma$, where σ is the diameter of the nucleating particles, nucleation will be suppressed. It is worth noting that Allahyarov *et al*[156] found that a seed with diameter($\sigma_{seed} = 15\sigma$) will favour initial nucleation, before the internal stress created by the curvature of the seed in the nucleus causes it to split from the seed and grow conventionally in the bulk.

If we wish to study homogeneous nucleation and do not have the luxury of periodic boundary conditions available in simulations, we can exploit the effects of patterning and curvature. Patterning the walls of our confining capillaries with a random coat of polydisperse spheres suppresses heterogenous nucleation. The randomness and the polydispersity are both highly unlike the desired crystal structure, which is ordered and made of reasonably monodisperse hard spheres. Furthermore, choosing a mean wall particle size of 4-5 bulk particle diameters creates high curvature at the particle level, which is also

deleterious to crystal formation. This technique has been applied in previous experimental work to study homogenous nucleation in experiment[62,157].

In order to pattern our capillaries in this manner, we choose a highly polydisperse PMMA and swap the solvent to Hexane (usually from cis-Decalin). Hexane is an ideal solvent because it dries rapidly, both speeding up the process and reducing coffee-ring effects which cause PMMA to be deposited preferentially at the ends of the capillary[158]. The process for exchanging the solvent is a simple one, involving centrifuging the PMMA into a pellet, replacing the supernatant solvent with Hexane, and redispersing. This is repeated multiple times, which can give an arbitrary hexane purity. In practise we repeat 4 times, resulting in a hexane volume concentration $c_v > 0.99$. Capillaries are cut to around $2cm$ in length, and are placed in the disperse PMMA solution. They are very rapidly filled as capillary forces draw the PMMA and solvent to the top of the capillary. The capillaries are left to dry for at least 2 hours, when all hexane appears to have dispersed, leaving a thin sheet of PMMA particles on the walls of the capillary. The capillaries are then placed in an oven at $130°C$ for 90 minutes. This sinters the PMMA particles, melting them to the glass surface of the capillary. The capillaries are then viewed under a Lecia DMI3000B optical microscope to ensure that the PMMA layer covers the entire surface. If the layer is only partial, the process is repeated. Images of this process can be seen in Fig. 2.2.

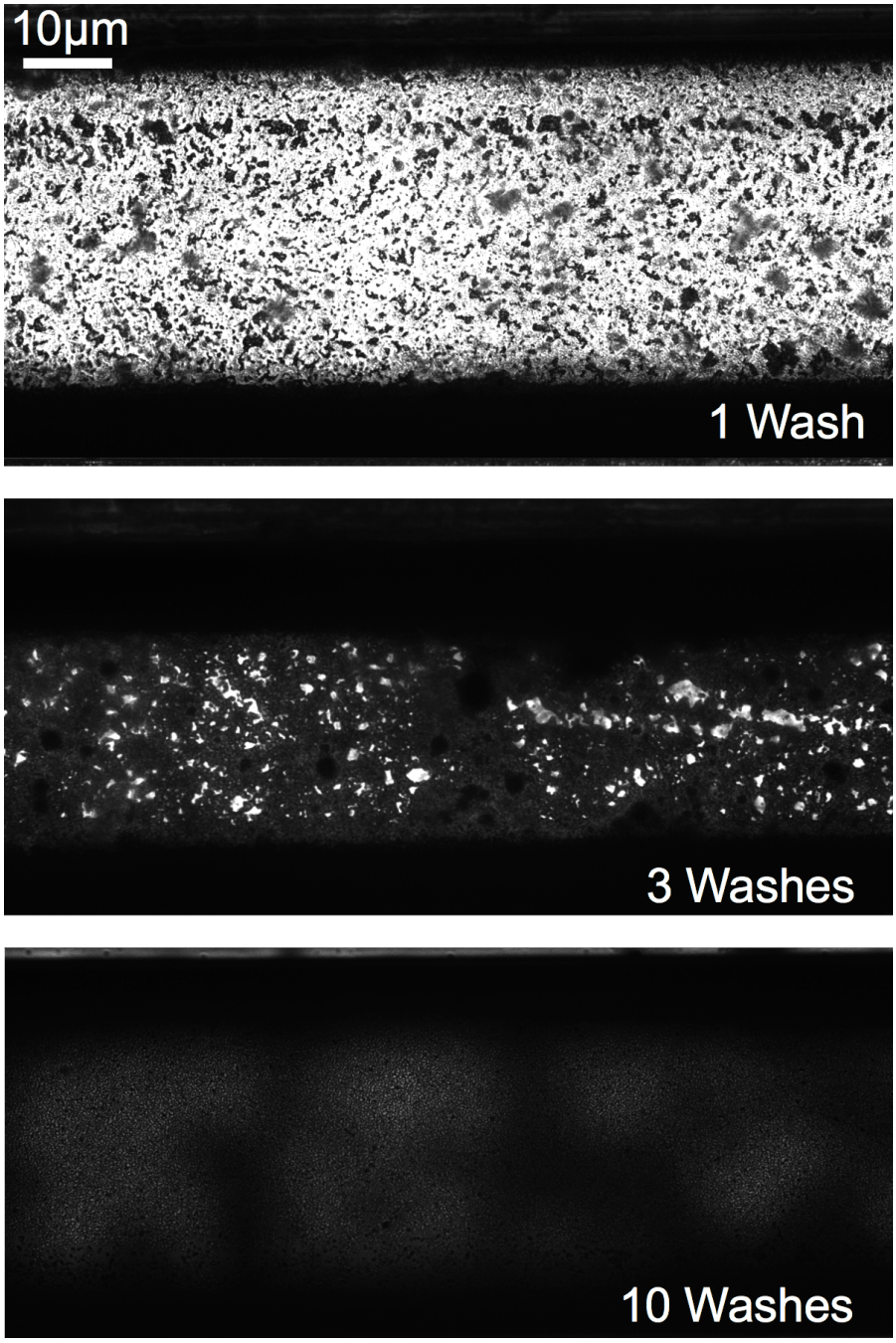

Figure 2.2: The effect of sintering with increasing numbers of washes. By 10 washes, the wall has been fully coated with polydisperse PMMA. These images are with a polydisperse PMMA of average size 1μm, with a volume fraction in hexane of around 10%.

Part II

RESULTS

3

THE EFFECT OF SEDIMENTATION ON THE STRUCTURE OF HARD SPHERE LIQUIDS

3.1 INTRODUCTION

The literature experimental results on hard sphere nucleation show much larger reduced nucleation rate densities than biased Monte Carlo simulations, forward flux sampling[99], and seeding simulations[100] (see section 1.4). As discussed previously, sedimentation appears to be a promising potential explanation for explaining this disagreement. Our hypothesis is that the small amount of sedimentation present in the experiments is inducing a change in the local structure of the hard sphere fluid, which is favouring nucleation.

We can study this effect using simulations or experiments, or a combination of both. The advantages of simulations are that they give the precise positions and dynamics of all particles, meaning analysis can be done with no need to worry about experimental error. However, the drawback is they are constrained to the current limits of computing power. This generally means that simulations can include aspects of a complex nucleation process, including, for example, hydrodynamics[121] or sedimentation[112], or they can probe the deeply supercooled regime where the discrepancy exists, but not both.

As discussed in Section 1 many different avenues have been explored for explaining the nucleation rate density discrepancy between simulations and experiment[88]. None of these have yet proved adequate[99]. The two most promising routes appear to be those of sedimentation[88] and hydrodynamics[121]. Both constitute substantial differences between the biased Monte Carlo simulations and the experiments they attempt to recreate. Both are difficult to recreate in simulation. Hydrodynamics are inherently computationally expensive and therefore difficult to combine with rare event techniques. Multiparticle collision dynamics[159], for example, is a natural choice for simulating colloids embedded in a solvent, but at high volume fractions it is necessary to resolve the solvent flows down to length scales smaller than a particle radius, which can be challenging[160].

Sedimentation, meanwhile, can be implemented in simulation fairly easily by simply adding a gravitational force to all the particles, which will then form a barometric profile[112]. However, the relatively small

size of the simulations means that the choice of boundary condition becomes important - implementing rough walls means that the system very rapidly reaches its equilibrium density profile, whereas periodic boundary conditions mean it will never reach the equilibrium density profile. The rich behaviour of sedimenting experimental systems can only be studied with much larger simulations, in which measuring nucleation is prohibitively expensive. Even worse, sedimentation is itself hugely affected by hydrodynamics. Even the most basic quantity, the sedimentation velocity, is reduced by hydrodynamic interactions. Roughly speaking, this reduction goes as the Richardson Zaki law, $v_s/v_s^0 = (1-\Phi)^n$ with $n \approx 6.6$[129]. This means that at the volume fractions relevant for nucleation, the reduction in the sedimentation velocity is more than two orders of magnitude. To fully capture sedimentation in the experimental systems, then, we need to also take hydrodynamics into account.

Given these issues, we run experiments rather than simulations to explore the effect of sedimentation on hard sphere fluids. Running experiments allow us to study the deeply supercooled regime, whilst also giving access to samples which contain around 10^6 times more particles than in a normal simulation. This means that we can examine sedimentation across large length scales of many thousands of particle diameters, the same length scale that exists in the scattering experiments. Furthermore, we automatically capture the hydrodynamic effects at no cost. The most obvious experimental design would be to simply measure nucleation rate densities for sedimenting and non-sedimenting samples. However, one difficulty in simulation which is equally hard to overcome in particle-resolved experiments is that of very slow nucleation rate densities at low supersaturations. Scattering experiments overcome this by using much smaller particles than can be particle tracked in confocal data, but the need for high resolution, particle trackable images constrains us to rather larger ($2\mu m$) particles[161] which will nucleate very slowly. The feasible nucleation rate density measurements would therefore be in the more supersaturated regime ($\Phi \gtrsim 0.54$), where no discrepancy exists[62]. The experiments we perform instead compare the local structure of the hard sphere fluid with and without sedimentation. If the local structure is changed in a manner which is favourable to the formation of crystal nuclei, this may explain some of the nucleation rate density discrepancy.

3.2 EXPERIMENTAL DESIGN

3.2.1 Overview

Using real-space confocal microscopy techniques, combined with particle tracking and structural analysis tools, we can experimentally probe changes in the structure of the hard sphere fluid with respect to sedimentation. In order to control the sedimentation, we prepare samples that are both density matched and samples which have their density matching broken to a known degree. The Peclét number, P*e*, can be found to high precision from the weight composition of the solvent. These samples are then imaged in 3 dimensions with confocal microscopy and particle tracked. Applying the TCC algorithm[53,54] to the resulting particle positions, we obtain the population of particles that exist within a large variety of different local clusters. We are interested in seeing if these populations change with sedimentation, and if so, to what degree.

In particular, we are interested in local structural motifs which contain high degrees of five-fold symmetry. Interest in five-fold symmetry dates back to an argument made by Sir Charles Frank in 1952[162], addressing the question of vitrification. Frank calculated that the highly five-fold symmetric icosahedron structure was in fact the lowest energy structure for 13 Lennard-Jones particles, and was therefore likely to occur a great deal in the Lennard-Jones liquid. The icosahedron, however, is unable to tile space[163], and therefore is anathemic to the highly positionally ordered crystal structure. Frank postulated that this locally favoured structure played a key role in allowing the Lennard-Jones liquid to bypass crystallisation and become a glass. Later work on liquid structure also identified local five-fold symmetry as important[164,165]. The modern work reviewed in section 1.1.2.2 emphasises the importance of crystal-like structure and regions of high density in the formation of crystal nuclei, but other work has interpreted the crystallisation process as a competition between five-fold symmetry and the six fold symmetry of the crystal[62,166]. In 2016, the direct role of five fold symmetry in suppressing crystallisation through increasing the solid-liquid surface tension was demonstrated[61].

The most highly five fold symmetric cluster identified in the TCC is the icosahedron, with twelve interlocking pentagons, one surrounding each vertex. This cluster, however, is quite rare in the coexistence regime where the nucleation discrepancy exists[62]. If we focus on icosahedra populations then, it is likely that very large amounts of data will need to be collected to discern any changes when sedimentation

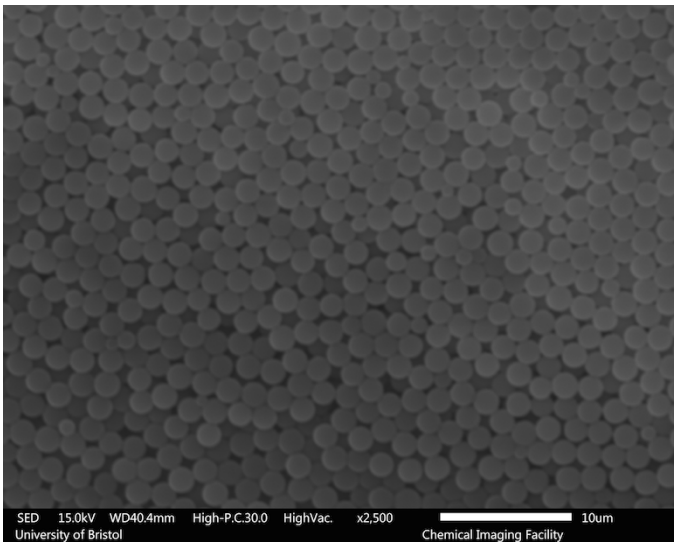

Figure 3.1: A scanning electron micoscope micrograph of the particles used for this work.

is induced, as the error on the populations will be quite high. As an alternative, we study the *defective icosahedra* (known as the 10B in other work). This is an icosahedra with a single three membered "cap" removed. It thus has ten particles which form three five membered rings. The defective icosahedron is very common in supercooled hard sphere liquids[60,167,168]. Moreover its population decrease during the crystallisation process is concomitant with the rise of the FCC crystal[61,62], suggesting that it is a good proxy for the five fold order which must be suppressed throughout crystallisation. Defective icosahedra structures are also very long lived in hard sphere liquids, with average lifetimes at least double that of almost all competing local structures[169], with only the icosahedra itself having a similar lifetime.

3.2.2 Particles

These experiments use particles made from PMMA. They are stabilised with a surface coating of short PSHA hairs, which stabilise the particles and give a sharp repulsive potential at short distances (see section 1.3.2.3), as needed for a hard sphere potential.

3.2.2.1 Size and Polydispersity

In order to establish the size and polydispersity of the particles, they are imaged using Scanning Electron Microscopy (SEM). A typical image is shown in Fig. 3.1.

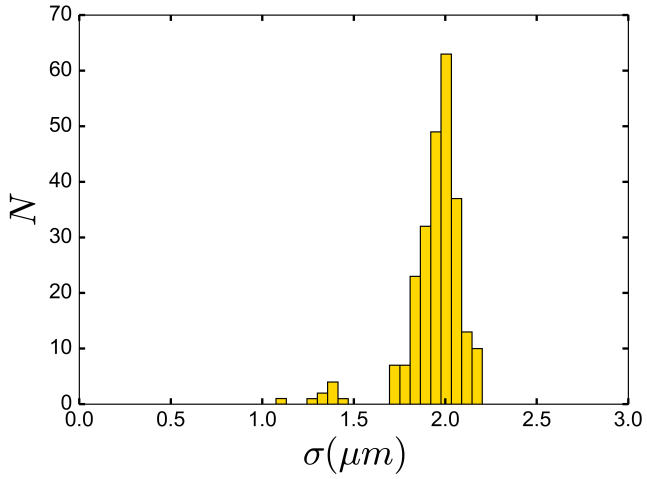

Figure 3.2: The distribution of sizes, in microns, of 250 particles.

We measure the sizes of two hundred and fifty of these particles by hand, which gives us a distribution of the particle sizes. This distribution is shown in Fig. 3.2. We see two populations, one which comprises the majority of the particles (more than 95%), centred around 2μm and a second, more heterogeneous group of particles with diameters less than 1.5μm. This second group is not seen in the confocal images. This may be because when drawing a sample into the capillary, it is generally taken from the centre of the centrifuged pellet. These smaller particles will sediment rather more slowly than the large group, and so will tend to be in the top of the pellet, meaning they do not end up in the final sample. The standard deviation of the diameters of just the particles in the larger group is 0.089μm, whilst the mean is 1.97μm, giving a final polydispersity of 4.5%.

This measured size is likely to be slightly lower than the size of the particles in a CHB/cis-Decalin solution. It is known that the particles can swell in good solvents, such as CHB[76,170]. This could be problematic for our experiments, as we use differing amounts of CHB in our solvent compositions, and thus It is possible that our particles will be slightly bigger in the creaming case (CHB Rich) than in the sedimenting case (cis-Decalin rich). It is likely this won't be a concern, as the particles should only swell by a small amount (their crosslinking restrains them from greatly expanding[170]), and so they should swell to this maximum size in all three of our solvent compositions. However, this is something that should be checked.

In order to check the degree of swelling, we leave our particles for 2 weeks in the 3 separate solvent compositions. These are the sedimentation, creaming, and density matched compositions discussed

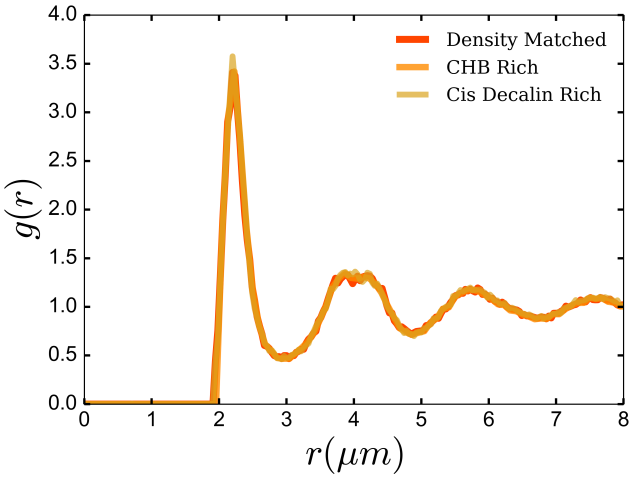

Figure 3.3: Measured radial distribution functions for all three solvent compositions.

in section 3.2.5. Dynamic Light Scattering was attempted, but the refractive index of our solvent was too close to that of the particles for clear results. Instead, we prepare three samples at a known volume fraction of 55% (using the method described in section 2.5), and compare the radial distribution functions. This is shown in Fig. 3.3. The position of the first peak is unchanged in the the three cases, which is highly suggestive that the particles have not swelled to different degrees in the different solvents. The maximum of the first peak is at around 2.2μm, so there has been a swelling of around 10% in all three solvents, which is consistent with previous results[63].

3.2.3 Measuring Crystallisation Times

The first step of our experimental work was to check that the crystallisation times for our particles matched those of previous work in which the volume fraction was carefully compared to simulations[62]. This is done to check that the interaction potential is close to that of hard spheres, and to give further confirmation that the packing fractions we measure correspond well with the true hard sphere packing fraction (see section 3.2.4).

This was done in capillaries sintered in the manner described in section 2.9, using sintering particles with a radius of 3μm and polydispersity ~ 50%. The protocol for measuring the crystallisation time was the same as Ref.[62], that is, when 40% of the sample was identified as crystal by eye.

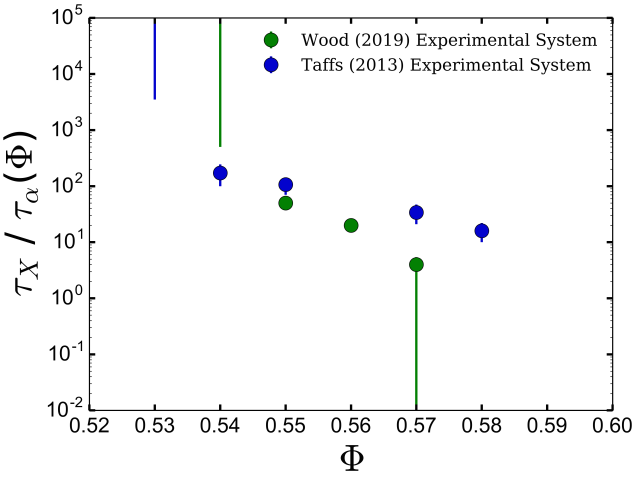

Figure 3.4: Measured crystallisation times for this system relative to that of Taffs (2013). Our data point at $\Phi = 0.54$ did not crystallise, whilst our data point at $\Phi = 0.57$ had crystallised on the first measurement after around 2 hours ($3\tau_\alpha$).

Figure 3.4 shows the measured crystallisation times against those of Taffs *et al.*[62] for a series of different volume fractions. The experimental system used in Taffs (2013) is almost identical to ours, with the same solvent choices and particle size and polydispersity. We therefore use the measured alpha time, $\tau_\alpha(\Phi)$, of Taffs (2013) with respect to volume fraction to scale our crystallisation times. The alpha time is a time scale which characterised the dynamics of the colloidal particles at a given volume fraction. It is found by performing a Vogel-Fuclher-Tammann fit to an intermediate scattering function[62]. We choose to normalise our raw crystallisation time data (measured in seconds) by the alpha time, as it gives a better understanding of the speed of the crystallisation process itself. In the raw data, crystallisation times increase with increased volume fraction, but this is simply because the entire system is slowing down, rather than because crystallisation is becoming less energetically favoured. Normalising by the alpha time corrects for this overall slowing, and we recover the expected trend of crystallisation becoming faster with increased volume fraction.

Given the difficulties of measuring the crystallisation time, the result in Figure 3.4 constitutes a good agreement. As the nucleation barrier falls very rapidly with increasing supersaturation, crystallisation times that are not an order of magnitude higher or lower than each other are indicative of very similar volume fractions, within 1 percentage point of each other. This is the case even for the experimental nucleation rate density curves of scattering experiments, which are relatively shallow compared to the simulations.

3.2.4 Measuring Volume Fractions

The crucial parameter for the hard sphere system is the volume fraction, Φ. We have a rough estimate of the volume fraction from the crystallisation times, the parameters of the sample preparation, the volume of the particles calculated from particle tracking, and by matching our radial distribution function to the theoretical Percus-Yevick form for hard spheres.

We also have an understanding of the volume fraction from the procedure described in section 2.5. Given that we know that random close packing of hard spheres gives an approximate packing fraction of $\Phi = 0.64$[11,142], we can add a known amount of density-matched solvent to bring a closely packed pellet to a desired packing fraction. There are errors on this process however as described in section 2.5, and so our determined packing fractions should be cross checked with other methods.

From our particle tracking method we can find the total number of particles in the imaged volume. Using the measured average particle radius, this can be converted to a packing fraction as $\Phi = \frac{N\frac{4}{3}\pi r^3}{V_{image}}$. This measurement is quite prone to error, however. As the radius is cubed, it contributes an error on the packing fraction equal to thrice its own error. A 2% error in the radius, therefore, gives an error in the packing fraction of 6%. Furthermore, finding the true volume of our image is difficult. Whilst the microscope image metadata gives a very accurate estimate of the x, y, and z dimensions, the relevant volume of the image is not simply the product of these three length[63]. This is because the tracking cannot usually identify particles which are cut off by the edges of the imaging box, thus using the x, y, z product will underestimate the true volume fraction. To account for this, we use a reduced imaging volume, equal to the product of the 3 dimensions after they have each been reduced in length by one particle diameter (a radius on each side). However, this reduction produces another error related to the radius. This error is much smaller than that on the particle volumes, as an error of 2% on the radius contributes only a 0.05% error to the length of the reduced dimensions (if each is 20σ). The imaging volume therefore has an associated error of 0.15%. The particle count therefore gives us a reasonable handle on Φ, to within 6.15% or so. This is good enough to ensure that our measurements from the sample preparation (which are generally more precise) were broadly correct. For example, extreme errors on the sample preparation resulting from mis-labelled capillaries, or typos when entering weight information into calculation spreadsheets can

be discovered at this stage. This measurement, however, is not good enough alone for the very precise measurements in the volume fraction needed for, for example, measuring nucleation rates.

3.2.5 Choice of Solvent Composition

3.2.5.1 Sample Prepatation

Our colloidal system allows precise control of the degree of sedimentation, through the density matching protocol explained in section 2.4. By density matching as before, and then adding a precise amount of extra solvent, samples can be prepared at a given Peclét number. The solvent composition can be changed to either be CHB rich (PMMA particles cream) or cis-Decalin rich (PMMA particles sediment).

We decide for this study to examine colloidal liquids sedimenting with Peclét number +/-1.5. This is in the high regime of sedimentation, and indeed is higher than that seen in the literature nucleation experiments, which have Peclét numbers between 0.01 and 0.3. Indeed, as Pe is above 1, we are seemingly in a different regime altogether - the sedimenting rather than the Brownian regime. However, the choice of $Pe = 1$ for this cut off is arbitrary - indeed "the specific dependence on Pe is expected to depend on the investigated structural or dynamic effect"[171]. As such, whilst the chosen Peclét number is high, this work can set an upper bound on the importance of sedimentation to the nucleation rate. If we see very little effect, even at this Peclét number, we can draw the important conclusion that sedimentation coupling to five fold symmetry is not an important factor in explaining the nucleation rate gap.

We can reach these Peclét numbers by running samples with a solvent composition that is almost entirely CHB for creaming, and around 33% CHB, 67% cis-decalin for sedimenting. The density matching mixture is around 67% CHB, 33% cis-decalin, assuming a PMMA density of 1.18 and a linear behaviour of the mixture density with CHB/cis-decalin composition. We can prepare samples with the sedimenting composition quite easily. Simply centrifuging our PMMA to random close packing from the stock 100% cis-decalin solvent, removing the supernatant, and adding CHB until the correct proportions are reached. The sample is then mixed for several hours, re-centrifuged, and concentrated to the correct volume fraction, in a similar manner to density matched work (except there is no need to heat the sample, as it will naturally sediment due to the density mismatch). To prepare the creaming sample, PMMA from the cis-decalin stock is washed in CHB. The PMMA is centrifuged in cis-decalin stock, the amount

of cis-decalin remaining in the pellet is weighed, and a volume of CHB corresponding to 9 times the volume of cis-decalin is introduced. After careful mixing, the process is repeated. Each wash brings the concentration of cis-decalin in the solvent down by an order of magnitude, so after two washes, the CHB concentration is 99%, which gives us the correct density mismatch. Concentrating the sample is more challenging in this case, as when centrifuged the colloids move up instead of down. The clear solvent must then be extracted using a pipette tip which "breaks" the PMMA meniscus. Care must be taken to avoid pipetting up any stray PMMA. The errors on this process are certainly larger than in the density matching or sedimenting case, but generally we were able to prepare samples at volume fractions which agreed well with the results from other measurement methods.

3.2.5.2 Controlling for Solvent Composition Changes

Care must be taken when changing the solvent composition however. Whilst this does affect the Peclét number as desired, the solvent composition also controls other aspects of our experimental system. The electrostatics will change with different solvent composition, as the dielectric constant will be altered. Similarly, the solvent composition controls the refractive index match, and therefore the quality of the imaging.

We can model the change in the electrostatics using a Yukawa potential (see section 1.3.2.2). One parameter that will change on altering the solvent composition is the Bjerrum length, given by $\lambda_B = \beta e^2/4\pi\eta_0\eta_r$. In our CHB rich solvent composition the dielectric constant will be very close to that of CHB, η_r(CHB) = 7.9. The dielectric constant of the cis-decalin rich solvent will be around 4.1. This assumes a linear dependence of the dielectric constant on the solvent composition, which appears to be reasonable given that Leunissen[172] measures a dielectric constant of the density matched mixture of 5.6, very close to a linear combination of the solvents. We therefore expect a Bjerrum length in the CHB rich solvent that is around half of that in the cis-decalin rich solvent. This then affects the inverse Debye screening length $\kappa = (4\pi\lambda_B\rho_{ion})^{\frac{1}{2}}$. We might also expect the density of ions to be affected, but as we use 4mM of TBAB, the solution should be well past supersaturation in both cases. Overall, we expect κ to be around 30% smaller in the CHB rich case than in the cis-decalin rich case.

Another factor that will be affected is the colloid charge. The empirical rule of thumb is that $Z\lambda_B/\sigma = 6$[76]. Therefore, Z will be around twice the size in the CHB rich solvent than in the cis-decalin rich solvent. This will feed through to the contact potential, which also

Table 3.1: The Yukawa parameters for our three different solvent compositions.

Composition	ϵ_r	$\lambda_B(m)$	$\kappa(m^{-1})$	$\beta\epsilon_Y$
Density Matched	5.6	1.00×10^{-8}	1.98×10^{7}	16.5
CHB Rich	7.9	7.09×10^{-9}	1.67×10^{7}	32.3
cis-Decalin Rich	4.1	1.037×10^{-8}	2.32×10^{7}	8.99

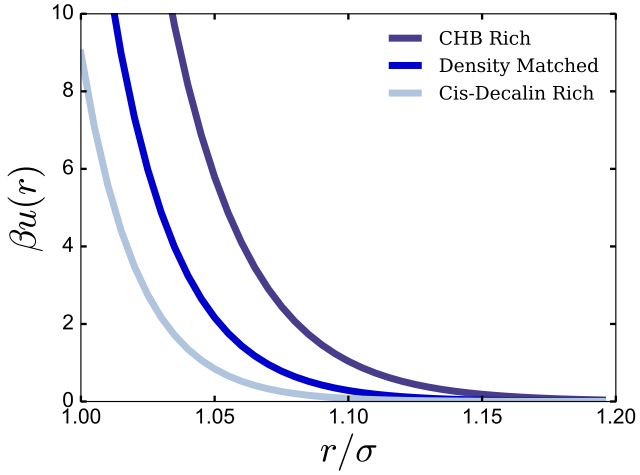

Figure 3.5: The effect of changing the solvent composition on the Yukawa potential of the colloids. It can be seen that the charging is strongest in the CHB rich case and smallest in the cis-decalin rich case.

depends on κ and λ_B. The final change in the Yukawa parameters is given in Table 3.1. The change this will make to the interaction potential itself is shown in Fig. 3.5

We would therefore expect to see an increase in the measured size of the CHB Rich particles and a decrease in the size of the Cis-Decalin particles, as measured by the radial distribution function. Interestingly, we do not measure this effect (see 3.3). The overall size of the electrostatics therefore appears to be quite substantially smaller than shown in Fig. 3.5. This is likely to be because the rule of thumb used for finding the charge, $Z\lambda_B/\sigma = 6$ fails to correctly ascertain the degree of charging in this system. Other work which matched the measured experimental radial distribution function to a simulated Yukawa radial distribution found $\beta\epsilon_Y = 1.0$[62]. However, the original Yethiraj - van Blaaderen work[136] which introduced this CHB-cis decalin model system found some considerable charging, enough to move the phase diagram by around 20% in volume fraction. Similarly, Sedgwick *et al.* measure the number of charges per particle to be around 700e[173], whilst Campbell *et al* directly measure a surface

charge of 140e[174]. These differences likely owe to the fact that the ionic strength of CHB can vary from batch to batch and over time[76,172,175], which will itself then change the degree to which the salt dissociates. This explains how Yethiraj and van Blaaderen can measure a TBAB dissociation of 0.5%, whilst Leunissen measures a dissociation of 2%, which makes a huge difference to the size of the electrostatics. The important point is that each experimental system must be carefully measured, and the results of Figs. 3.4 and 3.3 suggest that we are very close to hard sphere behaviour.

A further complicating factor in changing solvent compositions is the refractive index matching. At a solvent composition that matches the density of the particles, the refractive index is also well matched[176]. Changing the solvent composition will change the refractive index match. The relevant refractive indicies are: $n_{PMMA} = 1.4906, n_{chb} = 1.495, n_{cis-decalin} = 1.481$ at a wavelength of 587nm. The refractive index match at density matching has been measured at 1.4876[172], a very close match to the PMMA refractive index (a difference of 0.003). The refractive index of our CHB rich solvent will essentially be that of CHB, 1.495 (a difference of 0.004). Calculating the refractive index of the cis-decalin rich solvent is slightly more challenging, and requires taking into account the non-linearity of the refractive index on mixing measured by Leunissen[172]. When this is done, the final refractive index of the cis-decalin rich solvent is 1.4908, a difference of just 0.0002. This means that our cis-decalin rich solvent in fact has a better refractive index match than the density matched solvent. We therefore expect our imaging to be better in the cis-decalin rich case, and worse in the CHB rich case. This should have the effect of slightly harming our tracking in the CHB rich case, reducing the number of large clusters detected, whilst slightly improving the cis-decalin imaging and boosting the large cluster populations.

The important thing to note about both of these effects (electrostatics and imaging), is that they are *antisymmetric* about a change in the composition of the solvent from sedimenting to creaming. It is hard to say the precise effect of the net combination of the two effects, but we do know that if they are substantial enough to shift the populations measurably, they should shift them in different directions when the samples are creaming versus when they are sedimenting. However, if the sedimentation dominates the effects of the electrostatics and refractive index matching, we would expect the change of defective icosahedra populations to be the same about a movement from CHB rich to cis-Decalin rich solvents. The symmetry is intuitive, as we expect any hydrodynamic effects to be indifferent to the direction of

sedimentation. This is the case only if the compositions are tuned such that each have the same absolute Peclét number, as is the case in these experiments.

We can therefore ascertain the cause of a change in our sedimenting defective icosahedra populations from the density matched case. If the change is symmetric about the sign of the Peclét number, it is likely due to the sedimentation. If the change is antisymmetric about the sign of the Peclét number, or if the change is only seen in one of the sedimenting cases, it is likely due to a change to the potential or the imaging quality.

3.2.6 Sedimentation Profiles

We are interested in the effect of sedimentation on the structure of the colloidal liquid. The samples begin evenly dispersed in the square capillary - their density profiles are flat in the direction of gravity (as well as in the two perpendicular dimensions). As time progresses, the system settles into an equilibrium density profile. For non-interacting particles at low volume fraction this equilibrium profile mirrors the barometric law of gasses $n(z) = n_0 e^{\frac{-z}{l_g}}$ (this approximation is too simple for our systems, which interact through the hard sphere potential and are at high volume fractions)[177].

Before the equilibrium profile is reached, an intermediate and time dependent structure emerges. The system begins evenly dispersed at a single density, Φ_0. As settling begins, a dense ($\Phi = \Phi_s$), layered region emerges at the wall of the container which the particles sediment toward[178]. This region can be either amorphous or crystalline, depending on a complex interplay between the time scales of the crystallisation process and the sedimentation[179]. For systems of the type we study, we expect amorphous layered regions[178]. Above the layered region is a further region known as the "fan". In the fan, the density increases smoothly from Φ_s to Φ_0. Above the fan lies the settling colloids, which remain at $\Phi = \Phi_0$. Finally, above the settling colloids, there is a gap which contains only solvent[180].

The region of settling colloids, above the fan, is the region in which we are interested. This region contains particles settling under gravity, with complicated and potentially interesting hydrodynamic interactions, but with no accompanying density profile. Studying the structure of the colloidal liquid in the presence of a profile is a very different problem. For example, we expect nuclei to be preferentially born in the regions of higher volume fraction[112]. We also expect a higher number of defective icosahedra in the denser regions[62]. Studying the

change in the structure of the hard sphere liquid on sedimentation in the presence of a profile will therefore be dominated by the profile itself. Subtle changes created by the hydrodynamics will very likely be washed out. It should also be noted that the literature experimental data which we are trying to explain was taken at rather low Péclet numbers, which will have shallow, extended equilibrium density profiles. Studying a system with a sharp profile may not therefore give an accurate picture of the liquid structure of the literature experiments. As such, we focus on only the region above the fan - where the density profile is flat.

3.2.7 Sampling

As sedimentation at high Péclet numbers is highly packing fraction dependent, we sample across a wide range of different packing fractions. The regime of interest in this work is especially the weakly supercooled regime $0.495 < \Phi < 0.54$ in which the nucleation discrepancy exists. We extend our sampling to include the dense liquid below freezing $0.42 < \Phi < 0.495$ and the deeply supercooled liquid $0.54 < \Phi < 0.57$. This will allow us to see any interesting trends in the structural changes before the freezing line and after the melting line.

For each packing fraction five independent image stacks are taken on the confocal microscope. These stacks are taken far from each other, separated by over $10^3\sigma$ (2mm). This ensures that the samples are completely uncorrelated with each other, and each sample constitutes an independent measurement of the structures of the liquid.

The size of each sample is $42\mu m * 42\mu m * 83\mu m$ or around $20\sigma * 20\sigma * 40\sigma$. The voxel size (3-dimensional pixel) is $0.164\mu m$ in all three directions. Choosing a cubic voxel size is done by matching the z-step size with the xy pixel size and allows for better particle tracking. The reason for choosing a rectangular box is that an xy size of 256*256 pixels is the maximum that can be easily tracked, 512*512 stacks very quickly begin to use too much memory and take too long to process (>1 hour per stack). We ensure each colloidal particle is around 10 pixels in diameter, as experience has shown that this strikes a good balance between high quality tracking results and obtaining good statistics. However, we can gain better statistics by extending the image in z, and this tends to be easier to process. In theory, we could use a cluster supercomputer for the analysis allowing us to take very large images, but 5 images each containing $\sim 10^4$ particles already gives us very good statistics for bulk cluster populations.

The first set of experiments were for the density matched system. 5 samples were prepared across a range of packing fractions. We then progressed to measuring creaming and sedimenting samples. For this work we measured the same packing fraction regime, and tried to prepare pairs of sedimenting/creaming samples at similar packing fractions. This is very difficult, owing to the systematic and random errors on the packing fraction preparation. However, generally we were successful in preparing samples close to $\Phi = 0.44, 0.49, 0.52, 0.56$. The spread of points around these average values for the sedimenting samples mean that we actually sample the whole range of densities with more fidelity than the density matched samples.

3.3 RESULTS

3.3.1 Density Profiles

From our particle tracking, we can acquire density profiles of the regions we image. This is done simply by binning the final identified particle co-ordinates in the z-dimension, the direction of the gravitational field. Fig. 3.6 shows the profiles each set of samples, separated into creaming-sedimenting sample pairs of approximately the same packing fraction. It can be seen that the density profiles are extremely flat, with the standard deviation across our samples around 0.2%. This means that we successfully sampled only the sedimenting regions with no density profile.

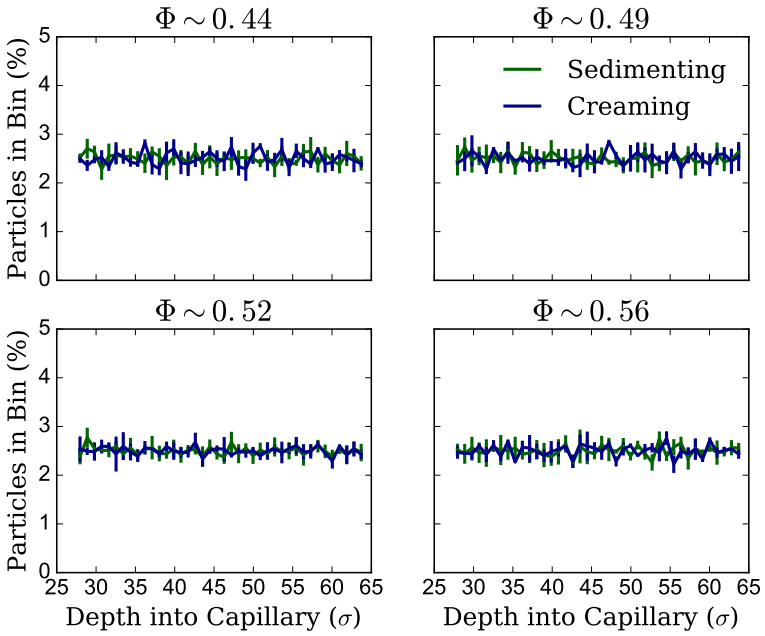

Figure 3.6: Sedimentation profile of all experimental samples. The Y error bar is the standard deviation across all of our repeated samples.

.

3.3.2 Defective Icosahedra Populations

On inducing sedimentation, we observe a decline in the populations of defective icosahedra (10B) clusters relative to the density matched case. The extent of this decline is shown in Fig 3.7. This decline is replicated with the change in the sign of the Peclét number, suggesting that it is caused by the sedimentation of the particles. This decline in defective icosahedra clusters is suggestive - it means that there is less five fold symmetry in sedimenting experiments than in density matched experiments. Therefore, we might expect that experiments, when sedimentation is also present, are less geometrically frustrated by five fold symmetry than simulations (which lack sedimentation) and are able to nucleate more rapidly.

The fall in the defective icosahedra population follows a trend. At high volume fractions, well past the melting line, the change in defective icosahedra population is quite small, relative to the total population. Indeed, at $\Phi = 0.57$, the change cannot be clearly discerned from noise in the populations. As the samples become more weakly supercooled, however, the size of the overall change remains about constant, at about 2.5%, but as the defective icosahedra become generally more rate, the relative size of the gap increases. At $\Phi = 0.44$, the change amounts to a reduction of more than 30% in the population.

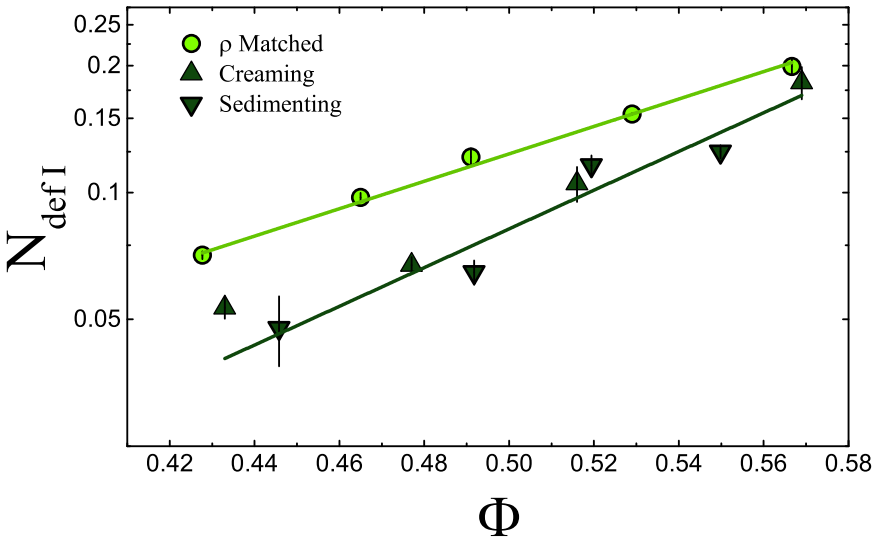

Figure 3.7: The change in the population of defective icosahedra measured when sedimentation or creaming are induced, across a range of volume fractions. N_{defI} is given as the ratio of the number of particles found in a defective icosahedron with the total number of particles in the sample.

This trend is promising, as simulation and experiment only begin to disagree at weak supercooling, whilst at high volume fraction little discrepancy is seen between the two techniques. We would therefore expect that an effect which could solve the discrepancy to be strong at weak supercooling but weak at strong supercooling, as the defective icosahedra population change appears to be.

Section 3.3.1 demonstrated that the density profiles of the entire studied system are flat. It is also interesting to study the profile of the defective icosahedra themselves. The structure of the entire sedimenting liquid is highly heterogenous. It is possible that hydrodynamic interactions between the “fan" region of the liquid and the bottom of our studied region could induce the formation of different local structures than those which exist at the top of our region - which would be more influenced by the top of the sample, which will have lower density.

Shown in Fig. 3.8 is the distribution of defective icosahedra in the direction of gravity (the z direction). This property, however, is inherently a noisy statistic - around 10% of our particles are found in a defective icosahedra, but as the defective icosahedra is ten membered, these particles are highly clustered in space. This means our signal size is of the order of 1% of the total number of particles, binned across the entire capillary length. Furthermore, as five fold symmetric

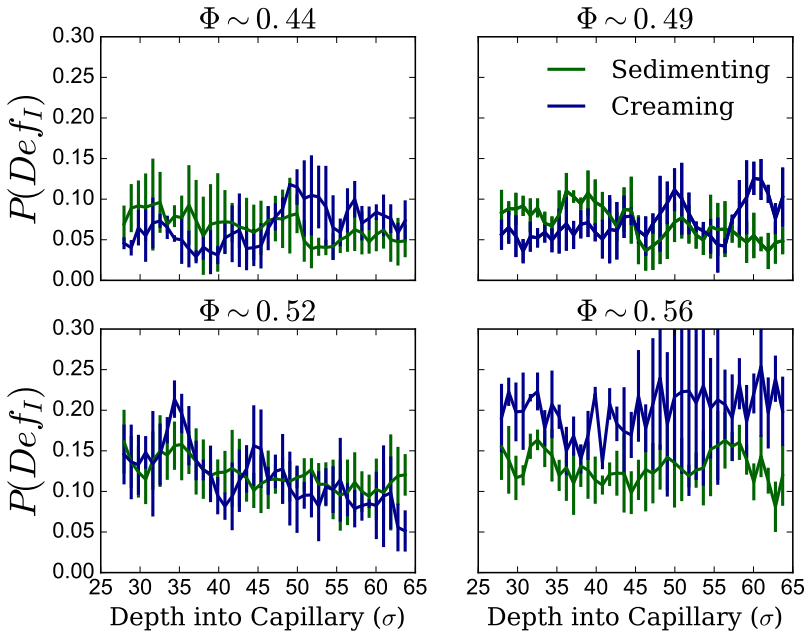

Figure 3.8: The distribution of the defective icosahedra along the axis of the sedimentation or creaming. It appears that the overall signal is fairly flat, although the signal is very susceptible to noise, as discussed in the text. The displayed error bars are the standard deviation for each point in the z dimension, measured across the entire data set for each volume fraction.

structure cannot tile space, regions which include defective icosahedra deplete their neighbouring regions, resulting in larger fluctuations than would be expected for truly randomly distributed clusters. To the extent that the error allows, it appears that the distribution of defective icosahedra is flat in the z direction. This is consistent with the density profiles shown previously, and suggests that our study measurements of the defective icosahedra populations is unaffected by any emergent structure in the bulk liquid due to sedimentation. This supports the notion that the measured change in the defective icosahedra populations is due to the bulk motion created by the sedimentation. Further work which examines the z-distribution of defective icosahedra would need to collect around an order of magnitude more data to address this question more clearly.

3.3.3 Other Five Fold Symmetric Structures

This work focusses on the defective icosahedron as it is the most long lived, and therefore most stable, five fold symmetric structure in the hard sphere liquid. However, it is not the most common structure, ow-

ing to the fact that it is quite large, making it hard to form. Indeed, in our results above, the defective icosahedra only filled at most around 20% of the system, and that was at deep supercooling. In the region relevant to the nucleation discrepancy problem, Φ is around 0.52, and here we see only about 10% of the system filled by defective icosahedra. We may well be skeptical then that this structure can control the nucleation rate to the degree needed to explain the nucleation rate discrepancy. The discrepancy is almost 10 orders of magnitude, and so it seems we need a mechanism which would change the entire liquid - if there are regions which are several σ distant from a defective icosahedra (and at $\Phi = 0.52$ there certainly are), these regions should nucleate at just the same rate as the unsedimenting system. If these regions were only 10% of the entire system, then we'd expect a concomitant decrease in the nucleation rate to one tenth of its previous rate, which is nowhere near enough to explain the discrepancy.

This back of the envelope argument applies to the case that the defective iscosahedron is the only relevant five fold symmetric structure in the supercooled hard sphere liquid. In fact there are many other five fold symmetric structures which do exist at much higher populations than the defective icosahedron. The defective icosahedra population acts only as a proxy for all of these structures. This is a reasonable assumption as the same five-fold rings which are necessary for the defective icosahedron are the basic building blocks of all the other five fold symmetric structures.

However, it is possible that the defective icosahedra is not a good proxy for five fold symmetry in this case. For example, it may be that the coupling of hydrodynamics and sedimentation break up large structures *in general*, such as the defective icosahedra, whilst leaving other structures, including smaller five fold symmetric structures, untouched.

As such, we repeat our analysis for another, smaller five fold symmetric structure, the pentagonal bipyramid (also referred to as the 7A structure). This structure comprises of a single pentagonal ring with particles above and below the centre of the ring. Shown in Figure 3.9 are the populations of the pentagonal bipyramid across a range of volume fractions, and for density matched, sedimenting, and creaming data. We see a similar reduction in the quantity of the pentagonal bipyramid as was seen with the defective icosahedra. Clearly, we do not have the same numerical change - but the same biasing field strength is required to replicate the decrease in the pentagonal bipyramid population in simulation. See 3.3.4 for details.

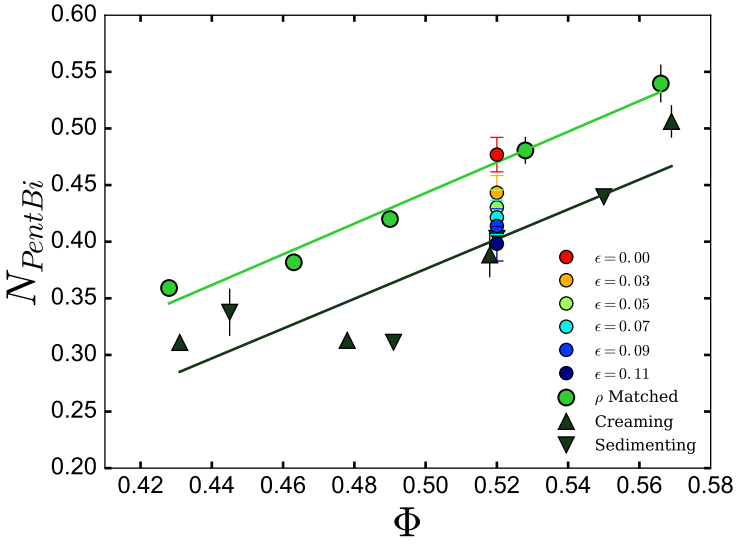

Figure 3.9: The population of the pentagonal bipyramid across volume fraction. Triangles facing up are creaming samples, triangles facing down are sedimenting samples, lime green circles are density matched samples. Fitting lines are linear fits to the density matched data and all non-density matched data, respectively. A reduction in the pentagonal bipyramid population can be seen across all volume fractions sampled for both sedimenting and creaming samples. Coloured circles at $\Phi = 0.52$ are simulation populations for various biasing field strengths, (ϵ)

3.3.4 Strength of Sedimentation Effect on Five-Fold Symmetry.

It has been shown that there is less five fold symmetry in our sedimenting experiments. What does this mean for the nucleation discrepancy between simulation and experimental HS? It is not immediately clear how much a decline in defective icosahedra populations of the magnitude shown in Fig. 3.7 will affect the nucleation rate densities. We could try to measure the effect size directly, by running confocal experiments to determine the nucleation rate densities when sedimenting. However there are two clear problems with this approach. The first is that the system is sedimenting with quite a high Peclét number, and so the emergent density profile would quite quickly emerge. The second problem is that at lower volume fractions, the nucleation rate is very incredibly low and therefore very hard to measure, and this is where the discrepancy exists.

Instead, we choose a more indirect method. Following Taffs (2016)[61], we penalise the formation of the smallest five fold symmetric structure that can be located by the TCC - the pentagonal bipyramid. Monte Carlo simulations are performed where for each pentagonal bipyramid

a particle makes up, an energetic penalty of ϵ is applied. This biases the system against the formation of five fold symmetric structures. As we increase the size of ϵ, fewer and fewer pentagonal bipyramids (and therefore all other five fold symmetric TCC structures) are formed. The simulations themselves were performed by Dr John Russo, and all analysis was performed by the author.

We are interested in the value of the penalising field which causes a reduction of defective icosahedra populations equal to that seen in our sedimenting experiments. We take 100 configurations of 500 particles at each field strength, meaning the sample size is the same order of magnitude as the experiments, and the error on the populations is similar. We choose a volume fraction of $\Phi = 0.52$ for these simulations. This value of Φ is chosen because it is the value at which the nucleation rate density discrepancy is largest, and therefore where our hypothesis of sedimentation coupling to five fold symmetry must do the "most work". If our effect size is large enough to explain the discrepancy at this supersaturation, it would be very surprising if it didn't explain the discrepancy at higher supersaturations. This is especially the case given that the reduction in defective icosahedra on sedimentation is reasonably constant across volume fraction, whilst the nucleation rates changes very rapidly.

Fig. 3.10 shows the behaviour of the defective icosahedra populations with the biasing field strength. When there is no field ($\epsilon = 0.00 k_B T$), the population matches our density matched result well. As we turn up the field strength, the population of defective icosahedra is reduced. At a field strength of around $\epsilon = 0.07 k_B T$, the defective icosahedra populations match the sedimenting/creaming trend line from Fig. 3.7. Increasing the field strength further results in an overshoot of the sedimenting/creaming trend. This behaviour and final value match the analysis of the pentagonal bipyramid quite well (see Fig. 3.9). Here, the trend lines are matched at rather larger values of ϵ, around $\epsilon = 0.11 k_B T$.

We choose a field of $\epsilon = 0.07 k_B T$, as it results in a defective icosahedra decrease equal to that of our sedimenting experiments. By performing umbrella sampling, it is possible to calculate the nucleation barriers in the case of the field being applied and in the normal, unbiased hard sphere case. The result is shown in Fig 3.11. Clearly, five fold symmetry reduction of the size that we see in our sedimenting experiments is very important for the nucleation rate density. Reductions of many $k_B T$ in the barrier are highly meaningful. We therefore proceed to try to quantify how meaningful more precisely, to see if this effect can resolve the nucleation rate density discrepancy.

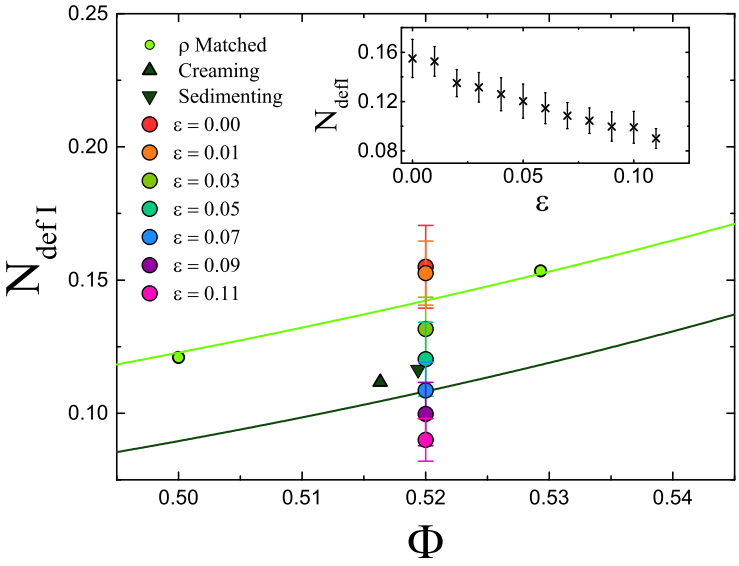

Figure 3.10: The effect of applying an effective field which biases against the formation of five fold symmetric structure. As ϵ increases, the quantity of defective icosahedra is reduced. For context, we show a zoomed in version of Fig. 3.7, with the biased simulation results overlaid. Shown in the inset is the dependence of the defective icosahedra populations on the field strength, which is linear to good approximation. Error bars are the standard deviation of all 100 configurations.

3.3.5 Change in Nucleation Rate Densities

From these barriers, we can calculate nucleation rate densities. We know that the nucleation rate density is related to the nucleation barrier height as in Equation 3.1.

$$J = \kappa e^{-\Delta G_{crit}/k_B T} \tag{3.1}$$

Where κ is the kinetic prefactor. We know ΔG_{crit}, which is simply the maximum value of the nucleation rate barrier. The kinetic prefactor, κ is given by $Z\rho_l f^+_{n_c}$, where Z is the Zeldovich factor, ρ_l is the number density of the liquid, and $f^+_{n_c}$ is the attachment rate of particles to the cluster. The Zeldovich factor can be found from the second derivative of the nucleation barrier[105], and ρ_l is known perfectly from the simulation parameters. Finding the attachment rate requires further simulations, we use results given in Auer and Frenkel (2004)[122]. These results, though are not at the exact volume fractions we use, so we take a simple linear interpolation between their points to approximate the relevant values at our points. There will therefore be an error of around an order 2 on our nucleation rates, which is

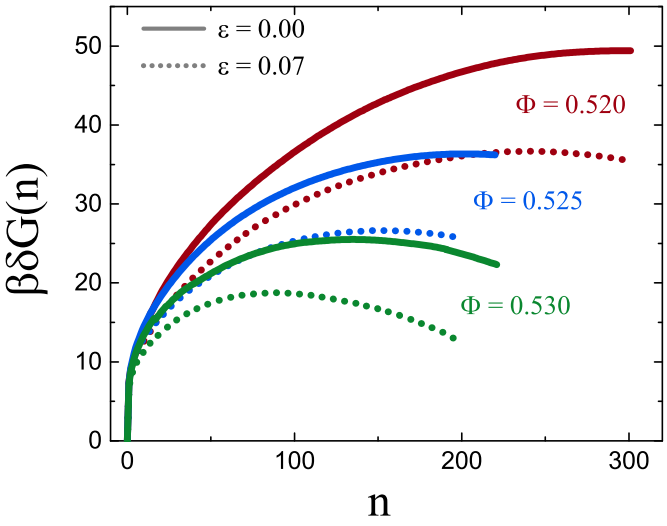

Figure 3.11: The nucleation barrier for hard spheres with no biasing (solid lines), and with a bias against pentagonal bipyramids equal to $\epsilon = 0.07$ (dashed lines). This is performed across three different volume fractions. The effect of less five fold symmetry is to substantially reduce the nucleation barriers (and therefore substantially increase the nucleation rate densities). For the lowest volume fraction $\Phi = 0.52$, this change in barrier height is around $11 k_B T$.

fairly small. Also, as the first Auer and Frenkel point is at $\Phi = 0.5207$, the most important data point at $\Phi = 0.52$, has only a very small error caused by the interpolation.

We plot the new nucleation rate densities in Fig 3.12. Clearly the change in five fold symmetry has substantially altered the nucleation rate densities, in fact, the new perturbed data seems to agree quantitatively quite well with the weakly sedimenting experiments.

3.3.6 Effect on the Nucleation Discrepancy

We have shown that sedimentation brings about a substantial decrease in the populations of 5-fold symmetric clusters in the supercooled hard sphere liquid, and that this change makes a difference to the nucleation rates of many orders of magnitude. However, this fails to resolve the nucleation discrepancy, because the Peclét number used in this work (1.5) is substantially larger than that used in the literature experiments. This issue is especially pronounced for those experiments which are in the slowly sedimenting arm, which use microgels or small

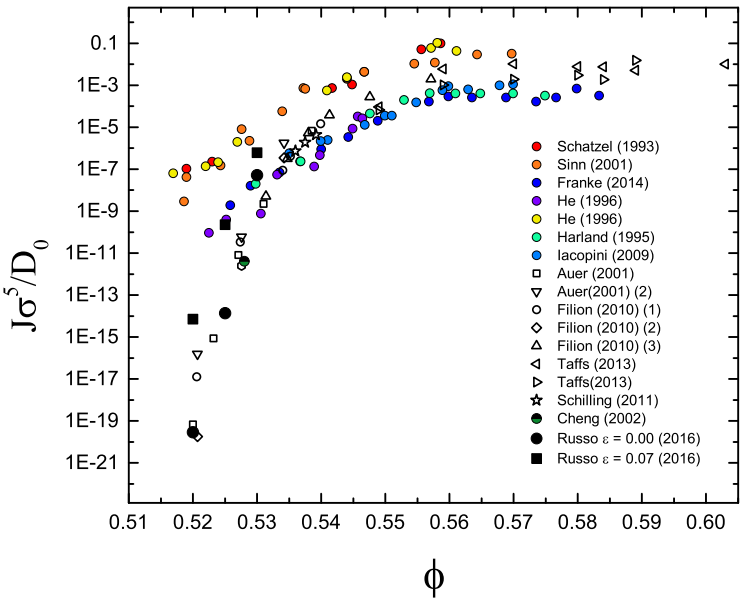

Figure 3.12: Nucleation rates of the literature for hard spheres, as seen previously. New points are shown in black filled circles and squares. Squares are perturbed simulations, with the same population of defective icosahedra as in our sedimenting experiments. Circles are unperturbed hard spheres. There is a clear difference in the nucleation rate caused by the change in symmetry, of up to order 10^5 for the $\Phi = 0.52$ case.

PMMA, as they have Peclét numbers around an order of magnitude lower than this.

We could probe the effect of substantially smaller Peclét numbers on the population of defective icosahedra. However, it will likely be very difficult to resolve the effect of the sedimentation, our defective icosahedra populations are different only by a few percent at high volume fractions, and this is near the edge of our resolution ability. Reducing the Peclét number by, say, an order of magnitude, will require us to discern changes in the populations of a few fractions of a percent, and without a huge data collection effort this will be very challenging.

To illustrate the likely effect on the nucleation rates at low Peclét number, we instead interpolate the effect through the region below our experimental results. We know that a Peclét number of 1.5 corresponds to a penalising field strength of $0.07 k_B T$, and that this results in a change in the nucleation barrier height of $11 k_B T$. Further umbrella sampling results at lower field strengths give quite a linear dependence of the barrier height on the field strength, down to a field strength

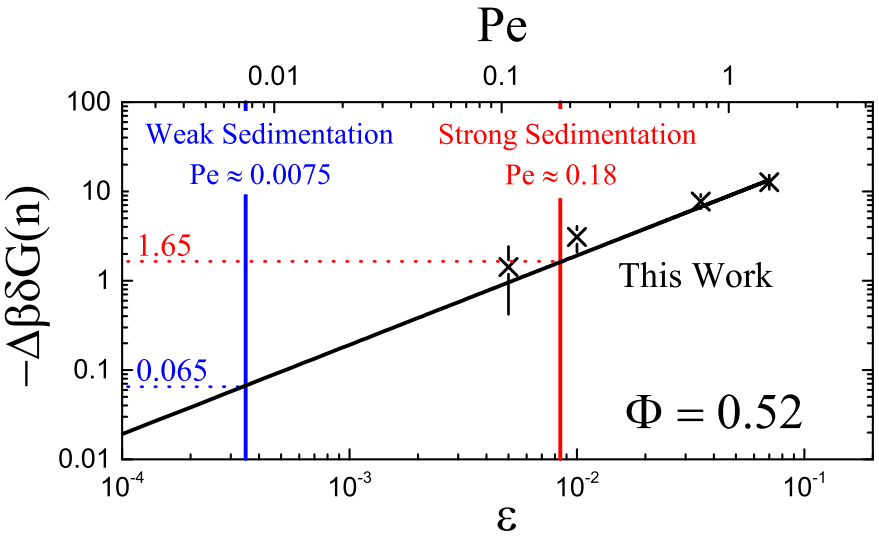

Figure 3.13: Interpolating our barrier height changes due to sedimentation down to lower Peclét numbers, which are representative of the degree of sedimentation present in the scattering experiments. This interpolation is performed at a volume fraction of $\Phi = 0.52$, where the discrepancy is largest.

of $0.005 k_B T$. We cannot probe field strengths any smaller than this as the error on the barrier height is around $1 k_B T$, and smaller fields will perturb the barrier by less than this error. We also know that when there is no gravitational field, there can be no change in the nucleation barrier height. Overall, this gives us a reasonable linear dependence of the barrier height on the size of the penalising field, and the result is plotted in Fig. 3.13.

Given this linear dependence, we see that in the case of the strongly sedimenting experiments, there is a reduction in the barrier height of $1.65 k_B T$, and for the weakly sedimenting experiments, there is a reduction of $0.065 k_B T$. We therefore expect the strongly sedimenting experiments to nucleate around 5 times faster than the weakly sedimenting experiments. This resolves a part of the nucleation gap between the two experimental arms, but fails to explain the discrepancy between experiment and simulation.

Further work could focus on clarifying the various dependencies between the different variables. For example, does the defective icosahedra population fall linearly with decreasing Peclét number? It is possible that the hydrodynamics brings about quite large effects even for small amounts of sedimentation, as it can do for the sedimentation velocities[130]. If this is the case, then sedimentation and hydrodynamics may play more of a role in the nucleation discrepancy than we measure. Further work could also examine different couplings between

the field and the liquid, beyond that of five-fold symmetry. Even better would be to directly measure the nucleation rates of hard spheres with sedimentation and hydrodynamics, but this is very challenging in experiments (systems will fully sediment before nucleating at low supersaturations) and in simulations (which will need to include hydrodynamics with rare event sampling). A limitation of this work is the size of the particles required. However, smaller particles could be imaged with the use of super-resolution microscopy techniques[60]. This would allow for direct measurements of nucleation rates in the weakly supercooled regime, which can cross check the results of the light scattering experiments.

4

DENSITY FLUCTUATIONS IN EXPERIMENTAL HARD SPHERE LIQUIDS

4.1 INTRODUCTION

The experimental literature review in 1 concluded that sedimentation is the most promising potential avenue for explaining the increased nucleation rate density. Section 3 explored the possibility that the mechanism for this process is the coupling of sedimentation to five fold symmetry. In this chapter we address whether sedimentation is coupling to density fluctuations. The term density fluctuations refers to the tendency of liquids, over short time and length scales, to include regions with a density different to that of the bulk liquid density. Density fluctuations may be important in the formation of the crystal, as during the pre-nucleation stage the liquid has regions which become both denser and more crystal-like in their ordering[37], from which nuclei form.

In fact, the presence of long range correlations in sedimenting suspensions is well known. In 1997, Segrét *et al.* measured the spatial correlation function of the velocity fluctuations, finding that they are correlated on a scale of around 20 particle diameters[181]. This result has proved robust for volume fractions from 10^{-4} to 0.4[182,183]. Moreover, the amplitude of these fluctuations grows with increased packing fraction[184], suggesting that they may become important at the high packing fractions needed for crystallisation to occur. However, the velocity fluctuations are complex, their time-dependent behaviour is strongly influenced by the container size and shape[185]. The velocity fluctuations themselves are intimately connected to the density fluctuations, as regions with higher or lower densities will tend to have higher or lower (respectively) sedimentation velocities[186]. Despite this, the amount of work that examines the microstructure of the sediment is limited, and the results are contradictory, with some suggesting that density fluctuations are enhanced by sedimentation, and others suggesting they are suppressed[184]. It should be noted that most of the work cited in this discussion is in the very high Peclét number regime, in which the sedimentation dominates thermal fluctuations. The situation is even more unclear for weakly sedimenting systems of the type used when studying hard sphere nucleation ($Pe < 0.5$).

Recent work[132] has examined density fluctuations and the impact they have on nucleation rates. The work of Bonn *et al.* uses a very similar experimental methodology to this work - PMMA spheres suspended in a density-matching mixture of CHB and cis-decalin, imaged by confocal microscopy. After particle tracking, the nuclei are identified using a local bond-order analysis. By examining the size distribution of the nuclei, energy barriers can be calculated (see Chapter 5 for more details). The authors examine nuclei found within regions of a particular local density, and plot the energy barriers for nuclei at these local densities. Their nucleation barriers collapse onto the same curve to within reasonably good agreement, and the authors claim that this demonstrates that density fluctuations are not important to nucleation. However, it appears that the measurement of the local density is done *post hoc*, after the nucleus has already formed. Therefore, what the measured nucleation barriers are telling us is that the local density of the liquid surrounding a nucleus is independent of the size of the nucleus, which seems unsurprising. As such, this work does not rule out density fluctuations as a possible mechanism to higher nucleation rates in experiments. See section 1.5.4 for a full discussion of this work.

4.2 ALGORITHM

In order to study the magnitude of the density fluctuations in our colloidal liquids, a simple algorithm was designed. This algorithm operates on the "centers" files given by the tracking algorithm. These files are simply the positions of each particle identified in the confocal image. Generally there are on the order of 10^4 particles per 3 dimensional image stack. This means that we can obtain fluctuation distributions with good statistics from a single stack of images, and excellent statistics when using multiple stacks taken from the same sample.

The algorithm operates by examining each particle in turn. It calculates the distances of every other particle from this sample particle. It then counts the number of particles within a threshold distance, which is the only free parameter of the algorithm. The number of particles within this threshold distance is then divided by the volume of the binning sphere to arrive at a number density. This binning sphere is simply the spherical volume defined by the threshold distance we choose. By multiplying the number density by the volume of an individual particle, a local volume fraction for each particle is calculated. A full schematic of this method is shown in Fig. 4.1.

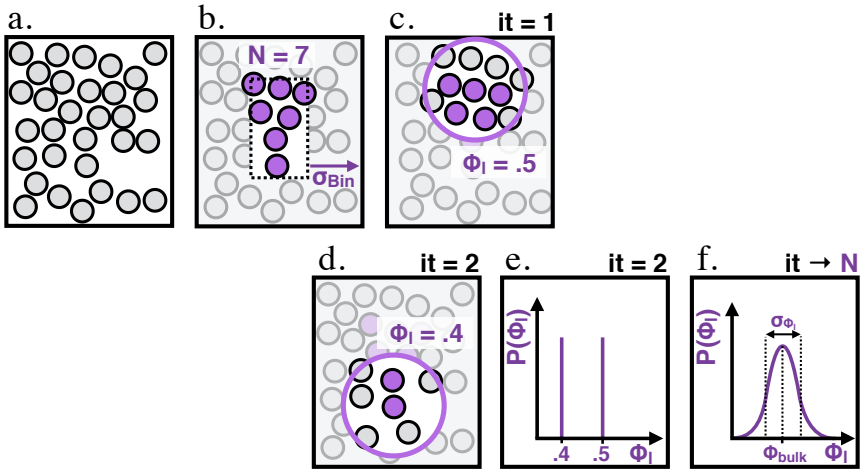

Figure 4.1: A schematic illustration of the method used to quantify density fluctuations in this chapter. **a.** A typical liquid configuration of interest. **b.** We examine those particles which lie within a binning distance from the edge of the box, shown in purple. Using other particles would result in the bin extending outside of the box range. The number of particles in the box, $N = 7$. **c.** On our first iteration, the first particle is considered, and the number of neighbours is counted. In this case $n = 10$, resulting in a local volume fraction $\Phi_l = 0.5$. **d.** On our second iteration, our second particle is considered, and the number of neighbours is counted. In this case $n = 6$, resulting in a local volume fraction $\Phi_l = 0.4$. **e.** The measured local volume fraction are binned into a histogram. **f.** As the number of sampled particles tends to N, the histogram becomes normally distributed, with a mean value equal to the bulk volume fraction Φ_{bulk}. The standard deviation of this distribution σ_{Φ_l} is our final measurement of the density fluctuations.

The particles in the centres file will lie at different distances from the edges of the sample. Particles within a binning sphere radius of any of the edges cannot be the centres of a local volume fraction calculation, as a part of the binning sphere will lie outside of the sample, and the volume fractions calculated will be artificially lowered. The solution to this problem is to test whether each central particle is further than a binning sphere radius from every wall and pass over those that are not. This reduces the number of particles considered, and thus results in a smaller sample size. This could be ameliorated by calculating the true volume of the sphere which could be occupied by particles, however as the statistics on the local densities are extremely good without this procedure, it was deemed unnecessary.

In simulations, no particle lies near the edge of a sample, because the simulations use periodic boundary conditions. In simulation then, no particles are lost to the edge of the wall, and the local density of every particle can be sampled. All that is necessary is to take into account the periodic boundary conditions when calculating the distances between the sampled particle and every other particle.

4.2.1 Choice of binning distance

The choice of binning distance is important. If the binning spheres are too large, any local fluctuations will be washed out. Too small, however, and the density fluctuations become dominated by small tracking position errors[187].

A desired property of the analysis is for the mean local volume fraction be equal to the bulk volume fraction of the entire sample. This can quite easily not be the case, especially at fairly high volume fractions. For example, take a binning sphere with a radius just over 1σ. This binning sphere will generally contain the all of the first "shell" of local neighbours. The full volume of these neighbours will be counted as existing in the binning sphere, and the calculated local volume fraction will be quite high, indeed it could be above 1.0. If we increase the radius of the sphere from here, there will only rarely be new particles and so the local volume fraction will drop. This will remain the case until the second "shell" of neighbours is crossed, when the local volume fraction will increase again.

In this way, the local volume fraction binning mirrors the radial distribution function, $g(r)$. This is shown in Fig 4.3 It is therefore simple to choose a binning distance where the mean local density equals the bulk density - simply choose a distance where the $g(r) = 1$.

There are clearly many values of r where $g(r) = 1$. We wish to choose a value which captures the local density in the region of a single particle, but if a value is chosen that is too small, a single particle moving in and out of the desired region could result in a substantial change to the local number density, and the error on our final measured standard deviation will be relatively high, meaning more particles will need to be measured. This means more samples being imaged and more (computationally costly) particle tracking. Furthermore, if a small value of r is chosen, this can lead to problems in choosing the value of r such that $g(r) = 1$. This is because the derivative of the radial distribution function is high at small r - small changes in r lead to large changes in the $g(r)$. Small errors in our measured σ can therefore lead to large changes in the final average

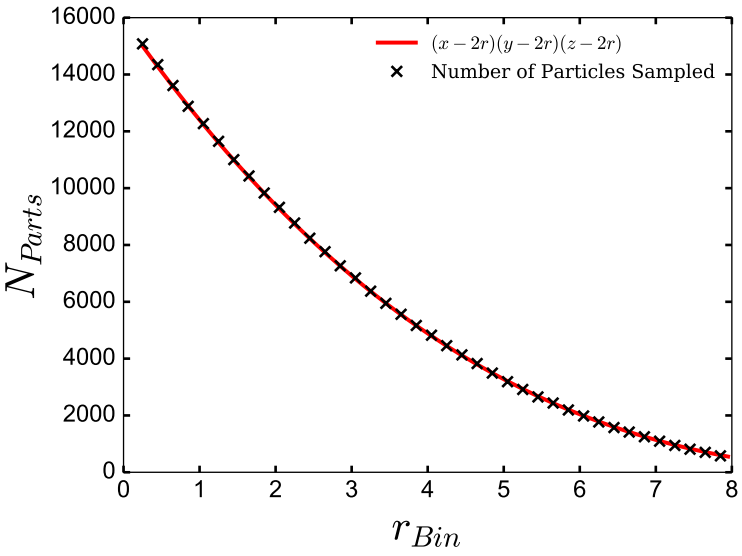

Figure 4.2: The decrease in the number of particles sampled as the binning sphere radius is increased. The red line is a fit to the expected behaviour - the particle number should fall off with the volume of the restricted box. The $(x-2r)(y-2r)(z-2r)$ fit is also multiplied by $N_{parts}(0)/V_{box}(0)$. in order to give the correct starting value.

number density. As such, it is good to choose a reasonably large value of r.

On the other hand, choosing a value of r which is too large will wash out the local density fluctuations, and every bin will be found to contain the number of particles which correspond to the bulk number density. Also, small bins are desired as more particles can then be examined, particles which lie closer than r to a wall are not included. As r increases the number of particles included is therefore reduced. This reduction goes as $N \propto (x-2r)(y-2r)(z-2r)$, where x, y, and z are the imaging dimensions. See Fig. 4.2 for the dependence of the sampling size with respect to the binning sphere radius.

Given these considerations, we choose a value of r equal to 3.25σ. This r gives a mean local density value equal to the bulk number density. It also gives a reasonably wide distribution of the local densities. This value of r does mean many particles cannot be sampled - in fact over half of particles are too close to the edges to be sampled. However, this reduction does not compromise our statistical power enough to be an issue - we can determine the mean and standard deviation of the local densities to good error.

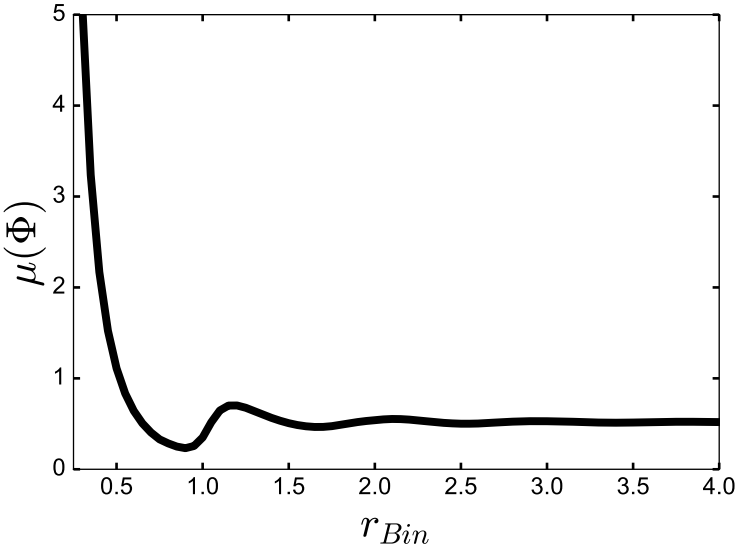

Figure 4.3: The change in the average local density with the size of the binning sphere. The bulk volume fraction for this sample is 0.5, and it can be seen that at large bin lengths the average local volume fraction tends to this value.

4.3 SIMULATION DETAILS

In order to compare our experimental results to perfect hard spheres, we run molecular dynamics simulations of hard spheres. These simulations use the DynamO event-driven package[188]. The simulations hold the number of particles, the box volume, and the temperature constant (the NVT ensemble). In order to prepare configurations of hard spheres at equilibrium at the appropriate volume fraction, we first seed a crystal of 2048 particle in a large box. On running the simulations with an Anderson thermostat for one million timesteps, the crystal melts and the system becomes a very low density liquid ($\Phi = 0.05$). We then use DynamO's compression engine to slowly reduce the size of the box until the desired volume fraction is reached. The simulation is run forward for ten million time steps to equilibrate the configuration at the new density. To collect data, every one million time steps the configuration is saved, and the simulation is run for as many time steps as required to generate the desired amount of data. In the work in this chapter, generally 20 configurations are used for each calculation, meaning the statistical power (around 40000 particles) is of the same order as that of our experimental configurations.

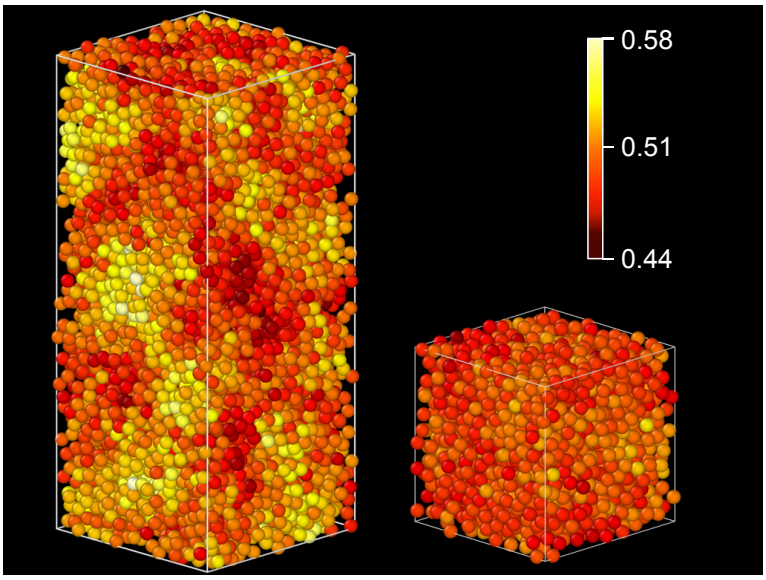

Figure 4.4: A snapshot of an experimental configuration (left) and a simulation configuration (right), with each particle colour coded according to their local density. Both systems have a bulk volume fraction of $\Phi = 0.51$. Only those particles far enough away from the edges of the system to have a calculated local density are included in these images.

4.4 DENSITY FLUCTUATION RESULTS

Shown in Fig. 4.4 is a visualisation of density matched experimental and simulation data, at the same bulk volume fraction, after the local densities have been calculated. It can be seen that there are reasonably large domains of both high and low densities in the experimental case, but in the simulation the fluctuations about the mean are much smaller. The full distribution of these fluctuations is shown in Fig. 4.5.

Fig. 4.5 shows that both experiment and simulation follow normal distributions, centred about the bulk mean volume fraction of the configurations (as would be expected). However, the experimental distribution has a much wider distribution than the simulation distribution. This can be seen in the standard deviations, which for the experimental distribution is 0.020, whilst the simulations have a standard deviation of just 0.011 (expressed as volume fractions).

We therefore see a quite substantial discrepancy in the density fluctuations in our experimental data and our simulation data. This seems very promising - a liquid with a wider distribution of local densities might well be expected to nucleate faster. After all, bulk systems at higher densities nucleate orders of magnitude more quickly than systems just a few percentage points less dense. In our experimen-

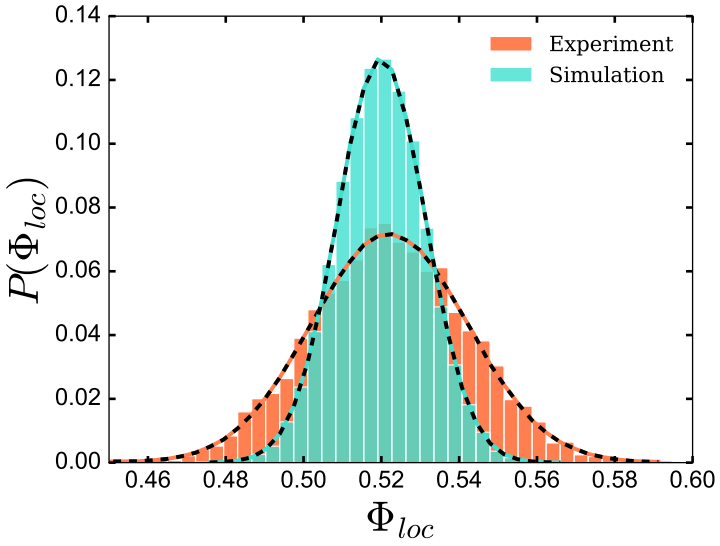

Figure 4.5: The probability of a particle being found to have a given local volume fraction. Shown in orange is the experimental configuration from Fig. 4.4, and in turquoise is the total distribution from 20 simulation configurations of 2048 particles each, including the simulation configuration from Fig. 4.4. This is not a continuous probability density function, as each particle found in the binning sphere adds a set amount of "local density", meaning that the local density has a discrete set of possible values. Shown in turquoise-black and orange-black dashed lines are normal distributions of the same mean and standard deviation of the simulation and experimental fluctuations respectively. This demonstrates that the fluctuations are normally distributed.

tal systems, there are many more regions at relatively high volume fraction than in our simulated systems. Nuclei may well preferentially emerge from these regions, which could partially explain the nucleation rate discrepancy between simulation and experiment.

4.5 DENSITY FLUCTUATIONS - MECHANISM

If we wish to claim that the change in the distribution in the local densities explain part or the entirety of the nucleation rate discrepancy, we need to understand the mechanism underlying it. If this mechanism is due to something fundamental about the experiments which would be replicated across all of the literature work, we can say that the fluctuations may be causing the discrepancy. If, however, the fluctuations emerge due to a more system-specific mechanism, they will not help to explain the gap. For example, if the fluctuations are due to some electrostatic effect that is unique to our solvent and salt choice, that

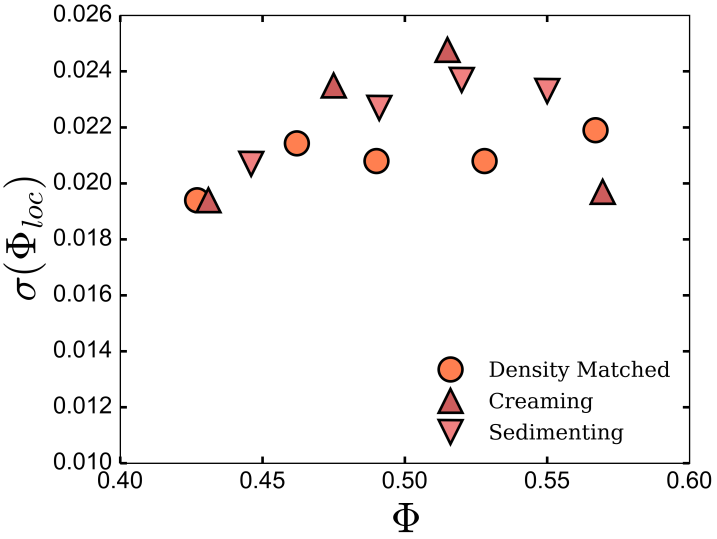

Figure 4.6: The size of the density fluctuations for all of the data taken in the previous chapter. This allows us to study the effect of sedimentation on the fluctuations. The y-axis is chosen to drop to 0.01 as this is roughly the size of the fluctuations in the simulations.

will not be enough, as different experiments in the literature do not use this system. Similarly, if the mechanism is an error in our confocal measurements, this will not explain the discrepancy, as the literature work uses scattering techniques which will not be affected by these errors.

4.5.1 Sedimentation

The immediate first test is whether these fluctuation differences are caused by the sedimentation of colloids. Fortunately, we already have the data for this test. By running our fluctuation algorithm on density matched, cis-decalin rich, and CHB rich samples, we can see if the sedimentation rate controls the fluctuations.

Fig 4.6 shows the result of running the fluctuations code on all of the data from the previous chapter. There seems to be a small trend at intermediate volume fractions ($0.47 < \Phi < 0.55$), where the sedimenting or creaming points are around 10% larger than the density matched points. However, at higher or lower volume fractions the sedimenting data is similar to, or below, the density matched trend. Given that the simulation fluctuations are much lower than 90% of the density matched data (closer to 50%), it therefore seems very unlikely that the tiny amount of sedimentation present in the density matched experiments could explain the anomalous fluctuations. The apparent

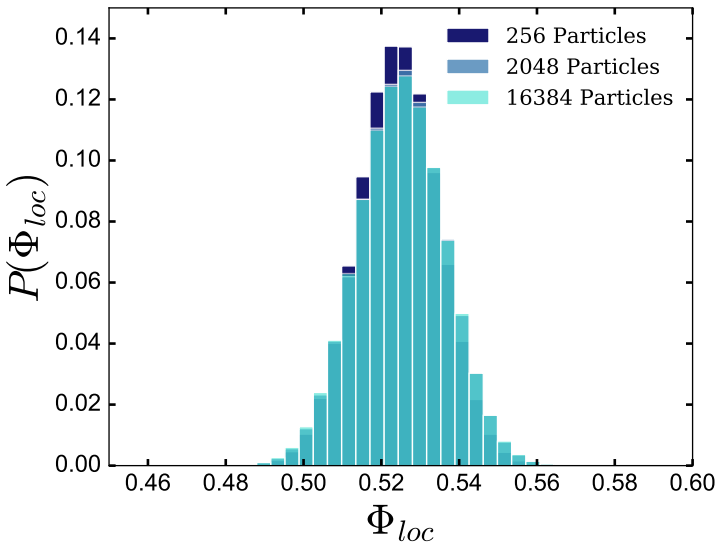

Figure 4.7: The effect on the local density distribution in simulations when changing the system size. We observe only a very limited change.

trend may simply be due to experimental noise. Alternatively, these small differences may in fact be caused by the sedimentation, but given that the difference in Peclét number behaviour between the creaming/sedimenting samples and the density matched samples is much higher than the difference between the density matched samples and ideal non-sedimenting experiments, the sedimentation alone is not a strong enough effect to resolve the discrepancy.

4.5.2 Simulation Parameters

There is some possibility that our simulations are incorrect, for example, maybe the system size is too small and our low fluctuation measurement is due to a finite size effect. We therefore run simulations with different box sizes. The first is a much smaller box with just 256 particles, which should suppress fluctuations if they are caused by a finite size effect. We also run simulations with a much larger box, with 16384 particles. This box is close to the size of the experimental systems and so should be able to capture fluctuations as they exist in the experiments. All these simulations are run at the same volume fraction of just over $\Phi = 0.52$.

The result can be seen in Fig. 4.7. Clearly little difference is made to the fluctuations by the system size. There is in fact a very small trend in the fluctuation standard deviations which is hard to see in this figure, the 256 particle system has a standard deviation of 0.0104, the 2048 system has a standard deviation of around 0.0112, and the 16384

system has a standard deviation of 0.0113. There therefore probably is a small system size effect, with the smallest systems unable to properly explore the whole range of local densities. This effect is small, however, and certainly does not explain the difference between the experiments and the simulations.

We also checked to see if the simulation ensemble changes the density fluctuations. We ran simulations with 2048 particles at a volume fraction just over $\Phi = 0.52$ in the NVE, NPT, and NVE ensembles, but again we found that there is almost no difference in the density fluctuations.

4.5.3 Imaging Parameters

When we image our colloidal systems, certain decisions have to be made about the imaging parameters. These include choices like the laser power, number of scans per image, aperture size, and others. Generally these parameters are chosen to ensure a Gaussian distribution of the pixel intensities, and if the tracking delivers an accurate radial distribution function and topological cluster classification results the imaging parameters are taken to be acceptable.

However, it is possible that the choice of imaging parameters is affecting the density fluctuations, whilst leaving these other order parameters unaffected. Two parameters in particular which may do this are the laser intensity and the image averaging. The laser power affects the overall image intensity, and is generally chosen to give the widest possible dynamic range in the images (background at with an intensity of zero and the most intense points at an intensity of 255), whilst being low enough not to saturate the image. The laser, however, may potentially heat the imaged region as it is scanned, leading to a heterogeneous temperature field across the sample. This could affect the structure of the colloidal liquid by creating non-equilibrium solvent flows. The image averaging, meanwhile, is chosen to reduce noise in the image, at the cost of increasing the time to take the images. So long as the timescale to take the images is substantially below the time for the colloidal particles to diffuse their radius, this should make little difference to the final measured structure. In fact, the discrepancy in the fluctuations grows with the volume fraction, which is likely to be in the wrong direction. Higher volume fraction samples relax more slowly, and so the impact of the averaging should be lower, not higher, at higher volume fractions.

To test the effect of the laser power on the fluctuations, we run an experimental sample at $\Phi = 0.51$. We then take several image stacks,

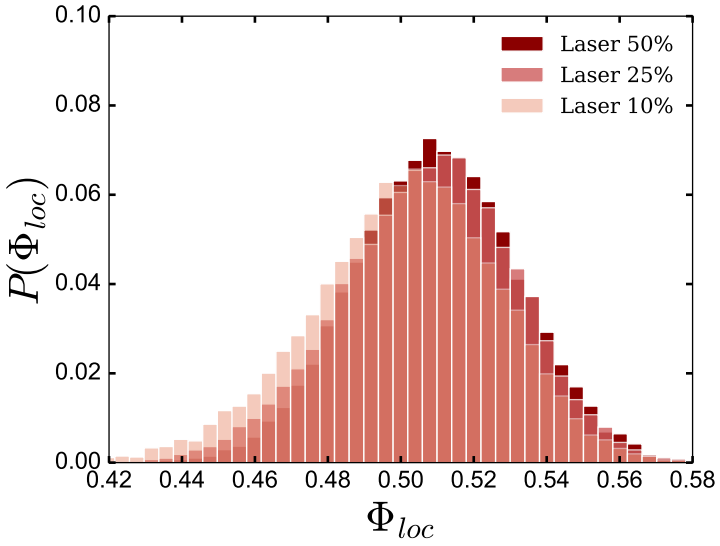

Figure 4.8: The effect on the local density distribution in experiments when changing the laser power. Only a limited difference is seen between the three distributions.

at different laser powers. We choose laser powers of 10%, 25% and 50% of the highest possible laser intensity. Choosing values higher than 50% led to unavoidable oversaturation of the image, which would lead to poor tracking, whilst values less than 10% led to low intensity, noisy images. We attempted to track an image taken at 5% laser intensity, but found that our final calculated volume fraction was substantially lower than that of the other three data points due to the tracking missing particles. The images themselves are taken in different places within the sample, to ensure that the potential effects of the imaging process are not compounded in each new data set.

Fig. 4.8 shows the result of this experiment. The standard deviation for the 50% distribution is 0.0224, for the 25% distribution it is 0.0237, and for the 10% distribution it is 0.0256. Clearly, whilst there are small changes to the distributions with different laser power, there is not a substantial enough effect to suggest that the laser power is the cause of the fluctuation difference. Whilst there is a trend, with the laser power generally decreasing the width of the local density distribution as it increases, this is in the opposite direction to the trend we would expect. The high the laser power, the more the experimental system is being perturbed, and yet the less it appears to differ from the simulation result. As such, we conclude that this trend is likely just experimental noise.

A similar experiment was performed to establish the effect of the image averaging on the density fluctuations. Different regions were

Table 4.1: The size of the density fluctuations for different amounts of averaging.

Averaging Interations	Fluctuation Size
2	0.0230
4	0.0225
8	0.0248
16	0.0246

selected from a sample prepared at $\Phi = 0.51$ with increasing amounts of averaging for each. The results can be seen in Table 4.1. The results are familiar, with little clear systematic difference being made by the averaging which might help to explain the large experimental fluctuations.

4.5.4 Boundary Conditions

One of the key differences between the simulations and the experiments during analysis is the way the boundaries are treated. Simulations have a periodic boundary whereas experiments are sharply cut off at the edges of the image. Small mistakes in how either boundary is handled could lead to changes in the fluctuations. These would mostly be due to errors in our code. We therefore check to see if proximity to the boundary makes any difference to the density fluctuations.

Shown in Fig. 4.9 are average density fluctuations in a simulation and experiment, both at $\Phi = 0.52$. Here we are examining the local densities for slices of particles a given distance from a boundary, and finding the standard deviations of these sub-populations, and then binning across every slice. Clearly the simulation fluctuations are smaller throughout, as expected. However, there is no clear trend in this data that suggests that the difference between experiments and simulation might be due to problems with handling the boundaries, as the density fluctuation profiles do not clearly peak or dip near the boundaries.

4.5.5 Polydispersity

One parameter which is hard to control in our experiments is the polydispersity of the colloidal particles. We can get some measure of this using DLS and SEM imaging. Both have their limitations. SEM imaging measures the particles whilst dry, and it is known that PMMA

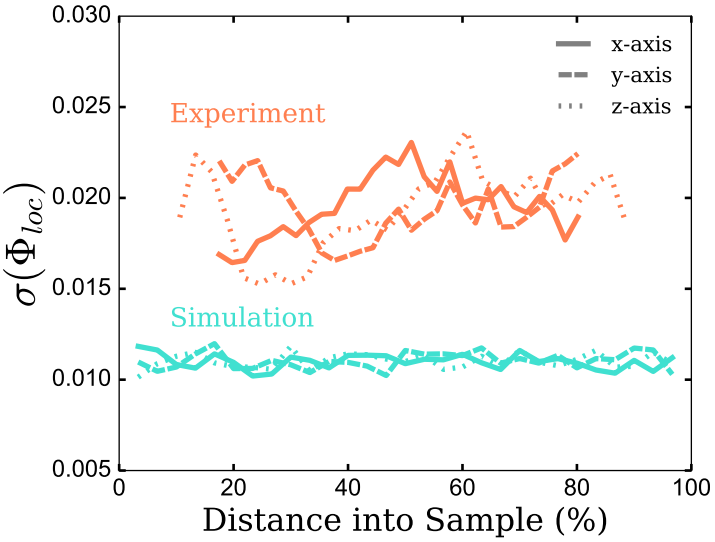

Figure 4.9: The density fluctuations according to position within the image, for both simulations and experiment. Simulations encompass more of their "sample" as they have periodic boundaries, meaning local densities can be calculated for all particles in the simulation configuration. The experiments are more restrained, as the particles at the edge of the configuration are ignored.

swells slightly in CHB[76]. Different particles will have slightly different PMMA network structures, for example the density of the particles will likely have a narrow distribution. Furthermore, moving from SEM images to distributions of sizes requires either image analysis or manual measurement. This often uses some sort of thresholding and labelling, which can be prone to error. They are at least dependent on the correct choice of threshold, which can be underdetermined by the image itself. It is also possible to analyse these images by eye, though that incurs its own human error (in fact it is likely that eye measurement will increase measured polydispersity artificially). DLS is an alternative technique, but as it only measures the hydrodynamic radius of particles, it is prone to missing asphericity, and there is always some experimental error on the measured polydispersity.

The upshot of this is that our experimental particles have a finite and somewhat uncertain polydispersity. It is possible that this polydispersity leads to higher density fluctuations as larger particles will allow fewer particle in their local region, whilst smaller particle will allow more. To check this, we run simulations which include polydispersity (see Fig. 4.10). This is done by running DynamO simulations as in section 4.3, except with each particle size diameter drawn from a

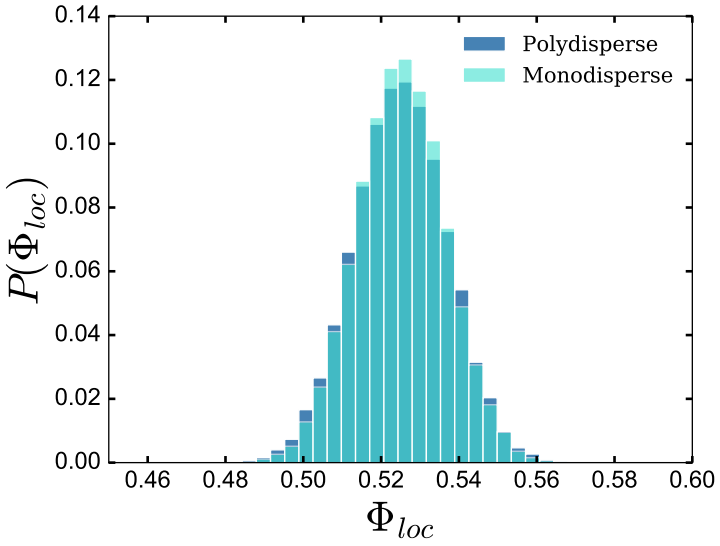

Figure 4.10: The effect of polydispersity on the density fluctuations of a simulated hard sphere system. We see a slight broadening of the distribution.

Gaussian distribution centered on 1.0 and with a standard deviation of 0.045, to match the size polydispersity of the experimental system.

Shown in Fig. 4.10 is the local volume fraction distribution for monodisperse and polydisperse hard spheres, both at a volume fraction of around 0.52. The standard deviation in the polydisperse case is 0.0120, and in the monodisperse case is 0.114. This means there is a difference of around 5%. Whilst the polydispersity does increase the density fluctuations, it again does not explain the fluctuation difference seen betwen simulations and experiments.

This seems to rule out polydispersity. However, there's some possibility that the experiments are fractionating to a higher degree that the simulations. Even systems with low polydispersities like these are prone to some degree of fractionation[189]. If larger particles in the experiments are grouping together, they might be forming regions of particularly low apparent density, whilst the small particles would form regions of particularly high apparent density, spreading the local density distribution. We can check for this possibility using the radii of the experimental particles. Our tracking package, Colloids[150], gives us these radii from its Multiscale algorithm (see section 2.8). We can plot these detected radii against their local density to check for a correlation. A probability distribution of these two variables is shown in Fig. 4.11. We see no apparent correlation between detected size and detected local density, the distribution is almost perfectly symmetric through the mean density, implying that large and small particles are

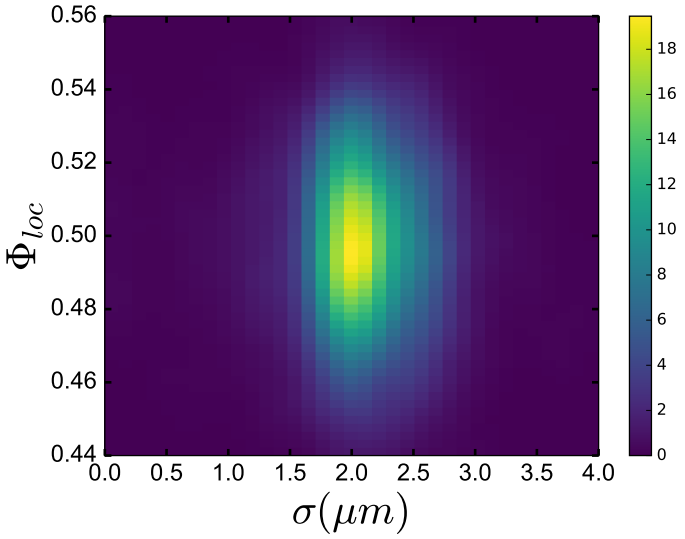

Figure 4.11: A 2d probability distribution showing the relationship between measured particle size and local volume fraction. This sample has a bulk volume fraction of $\Phi = 0.50$.

just as likely as each other to be in the highest density or the lowest density regions. In fact, there must be some small correlation, as large particles by definition must be in less dense regions as they take up more space than small particles. However, as our bin size is large this effect is too small too see in this data. The distribution of sizes in the figure is wider than that previously shown for this particles (see Fig. 3.2). This is because the tracking sizing results are less accurate that those taken by SEM, due to particle motion, blurring in the z dimension and lower resolution images. However, we would still expect any substantial trend in the local densities to be visible.

4.5.6 Potential

Our colloidal particles, to good approximation, interact through a hard sphere potential. However, there is some residual, unscreened charge, and our PSHA hairs will give a repulsion which increases over a moderate length scale (some tens of nanometers[86]), rather than an instant jump to very high values. It is possible that this slightly more repulsive potential could change the density fluctuations in our experiments. There's also some possibility that the PSHA hairs are not stabilising the particle well, and this is resulting in particles clumping together through attractive Van der Waals forces. We therefore run simulations of attractive Square Well and truncated-Morse - Yukawa

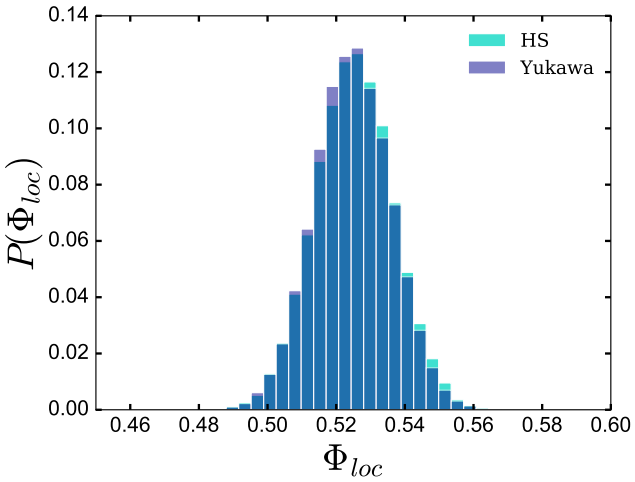

Figure 4.12: The effect of implementing a nearly Hard Sphere Yukawa potential on the density fluctuations in our system.

parameters, to see if small perturbations to the hard sphere potential could explain the density fluctuation disagreement.

4.5.6.1 Yukawa

Previous work has already identified truncated-Morse Yukawa parameters which closely track the real degree of charging in our system[62]. The truncated Morse potential generates a very steep potential below $r = \sigma$, modelling the steric hard sphere repulsion. It is truncated at $r = \sigma$, where it is equal to 0. The Yukawa potential component generates a long range repulsion at distances larger than $r = \sigma$, which models the small repulsions induced by the incomplete charge screening[190]. The truncated-Morse Yukawa potential is give in equation 4.1. The work of reference[62] matched the radial distribution function of particles of the same size and suspended in the same solvent as this work with that of simulated particles at a known set of truncated-Morse Yukawa parameters. These parameters were $\kappa\sigma = 30.0$, $\beta\epsilon_Y = 1.0$,$\epsilon_M = 1.0$,$\rho_0 = 25.0$. These are the parameters we choose for our truncated-Morse Yukawa simulations.

$$U_{MY}(r) = \begin{cases} \beta\epsilon_M[1 + e^{\rho_0(1-r/\sigma)}(e^{\rho_0(1-r/\sigma)} - 2)] & r < \sigma \\ \beta\epsilon_y \frac{e^{-\kappa(r/\sigma-1)}}{r/\sigma} & \sigma < r \leqslant 2\sigma \\ 0 & r > 2\sigma \end{cases} \quad (4.1)$$

It can be seen from Fig. 4.12 that these parameters do not result in a substantial change to the fluctuations. There is maybe a very slight

shift away from the most high-density regions. This makes sense as the Yukawa potential will make it harder for the spheres to pack tightly.

4.5.6.2 Square Well

If the PSHA coating of our particles breaks down, the steric stabilisation which gives the hard sphere repulsion will begin to weaken. This may lead to attractions in the liquid which could disrupt the density fluctuations. We model these attractions with a square well potential, give by equation 4.2.

$$U_{sq}(r) = \begin{cases} \infty & ; \quad r < \sigma \\ -\beta\epsilon & ; \quad \sigma \leqslant r < \lambda\sigma \\ 0 & ; \quad r \geqslant \lambda\sigma \end{cases} \tag{4.2}$$

λ controls the length scale of the interaction, whilst ϵ controls the strength. Shown in Fig. 4.13 is the impact on the fluctuations caused by a square well potential. For a short range, shallow attraction ($\epsilon = 10k_BT$, $\lambda = 1.1$) very little difference is made to the fluctuations ($\sigma_{HS} = 0.011$, $\sigma_{SqWell} = 0.012$). Increasing the potential range and strength begins to broaden the distribution, as clusters begin to form, but again this is not enough to explain the experimental fluctuations. A very deep well $\epsilon = 10k_BT$ gives a much broader distribution $\sigma_{SqWell} = 0.019$, which is close to the experimental observation. However, at this point the liquid structure has changed substantially, with particles forming tightly-bound clusters. This can be seen clearly in the radial distribution function at this potential strength. Furthermore, a strength of $10k_BT$ would be very high. Even in systems which have an additional induced depletion attraction in order to cause gelation, $5k_BT$ would be a normal value of the interaction strength[191]. Our system should only have Wan Der Walls attractions, and the strength of these should be greatly reduced by the refractive index matching between the solvent and the colloids.

4.5.7 Volume Fraction

A further test is to check whether the density fluctuation change is volume fraction dependent. This may shed some light as to the mechanism of the fluctuations. We therefore run several samples at a variety of different volume fractions, and measured the relative size of the fluctuations with respect to the volume fraction. The results of this analysis are shown in Figure 4.14. Similarly, we run simulations to match the experiments and measure their fluctuations with respect

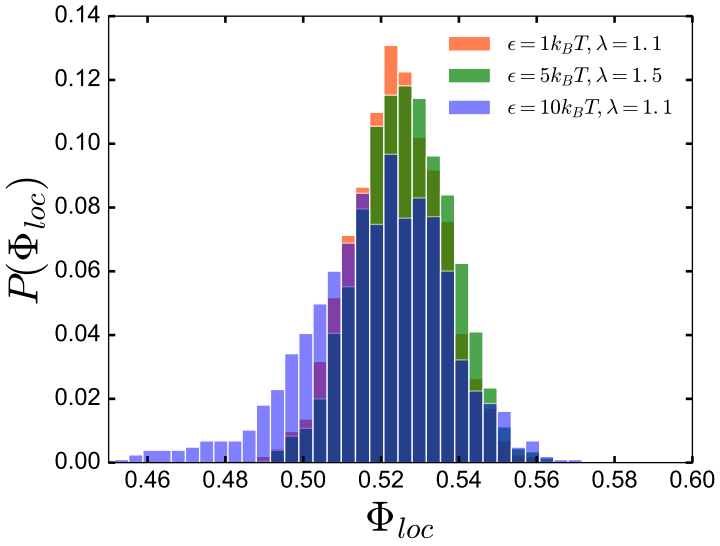

Figure 4.13: The effect of implementing a square well potential on the density fluctuations in our system.

to the volume fraction. We find that the simulations make a smooth decline in the fluctuation size when measured in this way, falling from about 7% at a volume fraction of 0.21 to about 2% at a volume fraction of 0.52. Meanwhile, the experiments show non-monotonic behaviour, declining between a volume fraction of 0.21 and 0.37, before increasing again at a volume fraction of 0.42. Whilst the experimental fluctuations agree very well with the simulations at a volume fraction of 0.21, the discrepancy begins to emerge at higher density, with the gap already existing at a volume fraction of 0.37. The gap then increases at a volume fraction of 0.42, and then remains constant at around 2% of the volume fraction for higher densities.

This result demonstrates that the fluctuation discrepancy only exists at relatively high volume fraction. It isit is possible that experimental inaccuracies may slowly emerge as the density increases. For example, it is plausible that the slight softness in the potential may only become important at high density, when particles regularly come into very close contact with each other. However, the previous work in this section has demonstrated that these inaccuracies struggle to explain the full extent of the fluctuation error. Another possibility is that at higher volume fraction, accurate particle tracking becomes more difficult. Particles have a Gaussian distribution in intensities when imaged by confocal microscopy, and at high packing fractions these distributions tend to overlap more and more. We therefore turn to examining the influence of tacking errors on the fluctuations.

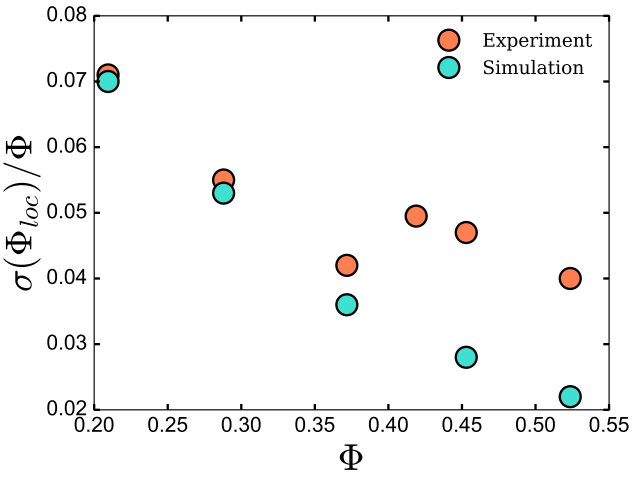

Figure 4.14: The size of density fluctuations measured with respect to the bulk volume fraction for a variety of densities. Shown in orange are experimental results, whilst in turquoise are simulation results.

4.5.8 Tracking Code

The tracking code used throughout this work is based on the multiscale colloidal tracking algorithm[150]. However, the first tracking algorithm for images of this type was developed by Crocker and Grier[148]. Rather than using a difference of Gaussian-convolved images, Crocker and Grier's algorithm found local maxima within the image after a single Gaussian blur (see Section 2.8 for more details). It is possible that the multiscale algorithm itself is causing our increased density fluctuations, and so we also run Crocker and Grier's tracking algorithm. The implementation used is the Python package TrackPy[192]. The result is shown in Fig. 4.15. We find that density fluctuations in Crocker-Grier tracked configurations are actually broader than in multiscale tracking, and we also are unable to locate all of the particles, leading to a slightly reduced volume fraction.

4.5.9 Tracking Errors

Particle tracking algorithms are used to move from our confocal image stacks to our final configurations. The particle tracking has an associated error in the output particle positions, and this error gets worse as particles become closer together (that is, as the volume fraction increases). For spheres at contact *with perfect images* this error is at 2.5% of the particle radius[150]. There is a further error associated with noise in the imaging[148], as well as for an elongated point spread function

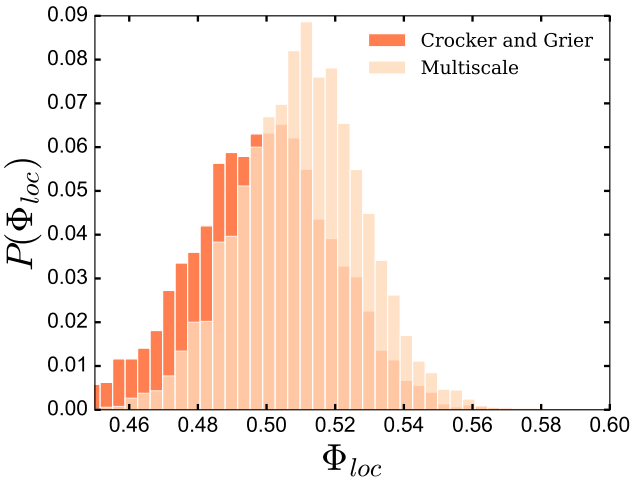

Figure 4.15: Distribution of local densities for the same configuration ($\Phi = 0.51$), for two different tracking methods. Crocker and Grier's algorithm (red) shows a larger spread of local volume fractions than the multiscale algorithm, and a mean volume fraction around 1% smaller owing to missed particles.

in the z dimension[150] as with our confocal imaging. Furthermore, the particle tracking can occasionally miss particles, or remove valid particles when filtering out spurious overlapped particles[150].

We model these errors by both randomly removing a small percentage of particles and slightly randomly displacing particles in simulated systems. The displacement is chosen by choosing a random unit vector in 3d space which determines the direction, and this is multiplied by a sample from a Gaussian distribution centred on a chosen mean. This chosen mean is generally a small fraction of the particle radius, and controls the average tracking distance error. By modifying the displacement error and the number of particles deleted we can explore the effect of the tracking errors on the density fluctuations.

In order to understand the number of particles that should be removed, we examine the positions identified by the tracking algorithm from experimental data. If particles which exist are being completely missed, then we expect to see voids in the configurations near the size of a particle. We choose a random point within the experimental box, and calculate how far away the nearest particle is. If the nearest particle is more than one particle diameter away, then there is a void of the size of a particle, which is indicative of a tracking error. In order to ensure that this void isn't found again, we place a new particle at the point with the void.

Taking many millions of random points and testing in this way, the measured number of voids of this size approaches the true number.

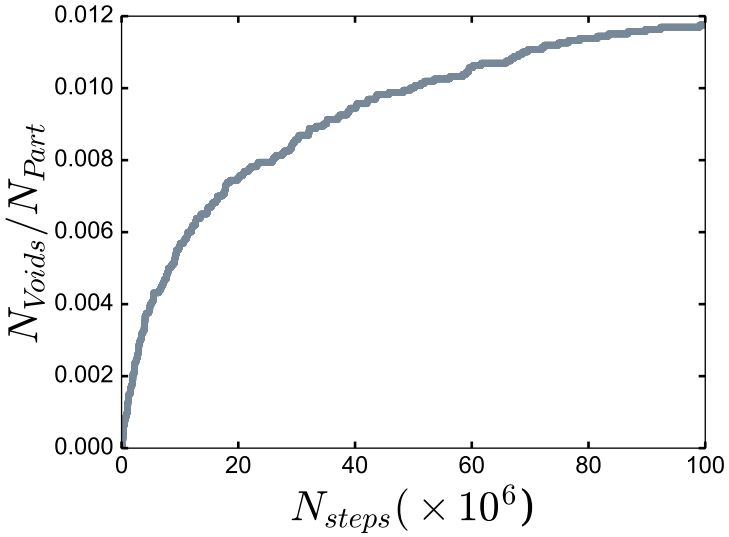

Figure 4.16: Number of particles added to the configuration when voids are located, as a percentage of the total number of particles in the configuration. The growth has not quite stopped, but finding many more voids will take orders of magnitude more computing time. This analysis was performed for a configuration with $\Phi = 0.52$.

That a void of this size exists suggests a missing particle is a good assumption at high volume fraction, when there are very few large natural voids in the liquid, but is a poor assumption at lower volume fractions. The fluctuation discrepancy emerges at high packing fraction, so in the regime that we are interested this should be a good assumption, even although it will only give us an upper bound on the number of missing particles.

The results of this analysis are shown in Figure 4.16. The number of voids located climbs rapidly at first, and becomes increasingly shallow as the remaining voids become difficult to find. When terminated, the number of voids located is still climbing incredibly slowly, and so we can only give a sensible lower bound on the number. It seems likely from Figure 4.16 that the number of voids found is unlikely to exceed 1.3% of particles in the system, and certainly not 1.4%, even if we give the simulation 3 orders of magnitude more computing time.

This allows us to approximate the effect of tracking errors. We randomly choose to delete 1.3% of particles from simulations, and move the remaining particles by a small amount. The configurations chosen are drawn from Molecular Dynamics DynamO simulations which have been compressed to $\Phi = 0.52$ and relaxed to equilibrium. We choose 20 configurations, each ten million time steps apart to

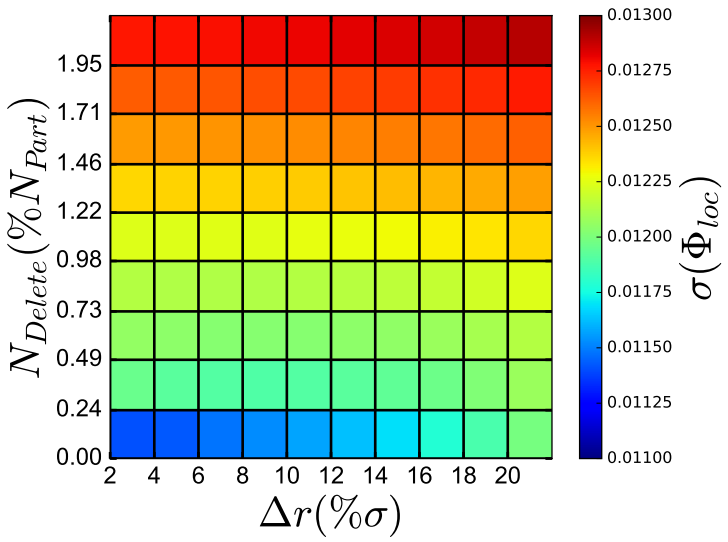

Figure 4.17: The size of the fluctuations on simulating standard particle tracking errors. This are small random displacements of each particle position (x axis), expressed as a percentage of the particle diameter, and the code occasionally missing particle (y axis), expressed as a percentage of the total number of particles. The colour shows the size of the density fluctuations, and it is clear that a difference is made, although the extent is too small to explain the simulation-experiment discrepancy (note the small range of the colourbar).

ensure they are independent from each other. All results quoted here are averages from those 20 configurations, meaning they each include around 40000 particles. For more details on the simulations, see section 4.3.

Figure 4.17 shows the effect of various choices of particle deletions and movements (to model positioning errors) on the density fluctuations. It can be seen that whilst both deletions and small movements tend to increase the density fluctuations, the extent is relatively minor. Certainly no reasonable choices of the number of particles to delete or the extent of the displacement result in fluctuations close to those found in experiment.

However, it should be noted that this analysis assumes that the error on the tracking positions is random. That is, the error on a particle is independent of the local environment of that particle. This is a reasonable first order assumption. However, the particle tracking errors may not be independent of the environment - for example if particles which are very close to each other are systematically pushed further apart[193]. This could create pockets of high or low density which our fluctuation analysis is seeing.

4.5.10 2d Tracking

The preceding series of experiments and tests cover every plausible parameter, in experiment or simulation, that could explain the measured density fluctuation difference. As such, we attempt to find a test in which we **can** match the density fluctuations. For example, we can test the fluctuations in just two dimensions. This provides a split between the experimental system itself and the particle tracking errors related to the point spread function in z. If the tracking is accurately measuring the structure of the colloidal liquid, which is different from that of the simulation liquid, then that divergence should still be seen when the analysis is restricted to just the xy plane.

However, clearly we have a three dimensional experimental system, which cannot easily be constrained to two dimensions without adding many other confounding factors. For example, using a highly density-mismatched system would cause the particles to sediment to the wall of the capillaries, and in this manner we could image them in two dimensions. However, this adds new issues like a substantial refractive-index mismatch between the solvent and the colloids and interactions between the wall and the colloids themselves. We therefore retain the images taken in three dimensions, but simply constrain our analysis to two dimensions. This means taking single xy slices from our experimental stacks, and tracking the particles in them with no reference to the third dimension.

We can calculate fluctuations in 2d in a very similar way to our 3d algorithm, simply removing the z dimension and calculating distances in xy only. When comparing to simulations care must be taken, however. Just taking a single slice from an experimental image stack clearly does not constrain the experiment to 2 dimensions - the slice will contain particles centred on a variety of different z planes. Any particles which have centres less than a radius from the z slice will appear in the image, and will appear smaller the further away they are. Clearly, taking a simulation configuration, choosing a z value, and only considering particles at exactly this value does not recreate this situation (in fact, almost no particles will survive this filter). Instead, a z value is chosen, and particles which have a z-position within a radius of this value are considered. This then replicates the experimental constraint.

The result of this quasi-2d analysis is shown in Fig. 4.18. The fluctuations of the experiments and the simulations agree very well in the xy plane. However, when we take slices of the experimental images in the XZ plane, we see a much broader distribution of the local densities.

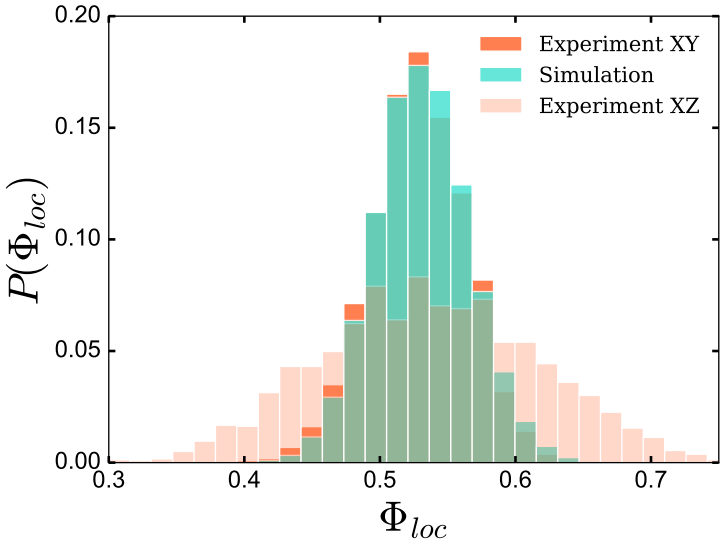

Figure 4.18: The distributions of local densities when analysis is restricted to two dimensions. Two dimensional experiments agree very well with simulations when the analysis is restricted to the XZ plane. However, when images are analysed in XZ, a plane in which the imaging is substantially inferior, the distribution broadens significantly.

The implication is that the discrepancy is not due to a fault with the experiments themselves, as this should be as clear in the xy plane as in the full 3 dimensional images. Similarly, two dimensional tracking in just the xy plane is quite accurate. However, relatively poor imaging in z results in the tracking failing to recreate the fluctuations in three dimensions accurately. This explains the observation that at low volume fraction the simulations and experiments agree. With a larger average distance between particles there will be less overlap, and so the particles can easily be located accurately.

The further implication of this result is that these density fluctuations are unlikely to be the cause of the nucleation rate discrepancy. The nucleation rate discrepancy lies either with an error in the experiments themselves (they do not recreate the theoretical hard sphere rates), the interpretation of scattering data, or the simulations. The density fluctuations are a result of particle resolved **analysis**, rather than any of these three issues.

However, particle resolved studies can accurately reproduce the theoretical radial distribution function, and even the qualitative behaviour of a wide variety of local structures with increasing volume fraction. It is somewhat surprising then that the co-ordinates from tracking are not good enough to reproduce

4.6 MODELLING FLUCTUATIONS

It has been shown that the density fluctuation increase occurs due to the particle tracking method. The fact that tracking in the quasi 2 dimensional xy plane works well suggests that the poor resolution in the z-dimension is the cause. However, we have not yet proven that the tracking itself is the issue, nor have we elucidated clearly what causes the tracking to fail. In order to move further, we examine the performance of the tracking code closely.

4.6.1 Two Particle System

The first test to check for errors in the particle tracking is to simulate the most basic case - two particles which can be moved relative to each other. In order to do this, we simulate images which mimic experimental images by defining a Gaussian intensity distribution for each particle. The tracked co-ordinates from this image can then be compared to the input positions of the mean of the Gaussian distribution, any errors in the tracking appear as differences between these values. The extended point spread function in z can be modelled by increasing the variance of the distribution in the z direction, creating a larger overlap between the particles in this direction.

4.6.1.1 Modelling Images

In order to accurately model our images, we fit our 3d Gaussian to the intensity profiles of individual particles cropped from microscope images. These images are taken at low volume fraction ($\Phi = 0.21$), to ensure that the particles are isolated so that only a single particle contributes to each measured intensity distribution. Matching the average of ten such distributions gives us confidence that our modelling reproduces the microscope images accurately.

4.6.1.2 Modelling Noise

Simply finding particles modelled with well defined Gaussians will be an easier task for the particle tracking than tracking the true experimental images. This is because the true images also have some degree of noise. This noise will come from multiple scattering events from the colloidal particles, dye which may leech into the solvent, and optical imperfections in the microscope and sample cell. To model the noise, we add or subtract a random amount from each pixel intensity. Each random number is sampled from a normal distribution with known

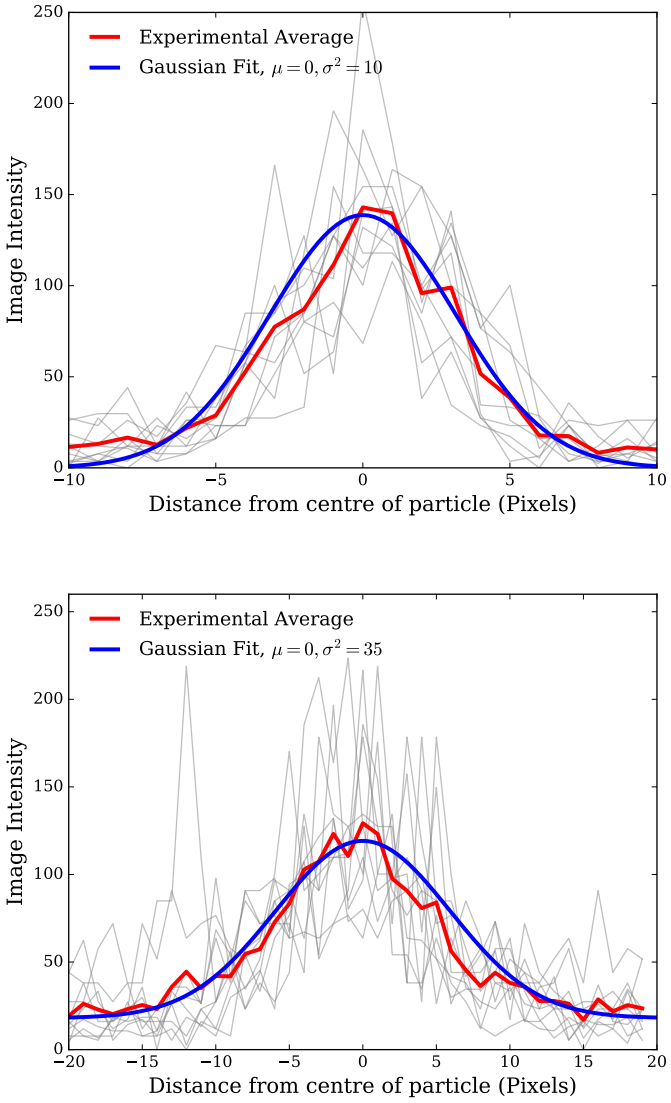

Figure 4.19: Modelling the size of a particle in our experimental system at a low volume fraction. **Above.** Shown in red is the average of ten particle intensity distributions in the x dimension, and in blue is a Gaussian fit to this distribution. Shown in light grey are 10 of the raw particle intensity distributions to show the noise in this analysis, which is quite high. **Below.** The same analysis, but for particles projected in the z dimension. It can be seen clearly that the z imaging is substantially worse than the imaging in x and y, and the particles are blurred in z (note the wider x axis in this graph).

mean and variance. It is difficult to measure the amount of noise present in the experimental images, as we have no access to a noiseless image with which to compare. Instead, we increase the extent of the noise until the simulation images closely match the experimental images.

4.6.1.3 Monitoring Tracking

Using the above profiles of the particles in x, y and z, we can create test "experimental" images in which we control the position of the simulated colloidal particles. This can be done by using a Gaussian distribution quantised on a meshgrid of a size similar to that of our experimental images. We can tune the degree of blurring of the three dimensions independently by changing the standard deviations of the Gaussian distributions which generate the image. In fact there is only a need for two parameters, one which controls the standard deviation in x and y and another which controls the standard deviation in z, this is due to the fact that the point spread function of the microscope is symmetric in x and y but extended in z. By centring the Gaussian distributions at known positions and comparing the results of the tracking, we can study errors in the tracking algorithm. We try to model the images to replicate the experimental images as closely as possible. That is, the particles themselves are around 10 pixels across, with a similar intensity distribution between 0 and 150, as in the average distributions shown in Fig. 4.19.

In order to model the tracking errors, we leave one particle fixed, whilst moving a second particle nearby. We choose three angles, $\theta = 0$ with respect to the axial dimension - particles aligned along z, $\theta = \frac{\pi}{2}$, particles aligned along x, and $\theta = \frac{\pi}{4}$, particles aligned diagonally between the two dimensions. We then bring the free particle closer to the stationary particle, from a maximum centre-centre distance of 2σ to a minimum of 1σ (the minimum distance with a theoretical hard sphere potential). The result of this analysis is shown in Fig. 4.20.

We find the tracking behaves in a complicated manner. When particles are side by side, with the same z position, there is little overlap of the two distributions and the code performs very well. This replicates the 2 dimensional tracking result, in which tracking images just in x and y performed well against simulation fluctuations. However, when particles have some overlap in z, the tracking performs more poorly. If the two particles are very close, they can be registered as just a single particle which is positioned between the two true positions. However, if particles are slightly further away, they tend to be pushed closer together than they truly are.

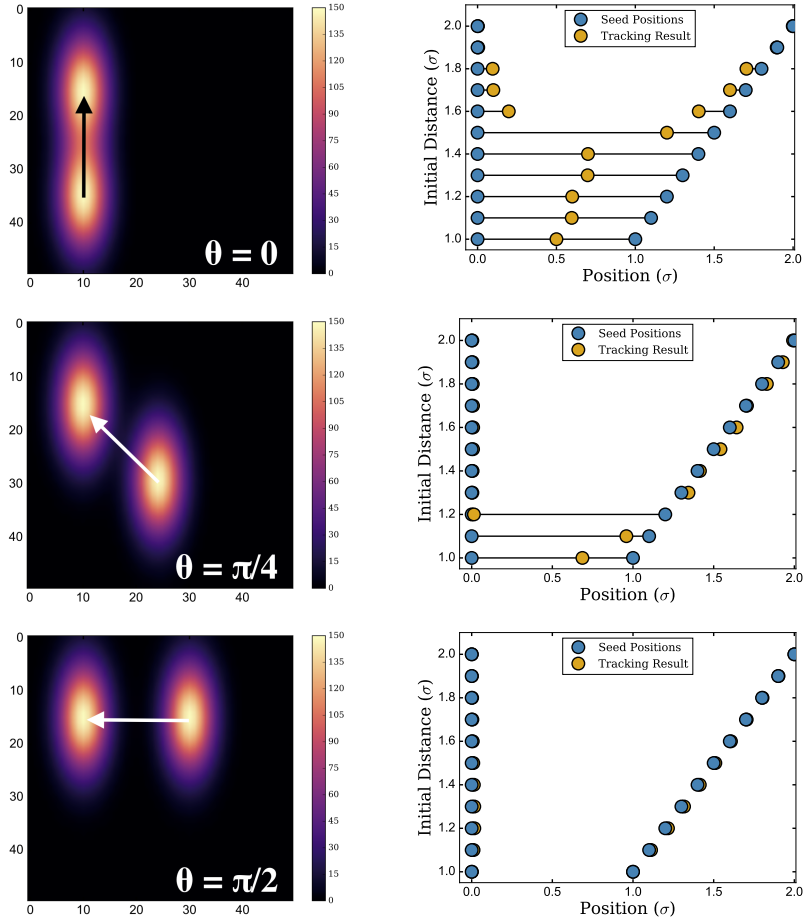

Figure 4.20: The characterised results of our tracking code with realistic particle images. On the left are the input images for three different angles, $\theta = 0, \theta = \pi/4, \theta = \pi/2$. These images are shown at the maximum distance between the particles, 2σ. On the right is shown the results of the tracking as the test particle is brought closer to the stationary particle, always along the vector connecting the centres of the two particles. Distances are along this vector, with zero corresponding to the centre of the stationary particle. In blue are the true seeded positions, whilst in yellow are the results given by the particle tracking. When there is only a single yellow particle, the tracking has only found a single particle.

This mechanism is the first possible explanation for the anomalous fluctuations which could explain the *widening* of the local density distribution. What is arguably most surprising about the result discussed is not just that experiments disagree with simulations, or that this is due to an artefact of the tracking, It is that the experimental fluctuations don't look like an artefact. If the tracking just had a tendency to delete particles, for example, this would manifest in too many regions with low local volume fractions. Other effects, like slight particle attractions, would be likely to create regions of higher density. The fact that the tracking can both delete particles, creating low density regions, *and* act as an effective attraction between particles means that it can potentially explain the fact that high and low density regions exist.

4.6.2 Resolving Particle Merging

What the above shows is that our analysis in section 4.5.9 was not subtle enough. There we assumed that particles would be completely missed by the tracking, leaving voids of a volume of roughly one particle, and attempted to find signatures of this effect. In fact, it seems more likely that particles will be merged than completely missed. This merging will happen preferentially in the z direction, as this is the dimension along which the particles are extended.

We can therefore look for signatures of this process in our tracked configurations. This involves checking for voids that exist both above and below individual particles in the z dimension. Our algorithm to do this moves through every particle in our configurations, and checks to see if there are no particles both above and below, which we refer to as z-neighbours. This involves two cutoffs, the first filters out all particles which might be z-neighbours according to their z position. Particles are z-neighbours if their centre is closer than 1.5σ from the test particle. The extra radius is to account for the fact that when we insert two new particles, their centres are placed one radius above and below the test particle's centre. The second cutoff then selects from the list of potential z-neighbours those which are close enough in xy to be true z-neighbours. In order for their to be a void above or below the test particle that could have accommodated a merged particle, there needs to be no particle within 1σ in xy of our test particle. Once both filters have been applied, we know if there are any particles which are both within 1.5σ in Z and 1σ in xy. If there is at least one particle like this, then there is not space in the new configuration for a particle merging event. However, if there are no z-neighbours, then a merging

event may have occurred. In order to check the upper bound of this effect, for every particle found which has no z-neighbours, we split the particle into two new particles at a distance 1σ from each other in Z.

When we run this algorithm over a typical high volume fraction configuration ($\Phi = 0.52$), we find that there are particles which lack z-neighbours. However, there are only a very small number of these particles, and so the splitting process makes very little difference to the density fluctuations in the whole configuration. For the parameters for the cutoffs described above, there are generally fewer than five particles which lack z-neighbours. However, we can relax our criteria slightly, to account for the packing of spheres. The argument above with respect to the xy cutoffs implicitly assumed that our particles are cubic. In fact, a particle centred at 1.4σ above another and 0.9σ away in xy is not a z-neighbour in the relevant sense, as it will not block the entry of the upper split particle. As such, we can relax the xy cutoff slightly, to 0.9σ, to account for the particle sphericity (in fact this will then underestimate the number of z-neighbours). This does increase the number of particles found without z-neighbours, up to around 75 (still less then 0.5% of the total number of particles in the configurations), and this decreases the fluctuation size from 0.0205 to 0.0203.

This effect does not appear large enough to explain the large experimental fluctuations. However, there's some possibility that the above analysis does not fully capture the effect of the merging. For example, the fact that there is error on the particle positions may mean that some particles which should have no z-neighbours in fact are found with z-neighbours, with the voids being slightly crossed by other particles. It is possible to reduce the fluctuations further by tightening the conditions for z-neighbours to be found, moving down to a standard deviation of 0.018 for an xy cutoff of 0.9σ and Z cutoff of just 1σ. This results in very unphysical configurations, though, with substantial overlapping between particles and high values of the radial distribution function below $r = \sigma$.

4.6.3 Resolving Particle Errors

The errors which cause the fluctuations seem likely to come from two sources, particle merging creating low density regions, and particles being dragged closer to each other in z, creating high density regions. We've modelled the former effect, but could the latter effect also be modelled? For some time, an attempt was made to measure the

effective “field" which alters a particle’s true position to its measured position, given some set of surrounding particle co-ordinates. The hope was that this field could then be used to establish the “true” particle positions, given the measured positions. This, however, is a difficult inverse problem - even given the field and a set of measured co-ordinates, there are many different “true" positions which could be mapped. Our original proposed algorithm was to choose each particle, examine its surroundings, and then move the particle back to a position more indicative of its real position. This has a clear problem though, which is that moving a particle changes the surroundings of every nearby particle, and so the final “true” position will be highly dependent on the order with which we move the particles. We conclude that this is not a very promising avenue for establishing the real particle positions.

4.6.4 Creating Simulated Experimental Configurations

To explore the effect of the tracking errors further, we create model experimental configurations from known simulation configurations. To do this, we create images from the simulation configurations by centring a Gaussian intensity distribution at the location of each particle in the simulation configuration, in a similar way to section 4.6.1.3. However, this time we are interesting in exactly recreating the experimental situation, so we use a box size comparable to that of the experiments. The experiments contain very close to 8 times more particles as the simulations at the same volume fraction, and so using a 128x128x128 box size gives the same apparent particle density for the same Gaussian standard deviation (particle diameter). We can then increase the extent of the z-blurring by selectively increasing the standard deviation of the Gaussian in z, and monitor the effect on the measured configurations.

In fact, the methodology used in section 4.6.1.3 was found to not be sufficient to accurately reproduce the experimental images by eye effectively at high volume fraction. This is because images of our particles are not Gaussian distributions, but rather from spheres of uniform brightness convolved with a Gaussian distribution. As such, we create images using this process, and find that the experimental images are reproduced excellently (see Fig.4.21).

We can then control the extent of the blurring in the z direction and monitor the size of the distributions. We also find that the extent of the noise in the image is also an important variable. The effect of

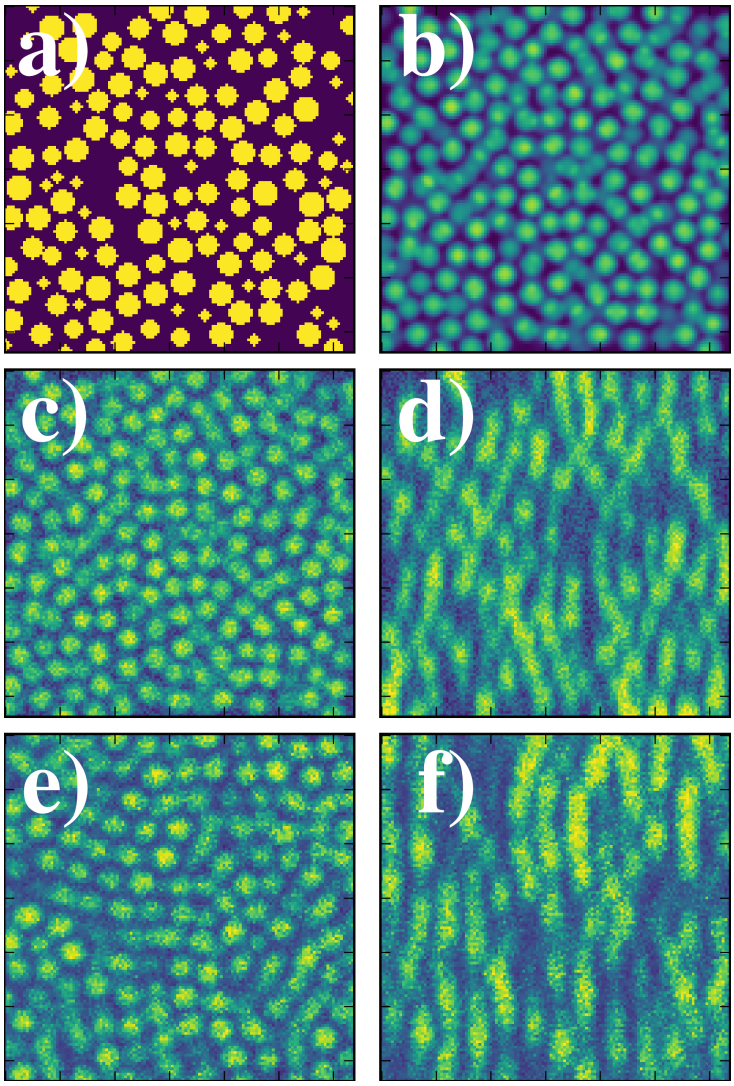

Figure 4.21: Generating experimental images from simulation configurations. **a)** An initial ideal image of colloids unaffected by the point spread function. **b)** The same configuration after convolution with a Gaussian distribution. **c)** Adding noise to approximate experiments. **d)** The same image shown in c), but sectioned through the yz plane, demonstrating the increased blurring in z. **e)** A sample experimental image in xy for comparison. **f)** A sample experimental image in yz for comparison.

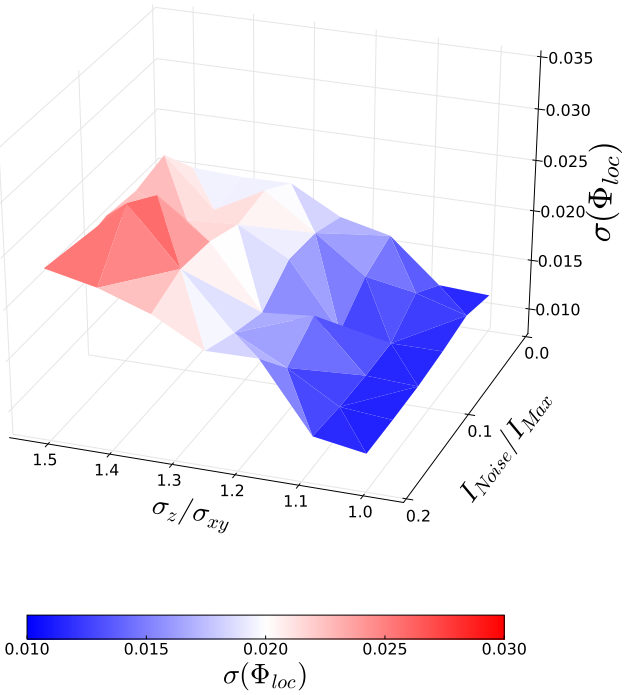

Figure 4.22: The behaviour of the density fluctuations when altering the noise level and degree of blurring in the z direction. Blurring is given as a ratio between the standard deviation of the Gaussian distribution in xy, and the standard deviation in z. Noise level is shown as a proportion of the maximum value of the image and the mean of the Gaussian distribution from which the noise is sampled (see section 4.6.1.2). Blue values correspond to parameter choices which do not fully resolve the discrepancy between simulation and experiment, whilst red values correspond to parameter choices which do fully explain the discrepancy.

changing the blurring in z and the extent of the noise on the density fluctuations is shown in Fig. 4.21.

From Fig. 4.22 we can clearly see that fairly normal imaging parameters are enough to induce density fluctuations of the necessary size. The image in Fig 4.21 c) used a noise level of around 0.2 (noise amplitude 50, maximum image intensity 256), whilst the blurring is relatively high, with $\sigma_z = 1.4\sigma_{xy}$. These two effects therefore are enough to fully explain the density fluctuation discrepancy between simulation and experiment.

4.7 RELAXING DENSITY FLUCTUATIONS

4.7.1 Motivation

The above work demonstrates that overly large density fluctuations are an artefact of real space confocal tracking techniques. However, previous work has demonstrated that the quantitative and qualitative behaviour of the local structure of tracked colloidal hard spheres match simulations to a high degree of accuracy[194]. Given that correctly identifying local structures relies on quite precise and accurate measurement of particle positions, it might be asked if we should be suspicious of the local structure results, given that pattern of density populations is hard to reproduce. To some extent we know that errors do play a role in the TCC analysis, which is why the f_c parameter is changed to compensate. One possible question would be whether the normal co-ordinate errors which reduce TCC populations also create these density fluctuation errors.

In order to answer this question, we use Monte-Carlo simulations to study the relaxation of our experimental configurations. As we run more Monte-Carlo sweeps, our experimental liquid will relax towards a “simulation" configuration, and in the limit of increasing numbers of Monte-Carlo steps, all of the properties of the liquid should match simulations, including the density fluctuations and the populations of locally favoured structures. If the same tracking errors that cause the fluctuation difference affect the populations of the local structures, we would expect to see both relax on the same timescale.

Despite being able to match the populations of locally-favoured structure to simulation configurations, we still expect the populations to change as we go through the relaxation. This is because the TCC analysis which locates the structures in the bond network is tuned using the f_c parameter to give matching populations at a given volume fraction. This accounts for errors in the particle tracking, and once this procedure is performed populations at all volume fractions match. However, once we relax an experimental configuration to a simulation configuration, the f_c parameter will be “too high” for the simulation, and we will therefore see an artificially large amount of local structure. This could potentially be accounted for by lowering the f_c parameter as we increase the number of Monte Carlo steps. However, this would require modelling the f_c parameter change, and it is unclear how this would be done. In the end, if this modelling were performed to keep the population of local structure constant then the rate of change of the f_c parameter would itself become the measurement of interest.

This is less transparent than simply looking at the timescale at which the population of local structure grows directly, and so this is our chosen measurement.

4.7.2 Method

Due to the fact that some particles slightly overlap in our initial configuration, we cannot use the hard sphere potential itself, as it will return infinite energies. Instead we choose a soft sphere potential given in equation 4.3, with $n = 20$.

$$\beta U(r) = (\frac{\sigma}{r})^n \tag{4.3}$$

Unlike a normal simulation we cannot use periodic boundary conditions as this would radically change the configuration, making particles on opposite sides of the box into neighbours when in the experiment they could have been up to 40σ away from each other. To stop the particles leaving the box we freeze the layer of particles closest to the walls - any particle within 1.5σ of a wall is frozen.

In order to relax the system, a standard Metropolis algorithm is used[195]. Firstly, a particle is chosen at random, and is displaced by a set amount in a random direction. The change in energy of the entire configuration is then calculated by finding the distances between the displaced particle and every other particle, and calculating the sum of the potential in equation 4.3 over all these new distances. Doing this once with the distances before the displacement and once with the distances after the displacement, and subtracting gives the change in energy. If this change in energy is negative then the displacement is automatically accepted, the particle is moved to its new position and a new sweep begins. If the change is larger than zero the Boltzmann probability of the change is calculated as $\beta e^{-(\epsilon_0 - \epsilon_1)}$. This probability is then compared to a random number between 0 and 1, if it is larger than this number then the displacement is accepted, if it is smaller then the displacement is rejected and the configuration returns to its previous state.

4.7.3 Results

Shown in Fig. 4.23 is the change in the density fluctuation standard deviation when we relax our experimental configurations. We see an initial rapid decline followed by a plateau, as would be expected. However, this plateau value does not appear to drop to the pure simulation result for monodisperse hard spheres, instead it seems to

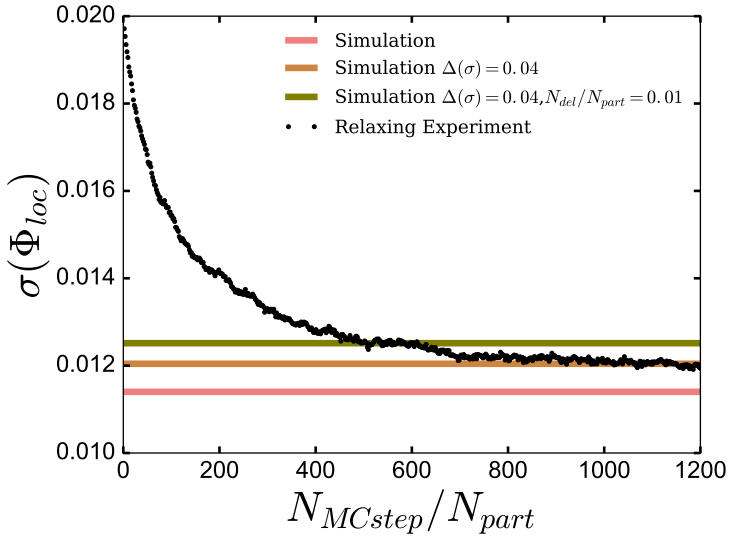

Figure 4.23: The decline of the density fluctuations as an experimental configuration is relaxed with Monte Carlo steps. Three comparison values are given, an ideal, monodisperse simulation (pink), a simulation with 4% polydispersity (orange) and a simulation with 4% polydispersity and 1% of particles deleted at random (green). The experimental fluctuations decrease as expected with increasing numbers of Monte Carlo steps.

correspond to the value for a system with some polydispersity. This is very surprising, as all our particles have the same enforced potential, the system is essentially being forced to become a monodisperse hard sphere system.

When we explore this further, we see that this is due to the frozen particles at the walls "locking in" some of the larger density fluctuations, whilst particles which are close to the centre of the configuration relax to the monodisperse hard sphere value. Shown in Figure 4.24 (above) is the same analysis, but each line now corresponds to a different subset of the particles. The first step are those 1000 particles which are closest to the walls, each further dataset moves deeper into the system, and it can be seen that the most internal particles relax to the monodisperse level, as expected.

During this relaxation, we also expect the populations of local structure to be relaxing to their simulation values. As we study the defective icosahedra (10B) populations previously in this work, this is the structure we focus on here. Shown in Fig. 4.24 (below) is the population of the defective icosahedra throughout the relaxation, split by groups of internal particles, as previously. We indeed see the relaxation of the value up to the simulation value. There appears to be a similar trend to the density fluctuations, with the populations tending to higher

values with as the distance from the walls increases. However, this is less pronounced the trend for the fluctuations. To some extent this is expected, as the length scale of a defective icosahedra cluster is considerably smaller than that of our density fluctuations, therefore any residual effect from the walls should decay away more quickly than for the fluctuations.

Figure 4.25 shows both the population of the defective icosahedra and the standard deviation of the density fluctuations as the system is relaxed in simulation. For consistency, only the results from the interior 1000 particles are shown - therefore choosing a point along the x axis gives the results of density fluctuations and defective icosahedra population for precisely the same set of particles. The defective icosahedra populations could be taken across the entire region, but as there is no trend in the defective icosahedra with respect to distance from the walls, this would make little difference to the result. We see that for small numbers of Monte Carlo steps (fewer than around 200 per particle), the density fluctuations make a rapid decline, whilst the defective icosahedra populations hardly change from their initial value. This demonstrates that there is a separation between the errors that result in the defective icosahedra populations being generally too low from those which generate the density fluctuation error.

Given the low number of Monte Carlo sweeps required to substantially reduce the density fluctuation artefact, it may be possible to add this procedure into our tracking methodology. That is, if we can arrive at more accurate configurations of particles, in the sense that they are less affected by fluctuation error, whilst still remaining very close to the original configuration, this might be thought of as simply a new processing step. However, for this to be a valid processing step, we cannot end up with a configuration a long way from the original output of the particle tracking, or this will be closer to a new simulation configuration, rather than the "real" experimental configuration of interest. To quantify this, we check the distance that particles move from their staring points throughout the Monte Carlo relaxation. The results of this are shown in Fig 4.26. Unfortunately, by the time the density fluctuations have relaxed, after around 200 Monte Carlo steps per particle, more than 50% of particles have moved more than $\frac{1}{3}\sigma$ from their starting positions. This limits the potential for a small Monte Carlo relaxation to be integrated into a tracking methodology.

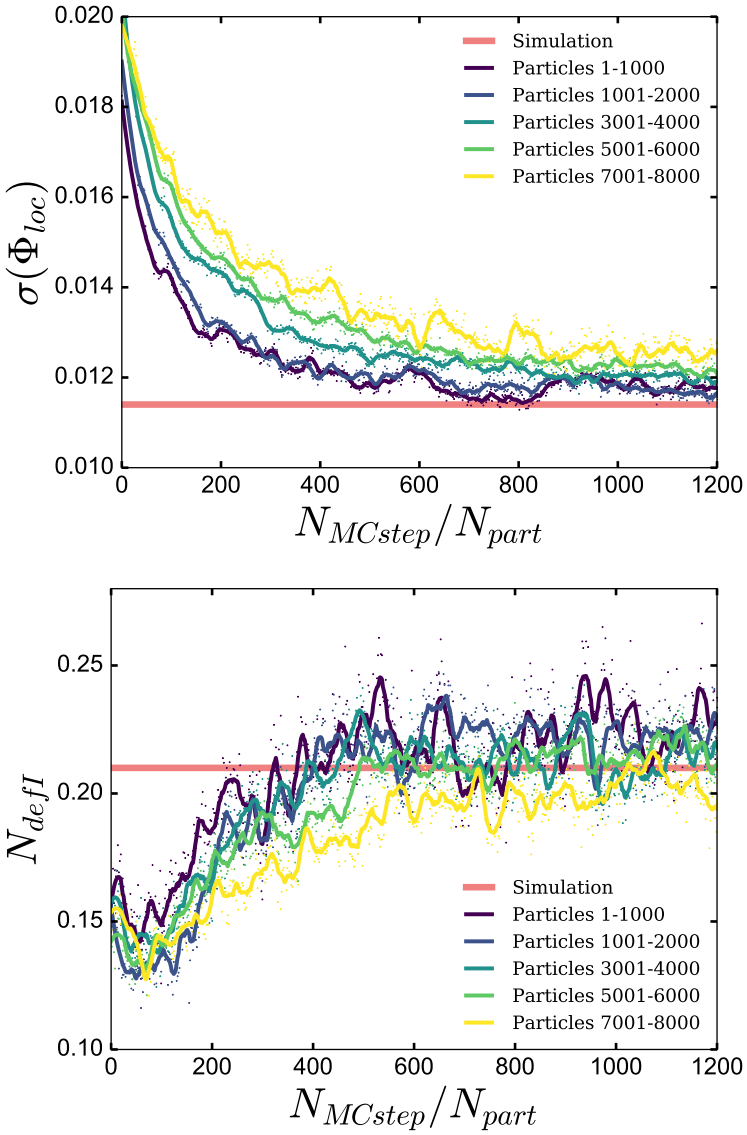

Figure 4.24: **Above.** The decrease of the density fluctuations as an experimental configuration is relaxed with increasing Monte Carlo steps. **Below.** The increase of the defective icosahedra population as an experimental configuration is relaxed with increasing Monte Carlo steps. All experimental data is divided into distances from the edge of the frozen containing walls. Particles 1-1000 are the most internal 1000 particles, particles 1001-2000 are the one thousand and first to the two thousandth most internal particles, and so on.

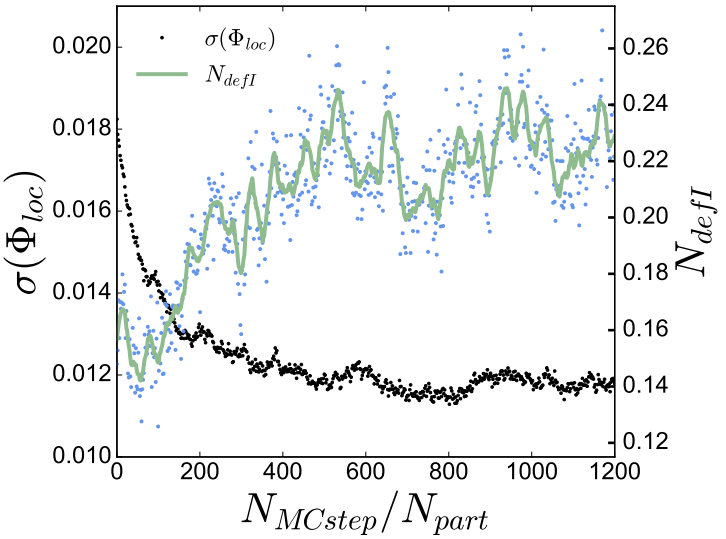

Figure 4.25: The trend in the defective icosahedron population and the density fluctuations with increasing number of Monte Carlo steps. Data shown here is for only the most internal 1000 particles, to avoid the residual effects from the frozen walls.

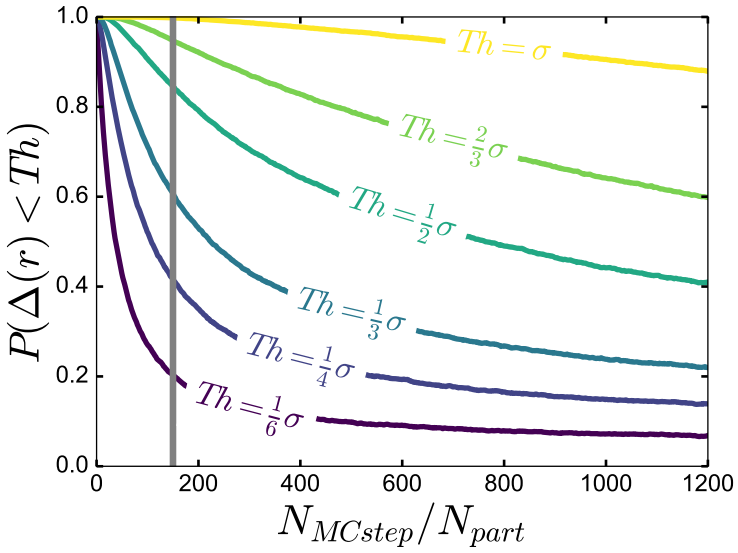

Figure 4.26: The extent to which particles have moved from their initial positions with increasing numbers of Monte Carlo steps.

4.8 CONCLUSION

Initially when this work was begun, it was to serve as a follow up to the work in Chapter 3, to check another possible parameter which could be coupling with sedimentation. Instead we found an important limitation of real-space confocal microscopy techniques, which give experimental density fluctuations that are much larger than those seen in simulation. This is due to a systematic error in particle tracking combined with poor z-resolution. However, we show a decoupling of the density fluctuation error and the topological cluster classification results, suggesting that whilst the tracking is too error prone to study density fluctuations at these volume fractions, it is good enough to accurately reproduce bulk cluster populations. This raises the question of the limitations of real-space confocal studies. At the very least, results need to be checked carefully against simulation work and discrepancies carefully investigated.

This work also sheds new light on the nucleation barrier results of Ketzetzi *et al.* (2018)[132]. Instead of their barriers collapsing due to the insensitivity of nucleation to density fluctuations, it may be that they collapse because the measured density fluctuations themselves are incorrect. If tracking errors are causing a very large error on the measured local densities, this will tend to compress the nucleation curves.

5

MEASURING NUCLEATION RATE DENSITIES IN CONFOCAL MICROSCOPY

5.1 INTRODUCTION

Confocal microscopy allows for particle-resolved imaging techniques to probe processes like nucleation. However, no systematic measurements of the nucleation rate have been taken using confocal microscopy. Some work has measured nucleation rate densities, such as Gasser *et al.* (2001)[32]. This work is limited in scope, however, quoting only high upper bounds for J across a range of high and low volume fractions. In the crucial coexistence intermediary region, where the discrepancy exists, only a general statement of the order of magnitude is given. Whilst these results were within the range of the literature scattering results, they are not precise enough to constitute an independent test of the scattering work. Ketzetzi *et al.* (2018)[132] also quote nucleation rate densities, but as previously discussed, these are likely dominated by the sedimentation profile.

A key issue with confocal measurements is that they are limited by the size of the particles they can study. In order to resolve the particles to the precision required for particle tracking, they generally need to be quite large. The resolution of particle tracking using confocal microscope images is around 50nm[161,196], meaning particles need to be at least 1μm, and preferably as large as 2μm[161]. For example, the Gasser *et al.* (2001) particles had a radius of 1.26μm, whilst the Ketzetzi *et al.* (2018) used particles with a radius of 0.97μm. Larger particles will tend to move more slowly, and therefore take longer to nucleate than the smaller particles used in scattering. The scattering work uses particles just under half the size of the confocal work, and the relaxation time scales with r^3. There will therefore be about an order of magnitude longer to wait for the confocal experiments to nucleate, experiments that took a few hours to nucleate will now take on the order of days. Worse, the scattering experiments have access to a macroscopically large volume, whilst the confocal experiments generally only consider volumes a few dozens of particles across at most. Gasser *et al.* (2001) measure a box that is 58μm by 55μm by 20μm, which has a volume roughly ten million times smaller than Sinn *et al.*'s (2001)[91] 20mm by 10mm by 5mm imaging box. This means

that we expect a nucleus to take ten million times longer to emerge in the confocal work than in the scattering work, which quickly pushes accurate measurements in the weakly supercooled regime out of reach.

It's unclear exactly how the Gasser (2001)[32] work, for example, calculated nucleation rate densities, but it was likely by measuring the time it took for the system to crystallise, and dividing by this time multiplied by the volume. This has three major drawbacks. Firstly if multiple nuclei form at once, or if one forms whilst another is growing, this measurement will systematically underestimate the the nucleation rate density. Secondly, only one event is seen per sample. As nucleation is inherently a random process, this means that many different runs need to be taken and averaged to find an accurate nucleation rate density[197]. Finally, there is some ambiguity as to the correct volume to consider. For example, the Gasser work observed a volume of 58μm by 55μm by 29μm, a volume of 6.38×10^{-11} litres, whilst the total volume of the sample was 50μL, almost a million times larger. Therefore, the chance of any given nucleation event occurring within the imaged volume is incredibly tiny, and any observed crystallisation is likely to have begun occurred outside of the imaging box. This means that the size of the imaging box itself is not the appropriate volume. The size of the entire sample could be chosen, but it is not clear that this is correct either. There is an excluded volume caused by the sintering itself, and a zone near to the walls where nuclei will be suppressed, both of which reduce the true volume. Furthermore, if we are trying to measure rates in the coexistence regime (where the nucleation rate discrepancy emerges), very often our imaged sample simply won't crystallise, whilst the nucleation event takes place elsewhere in the sample. If we claim that our imaging volume is representative of the whole sample by taking the volume measured to be the entire sample, we will understate the true nucleation rate density. It's possible that enough samples will ameliorate this issue, but it make an already formidable data collection challenge substantially more difficult.

A further issue is present, which is that of measuring the volume fraction accurately. In 2 the systematic and random errors on an accurate measurement of the volume fraction are discussed. These mostly relate to errors in the sample preparation, but it is also difficult to extract accurate volume fractions from post processing of the images. Methods like matching the radial distribution function can get close, and confirm the prepared volume fraction to within a few percent, but a few percent in the volume fraction can make the difference between excellent agreement with simulations and staggeringly poor agreement. This issue can be clearly seen in the Gasser (2001) work,

which only quotes volume fractions in a vague way, referring to the important low Φ regime as simply "$0.45 < \Phi < 0.53$". Furthermore, the Gasser work quotes nucleation rates below $\Phi = 0.45$, suggesting that their volume fractions are not calibrated to coincide with the phase diagram of hard spheres.

We therefore develop a new technique for performing real-space confocal microscopy. This is motivated by the need to increase the proportion of the system sampled, whilst also increasing the speed of nucleation by using smaller particles. We also develop a new and more accurate method for measuring volume fractions in real space, influenced by the original scattering work.

5.1.1 A Hybrid Reciprocal-Real Space Technique

Given the difficulties listed above, it seems clear that confocal measurement of rare events like nucleation will be difficult when those events become truly unlikely. This is the case due to large particles and relatively small measurement volumes. However, these limitations only exist due to the attachment to particle-resolved experiments. Particle resolved experiments are a key strength of confocal microscopy, as they allow extremely precise measurement of things like the structure of crystal nuclei[32] or kinetic pathways during crystallisation[38]. However, we need not necessarily perform *particle tracking* to measure real space quantities and effects. For example, measuring nucleation rates may only require some ability to check if a particular region is crystalline or not. Abandoning particle tracking allows us to make our particles smaller, both physically and in terms of their size in our images. Using smaller particles speeds up the nucleation process, whilst using a larger imaging volume speeds up our experiments. In this chapter a technique to study crystallisation in this way is developed.

The typical method for measuring nucleation rate densities with confocal microscopy is described above, simply measuring the crystallisation time and dividing by the volume of the containing box. This process has some degree of error associated with it, as discussed previously. Another issue is that at the low volume fractions where the discrepancy exists, it is very difficult to observe a full nucleation event, as this can take months to years even for reasonably small particle systems. However, a different property can instead be measured, and indeed is what is measured with biased Monte Carlo methods - the nucleation barrier itself. From the nucleation barrier, the nucleation rate density can be determined if the kinetic prefactor is also measured. A positive aspect of measuring the nucleation barrier is that

we can image small, pre-critical nuclei which exist throughout the supercooled liquid and use the populations of these nuclei to measure the barrier at small nucleus sizes. This then can give us some estimate of the nucleation barrier even in the weakly supercooled regime. This could allow us to establish whether the nucleation barrier heights in our experiment grow rapidly with decreasing supersaturation, as in simulations, or much more slowly, as in experiments, without having to measure the barrier heights themselves, with the associated prohibitively long experimental times.

Inspired by the work of Ketzetzi *et al.*[132] we therefore propose measurements of the nucleation barrier. This is done by counting the number of crystal nuclei at of a size n, and using Equation 5.1.

$$\Delta G(n) = -k_B T \ln(\tfrac{N_n}{N}) \tag{5.1}$$

Where N_n are the number of clusters of size n, $\Delta G(n)$ is the effective free energy of forming a cluster of size n, and N is the total number of particles in the system. For a full derivation of this relationship see Auer and Frenkel (2004)[122].

5.2 EXPERIMENTAL SYSTEM

This work uses PMMA particles purchased from Edinburgh Innovations. These particles have a quoted 303nm diameter as found through x-ray crystallography. They are sterically stabilised using short PHSA chains. The particles are dyed with the commercial NBD-TMA dye, which has a fluorescent excitation maximum at 458nm and an emission maximum at 530nm[198]. The solvent used is a CHB cis-decalin mixture which matches the refractive index and the density simultaneously, as before. To check the size the particles were imaged with a scanning electron microscope, and the sizes measured in the images by hand. Fig. 5.1 shows the size distribution of the particles. We found they were in fact distributed with a mean diameter of 392nm, and standard deviation of 28nm, giving a polydispersity of 7%.

5.3 MEASURING CRYSTAL NUCLEI

We wish to measure nucleation rate densities, and so therefore we wish to count nuclei. In order to do this, we need a technique which, given a large confocal image, can return the location and, ideally, size and shape of any crystalline regions that exist within that image. Given that we wish to leave aside particle-tracked methods, one option

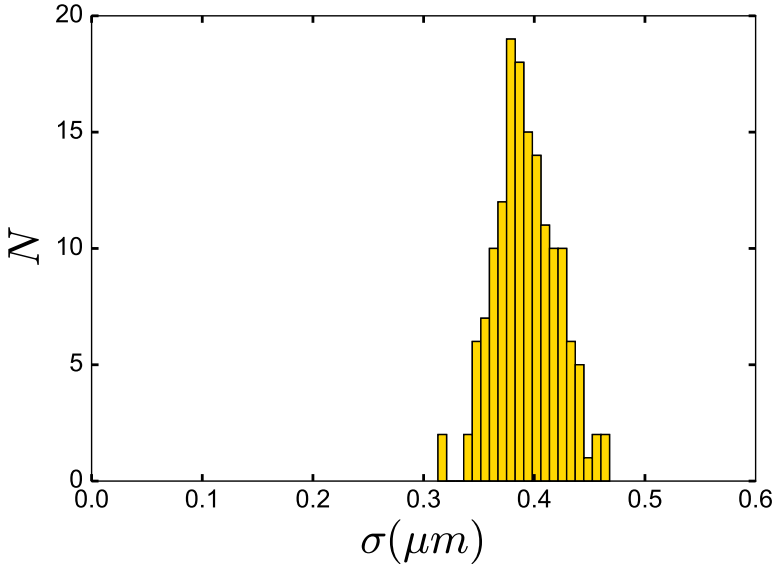

Figure 5.1: The size distribution of the particles used in this chapter, taken from an SEM micrograph.

is to return to a scattering-style reciprocal space method. A Fourier transform of an image that contains crystal regions should look very different to that of a liquid region - the crystal region will show sharp peaks corresponding to the lattice spacing of the crystal, whilst the liquid will show a ring pattern, with the most intense point of the ring existing at a distance of $\frac{1}{\sigma}$ from the centre (corresponding in real space to the first peak of the radial distribution function). We can therefore identify when a region of the sample is crystal, and when it is liquid.

However, simply taking the Fourier transform of our images and identifying peaks is unlikely to be very helpful. If we wish to take very large images of very small particles in order to increase our sampled volume, a single image may contain many nuclei. These will be oriented differently with respect to the focal plane of the microscope, and therefore will contribute low-intensity peaks in various different places which will be difficult to detect. The alternative to this is to section the images into smaller parts, and run a Fourier transform on each of these smaller images. This method allows us to locate crystal nuclei in space, and understand something about their shape and size, without having to run costly particle tracking. A schematic diagram of the method is shown in Fig. 5.2.

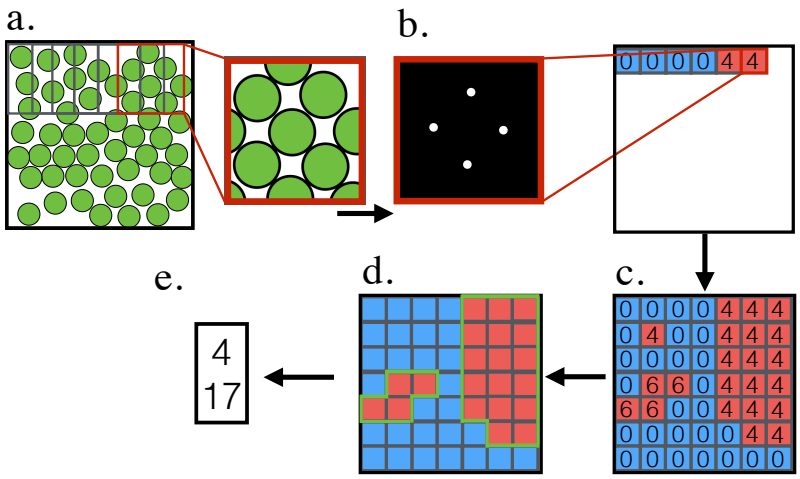

Figure 5.2: A schematic diagram of the real space-reciprocal space method used in this chapter. This is shown in 2 dimensions, but the full analysis is performed in 3. **a.** The initial image is cropped to a smaller subimage. This is repeated across a lattice in which sub-regions are allowed to overlap, to increase resolution and limit the importance of the location of the grid. **b.** A fast Fourier transform is performed on the subimage, and four crystal peaks are revealed. These are identified and their number is stored in a result array, which contains the result for every subimage. **c.** After every subregion is scanned, a full results array has been built up. **d.** The results array is processed. This involves filtering, which has removed a spurious crystal detection in the upper left corner, and potentially other processing. It also involves labelling distinct regions of crystal, shown by the green outline. **e.** The final result is a list of nuclei sizes in the detected image.

5.3.1 Choice of Imaging Parameters

A typical deeply-zoomed out image is shown in Figure 5.3. This image size is chosen by eye to be the maximum size image which still has features which can be resolved over the natural imaging noise. This image is 43.4µm across, meaning each single xy image contains around 5000 particles, already a 5 times improvement on the work with larger particles. When taking into account a full z-stack the improvement in the number of particles is around 20 times - with on the order of 10^6 particles instead of around $5 * 10^4$ particles[196,199]. By taking multiple stacks across the entire sample of this size, we can improve this much further, and finally end up with around 2 to 3 orders of magnitude more particles imaged than in a previous typical confocal measurement. Combining this with the order of magnitude increase in the relaxation time from the smaller particles opens up a whole

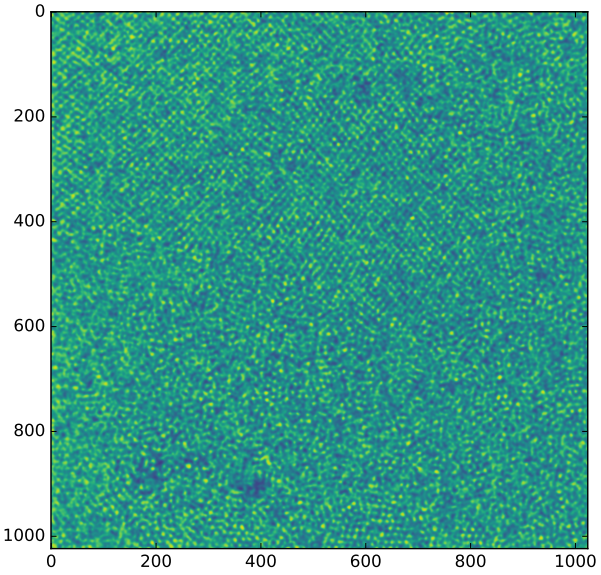

Figure 5.3: A representative deeply zoomed out image of the particles used in this work.

region of the range of nucleation rate densities to confocal techniques for the first time.

In order to keep the analysis time to a reasonable length, we compromise on the z-resolution of our images. Instead of having around 10 pixels per particle, as in XY, just 3 are taken in Z. This number was chosen considering that good images of any crystal nuclei which have planes near parallel to the image plane will only be taken if the imaging plane intersects with the crystal plane. The choice of 3 slices per particle diameter means that the maximum distance between the crystal plane and the imaging plane is $\frac{1}{6}\sigma$ which was deemed to be acceptable.

5.3.2 Identifying Crystal Peaks

Once we have the Fourier transform of the subsection of the microscope image, we need to locate any crystalline peaks. There are many existing implementations of algorithms which can find local maxima within images, in this work we use the peak_local_max algorithm from the python scikit-image library[200]. This function has two free parameters. The minimum peak separation removes the less bright peak from pairs of peaks which are closer than the threshold distance, whilst the intensity threshold removes any detected peaks which have a lower intensity than a chosen fraction of the maximum intensity of the image. Choosing a threshold value of around half the average

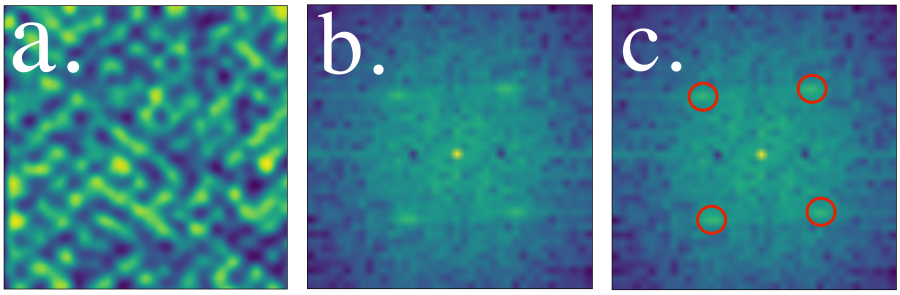

Figure 5.4: **a.** A typical crystalline subregion. **b.** The fourier transform of this subimage. **c.** The four crystal peaks as identified by the peak_local_max algorithm (we remove the central bright spot). This subregion would therefore be coded as containing 4 crystal peaks.

image intensity and a minimum peak separation that corresponds to just under σ in reciprocal space does a good job of finding peaks which exist in clearly crystal regions.

However, with these parameters the peak detection algorithm can sometimes find peaks in non-crystalline regions, which are clearly disordered liquids. The liquid ring pattern is itself more intense than the rest of the image, and if noise breaks up the ring sufficiently, parts of it can be seen as peaks. A further method to distinguish spurious from non-spurious peaks is therefore required. One way of doing this is by testing for the presence of the liquid ring. The ring is a clear feature which exists at a known distance from the centre of the image, and will not exist in regions which are clearly crystalline. By calculating the average image intensity at the ring distance, and divide the average intensity of the detected peaks by the ring intensity, we arrive at a measure of the likelihood that the peaks in fact belong to a ring structure. A threshold value can be chosen to separate true crystal from spurious crystal, though it should be noted that not all spurious crystal is misidentified liquid - images which are of the border between liquid and crystal can often contain both a reasonably intense ring and identified peaks.

Figure 5.5 shows the amount of identified pure crystal as we increase the required threshold for crystallinity. It was hoped that there would be a sharp distinction between the spurious liquid regions and the border regions, such that a particular choice of the threshold would remove the former but retain the latter. Unfortunately, this does not appear to be the case, and in fact there is a smooth change in the threshold from all crystal being found to be spurious and none at all. This is somewhat to be expected given that sub-images which include

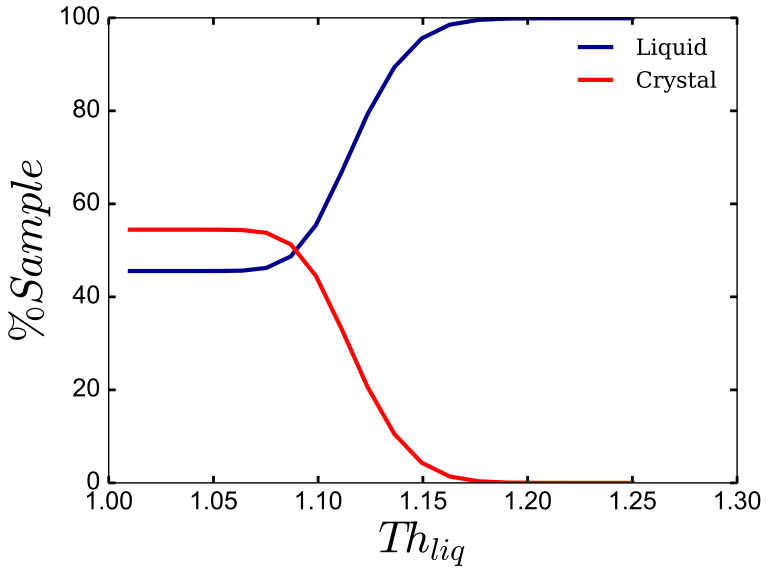

Figure 5.5: The effect on the measured amounts of crystal and liquid as we change the liquid ring threshold. The higher the value of the threshold, the more intense the crystal peaks have to be relative to the liquid ring for the subimage to be classified as crystal. We see that almost all detected crystal peaks are 10% higher than the ring thresholds, but more stringent thresholding reduces the amount of crystal.

the liquid-crystal border will show peaks and a ring, and the height of the ring will vary continuously with the ratio of liquid and crystal contained in the sub-image. We therefore take a very high choice of the threshold 1.08, which filters only the most obviously liquid-like regions out, whilst retaining almost everything else as crystal. In fact, the issue of spurious liquid is dealt with in a more complete way with other processing tools (see below).

5.3.3 Further Analysis

When we have completed our "Fourier scan" of the image, we have an array which breaks the image up into regions of crystal and regions of liquid. We would like to move from these images to a measurement of nucleation barriers, and from there to a measurement of the nucleation rate density. To measure the nucleation barriers, we require the size distribution of the nuclei. The size distribution of nuclei can be measured from our "Fourier scan" images, we simply need to count the volume of each nucleus, and then plot a histogram of the number of nuclei at each volume.

The first step then is to separate the nuclei. This means moving from our array in which each element is numbered according to the crystal status of the corresponding chunk of the original image, to one in which each independent, unconnected region of crystal is labelled separately. The algorithm written in python which can do this efficiently is from the scipy library - "scipy.ndimage.measurements.label"[201]. The only choice made when using this algorithm is the structuring element, which defines the condition for neighbourhood between two points. We choose a cross structuring element, meaning that crystalline points which are diagonally adjacent but with no horizontal or vertical neighbours are not counted as being part of the same nucleus.

When we perform this labelling, we often find many tiny nuclei (volumes smaller than a single particle) or very extended nuclei (lines of crystal with a very small width). These are due to erroneous peak detections or imagine artefacts. We can be certain, however, that these regions do not correspond to real nuclei, as real nuclei have to be made of particles, and so any nucleus with any dimension lower than a particle diameter cannot be real. This issue could potentially be resolved with a simple filter removing any nuclei which are too small. However, some of these spurious crystallites are not isolated in space, where they could be identified as nuclei and filtered out. Instead, the protrude out from larger, genuine nuclei, sometimes connecting two quite separate crystal nuclei into a much larger, highly non-spherical nucleus. In fact, when we run the algorithm as described so far, we find that almost 30% of the sample is contained within one huge, highly non-spherical cluster. A simple size filter will not address these effects alone. Whilst we apply a filter to ensure that no nucleus is smaller than the volume of a single particle, we also perform an erosion operation. This erosion shaves away the edges of the nuclei, meaning that thin tendrils are removed, breaking up the spurious huge non-spherical clusters. The side-effect of this operation is that true nuclei are eroded, reducing their volume. This effect can be compensated for by applying a dilation step to the eroded clusters, which undoes the erosion operation and (approximately) corrects their volume.

There is a tradeoff to be made when choosing the extent of the erosion that should be performed on our Fourier scan images. Too little erosion and the spurious nuclei may not all be removed, but too much and we remove the fine surface detail of our real nuclei. Whilst we can compensate the measured volume of the nuclei quite well by dilating the nuclei, this loses the real surface of the nuclei which we might be interested in. The more times we erode, the more information we lose. We therefore want to erode as little as possible.

5.3.3.1 Choosing Correct Number of Erosion/Dilation Cycles

When we erode and dilate our nuclei, we expect that for small numbers of erosion/dilation cycles, we should mostly be removing thin tendrils which are spuriously connecting multiple nuclei. We may also be destroying small clusters that just survived the initial size filter. In the case that the former effect is most important, we should see an increase in the number of clusters we find after the erosion, whereas if the latter is most important, we should see a decrease in the cluster numbers. As the number of erosion cycles increases, eventually the tendrils will all be broken, and we will see a decrease in the number of clusters as the erosion removes more and more. We should also see a sharp increase in the average sphericity of our nuclei for small number of steps as the highly non-spherical nuclei are broken up. This will be followed by a shallower increase in sphericity as the erosion removes the finer detail of the nuclei surfaces. We therefore wish to pick the number of erosion steps which is associated with an increase in the number of nuclei, and a rapid increase in their sphericity.

The sphericity of a cluster can be found by measuring its surface area and volume, and taking the ratio of the surface area of the cluster to the surface area of a perfect sphere of the same volume. This quantity is given by Equation 5.2[202].

$$\Psi = \frac{\pi^{\frac{1}{3}}(6V)^{\frac{2}{3}}}{A} \tag{5.2}$$

Where V is the volume of the sphere and A is the surface area of the sphere. It is equal to one for a perfectly spherical cluster, but for any non-spherical cluster it is smaller than one (as the sphere is the lowest possible surface area for a given volume). To find the surface area of the clusters, we test each region identified as crystal for neighbours which are not themselves part of the same region of crystal. We then count the total number of neighbours in both XY and Z (as the surface area of an XZ or YZ face is not equal to that of an XY face), and multiply by the surface area of a single face. The final cluster surface area is the sum of these faces. The volume is simply given by the number of pixels found in the cluster multiplied by the volume of a single pixel. We can then calculate the final sphericity from Equation 5.2.

Fig. 5.6 shows the behaviour of the number of nuclei and their mean sphericity with more erosion/dilation cycles. We see the expected behaviour, with nuclei populations increasing sharply for low numbers of cycles, and then falling. The sphericity also climbs rapidly, before flattening out. We choose to use 2 erosion dilation cycles for the

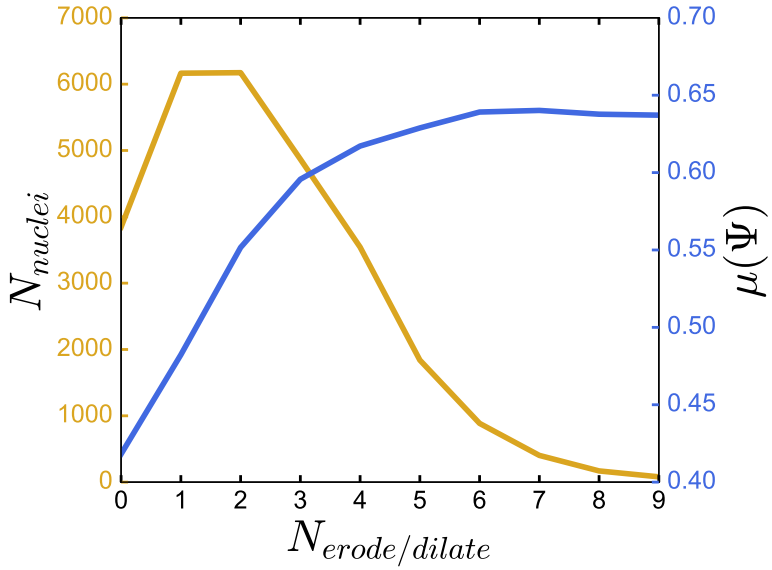

Figure 5.6: The behaviour of the number of nuclei (left, yellow), and the mean nucleus sphericity (right, blue), with increasing numbers of erosion and dilation cycles. This data is taken from a sample of PMMA particles at $\Phi = 0.33$.

processing, as this strikes a good balance between preserving the small nuclei, whilst removing spurious, highly non-spherical nuclei.

Fig. 5.7 shows the steps from Fig 5.3, but now with real images and processing steps.

5.4 CALIBRATING RESULTS

The image analysis so far gives us a method to locate crystal nuclei. However, so far the size of the nuclei have not been determined. We can find regions which return crystal-like fourier transforms, but mapping these to real particle sizes is not trivial. Regions with only a small amount of crystal on the edge may show crystal peaks, but we would count the entire region as crystalline, we will therefore substantially over-count crystal regions using the results naively. We need some way to move from our crystal maps to real nucleus sizes. We also need to characterise the quality of this analysis - how often are truly crystal regions correctly classified, and what is the false-positive rate on liquid regions?

In order to answer these questions, we run simulations of crystal nuclei surrounded by liquid. These simulations are performed using LAMMPS molecular dynamics code[203]. The crystal nucleus is created at the centre of the simulation box with an FCC lattice at $\Phi = 0.545$,

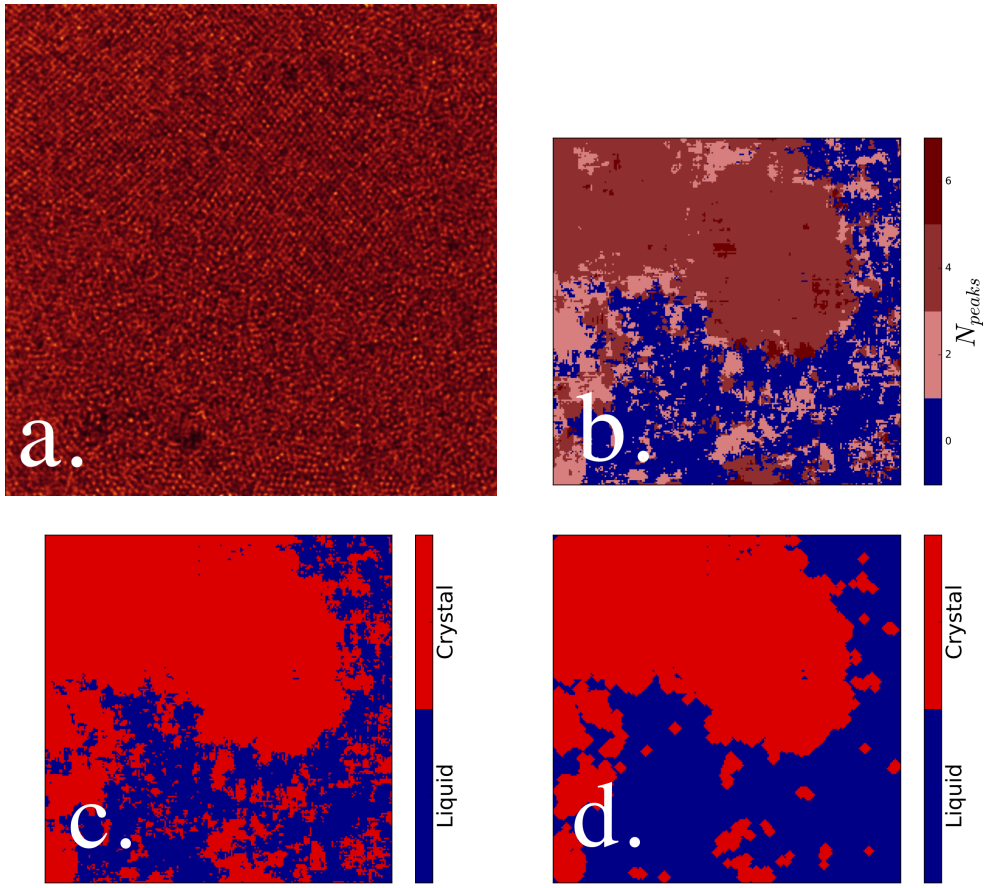

Figure 5.7: The process of scanning an image and categorising it into liquid and crystal regions. **a.** The original 1024 by 1024 microscope image. This image is chosen as it displays clear crystalline ordering in the upper portion of the image, and a clearly disordered liquid in the lower portion. **b.** The result of running the Fourier scanning algorithm on the image. This image is smaller than the original microscope image due to the scanning algorithm losing the edges of the images. **c.** Result after binarising into crystal and non crystal regions. **d.** After 2 erosion/dilation cycles, the noise in the image is removed, leaving only the larger crystal structure for labelling and sizing.

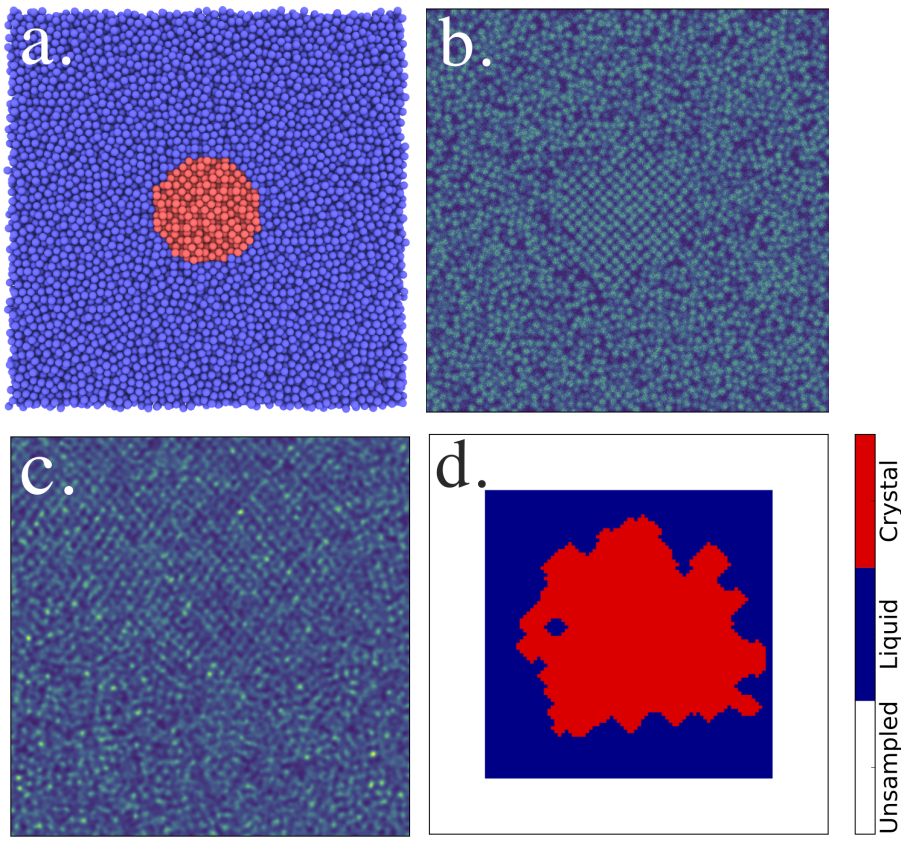

Figure 5.8: The process of generating calibration data. **a.** A simulation containing a crystal seed with a radius of seven particle diameters. Shown in red are the crystalline particles, and in blue the surrounding liquid. **b.** The same configuration as a simulated experimental image. **c.** A real experimental image for comparison. This image shows both crystalline and liquid regions, and is shown so a particle diameter in both images is the same size. **d.** The result of analysing the image in b. with the Fourier scanning code.

whilst the surrounding liquid is at $\Phi = 0.52$. The liquid is generated by taking random positions, and then relaxed using an energy/force minimisation, whilst the crystal is held in position. The potential used is the Week-Chandler-Anderson (WCA)[204], which can be mapped to the hard sphere model by use of an effective diameter[5]. The configurations are then run in the NVT ensemble for 1000 timesteps to allow the crystal to relax away from a perfect lattice.

Using the technique described in section 4.6.1.3, we can move from these simulation configurations to representative experimental images. See Fig. 5.8 b, c, for a comparison between real experimental images and those generated from the simulation configurations. These images are sliced in Z to give the same resolution as the experimental images in all three dimensions (see section 5.3.1). As the process of generating

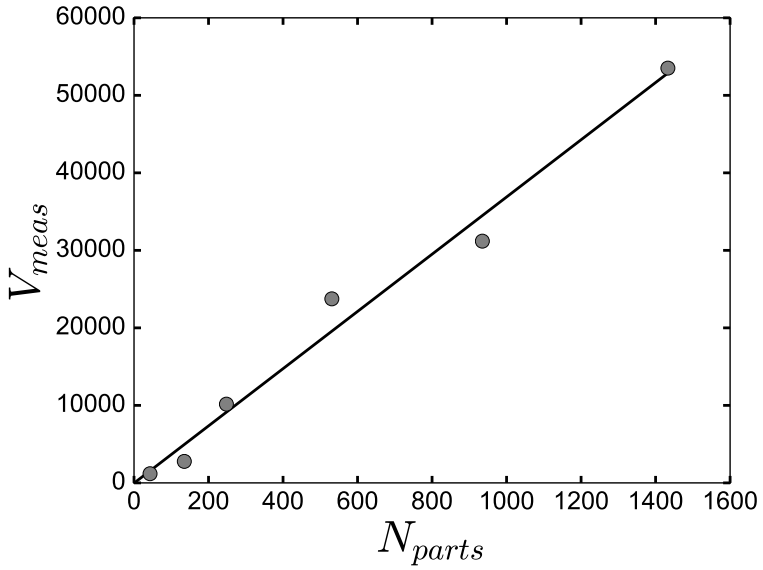

Figure 5.9: The size of the nucleus found when seeding simulated experimental images with nuclei of known sizes. Error bars are plotted for the same set of simulated images with separate noise generation steps, but the are smaller than the points shown. Y axis volumes are shown in the unit of final scanned "pixels" measured.

the images is expensive, we choose to only generate simulations that are 50 particle diameters wide in XY and 20 particle diameters in Z. This means that in XY we are looking at a representative image which is 463 pixels wide, and in Z, 60 sections deep. This is in contrast to the real experimental images which are 1024 pixels wide and 300 sections deep. These are large enough boxes to contain large nuclei and liquid regions which can be scanned over, whilst restraining the time to generate each set of images to around 2 hours. All other scanning parameters (thresholds for peak detection, erosion steps, labelling choices etc) are as described previously.

Fig. 5.8 shows the full process of moving from a simulation configuration through a simulated experimental image, and on to a final result. The crystal in Fig. 5.8 d. is larger than it appears in the simulation or simulated experimental image. This is because the scanning process is seeing crystalline peaks even when the centre of the subregion is reasonably far from the crystal. These peaks then cause the entire subregion to be classified as crystalline, even when the majority of the image may be a liquid. This boosts the overall size of the crystal nuclei.

The result of this analysis is shown in Fig. 5.9. We have a clear linear dependance of the measured size of the nucleus on the volume of the seeded nuclei. The linear fit in Fig. 5.9 is not forced through the origin,

it intercepts the y axis at a value of -33. The gradient of the linear fit line is 36.88, implying that this is the volume of a single crystalline particle in the results space after the Fourier scanning algorithm. This can be used to normalise our results when calculating nucleation barriers. There is some clear scatter of our points away from the line of best fit. In fact, the average distance from the best fit line is around 25% of the nucleus size. This is an estimation of the error on our nucleus sizes, which we will use in later analysis. We found some false positive nuclei that were not fully removed by the erosion/dilation steps. These were quite small however, with volumes less than 100 pixels in the Fourier results space, a true volume of less than 4 particle volumes.

5.5 DETERMINING VOLUME FRACTIONS

5.5.1 Method

Given the difficulty of determining volume fractions accurately, we might well ask how we know that the literature experimental volume fractions are accurate. The answer lies in the fact that the literature experiments used scattering techniques which measure the final equilibrium crystallinity (X) of the samples at a given volume fraction (see section 1.5.5.1). This has many advantages.

Measuring the crystallinity of the sample is very preferable to measuring the raw volume fraction, as the measurement of the crystallinity collapses onto *only the coexistence region*, which is only about 5% of the total range of the volume fraction. The difficulty in measuring the raw volume fraction is that errors of just 1% make a huge difference to the expected nucleation rate. However, errors of 1% in the crystallinity correspond to an error of just 0.05% in the volume fraction. We therefore have quite some leeway in measuring the crystallinity, whilst still finding reasonable volume fractions.

Generally, experimentalists using scattering techniques to measure nucleation embedded small pieces of paramagnetic wire into their sample, which could be used to shear melt and re-randomise the colloids. This meant that a single sample could have its volume fraction measured, be shear melted, and the nucleation rate could then be measured several times. We do not use paramagnetic wire, which means that we can only take measurements on each sample once.

The experimental method we devise to measure the volume fractions and the rates of our samples uses several capillaries. Generally three capillaries are used to measure the volume fraction, and one more is

used to measure the nucleation rate. We split the samples for several reasons. Firstly, the capillaries which measure the volume fraction mean we have 3 independent samples, which give us a more accurate volume fraction and some understanding of its error. Secondly, splitting the samples means we can use non-sintered, rectangular capillaries for the crystallinity measurements. Making sintered capillaries is a difficult process with relatively low yields, and it is best to keep sintered capillaries for only those experiments which require them. Our sintered capillaries are also square, and their depth is larger than the microscope can fully reach, meaning measuring the final amount of crystal in them would have a very large error. Our microscope can travel the entire length and depth of rectangular non-sintered capillaries, so we can check the crystallinity of the entire sample. Samples contained within non-sintered capillaries will also crystallise much more quickly than sintered capillaries, as the nucleation barrier against the walls will be much smaller. However, the final crystallinity in the non-sintered capillaries will be equal to the final crystallinity in the sintered capillaries, as changing the nucleation barrier should only change the rate of crystallisation, not the thermodynamics uniquely controlled by the volume fraction which determines the crystallinity.

In order to actually determine the final crystallinity, we originally simply filled our capillaries with a colloidal dispersion, waited for several days when the crystallisation process should have finished. Then by taking microscope images across the entire length and depth of the capillary (in practise many hundreds), and testing each image for crystallinity. The crystallinity of the sample is then simply the number of images with crystal divided by the total number of images. This could be developed further by counting the amount of crystal in each image, and weighting the contribution to the crystallinity by this amount. The problem with this method is that it has a relatively high error, as even with hundreds of images the entire sample cannot be measured. The crystal nucleates from the walls preferentially, but does this at random, resulting in a complex crystal pattern which is hard to sample properly. By chance, an alternative method was found. When a capillary was accidentally not completely filled, the colloidal crystal preferentially nucleated from the air-solvent interface, rather than the air-wall interface. This resulted in quite a clean separation between colloidal crystal and colloidal liquid, and the task is then to determine the position of the interface between the two phases. This can be measured quite precisely - even if we have an error of 100 particle diameters, as the capillaries are on the order of several centimetres long this is an error of 0.3% on the crystallinity, or 0.015% on the

volume fraction. This is quite easily the most precise determination of the volume fraction done in confocal experiments.

5.5.2 Results

In order to reliably assess the position of the liquid-crystal interface we take images across the entire capillary. By eye, we then establish the approximate position of the interface. A more detailed scan is then taken, imaging the entire sample in the region around the interface in XY in one Z plane. We run 3 of these XY scans at different heights through the capillary to make sure that the boundary position is not changing in Z. These scans are at one quarter, one half, and 3 quarters of the depth of the capillary. We can use the known position of the microscope stage to measure the distance from one corner of these XY scans to the edge of the sample, near the air bubble. We can therefore find the distance from the bubble to the edge of the interface, and by dividing this length by the length of the entire capillary we arrive at the crystallinity. There is therefore a further error on the crystallinity, that is the length of the entire capillary. Whilst we could simply measure each capillary with a ruler before filling them with the sample, this method would not truly capture the volume actually available to the particles. This is because the glue used to seal the capillary tends to slightly invade the sample by a few tens to hundreds of microns. To accurately account for this reduction, during the data collection we can measure the location of the particles closest to the glue which are still moving. These particles should be the first which are unaffected by the presence of the glue, and this gives us a more accurate estimation of the true length of the capillary.

Once we have these images, we need an objective way of measuring their crystallinity. In order to do this, we measure the relative height of the liquid ring signal relative to the rest of the image. We know that the liquid ring should have a maximum intensity at a distance which corresponds to the diameter of the particles in reciprocal space. In the case of our particles, which are about 8.5 pixels across in the 1024 by 1024 image, this means the ring maximum should be at around 120 pixels from the centre of the Fourier image. The final measured quantity is the ratio of the average intensity of the pixels which are 120 pixels from the centre of the image, divided by the average intensity of the rest of the image. The ring intensity in a region which is clearly liquid is around 3% higher than the rest of the image. In a crystalline region, meanwhile, the signal is concentrated in the crystal peaks, and the average ring intensity is essentially equal to the intensity of the

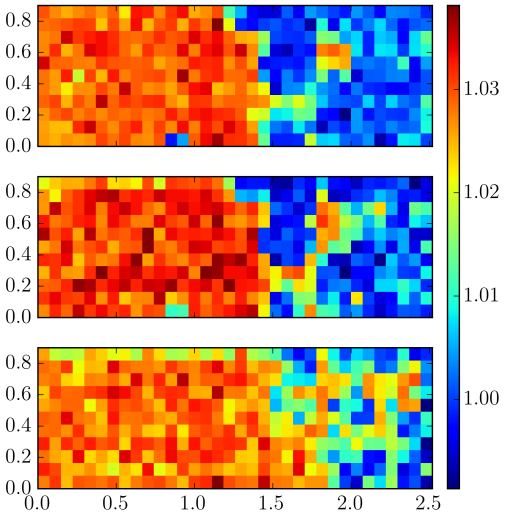

Figure 5.10: The crystal-liquid boundary in 3 different z planes for a sample. X, Y numbers are distances in milimeters. Colour coding is by the intensity of the liquid ring in the fourier transform of each images. The boundary becomes slightly less clear in the deepest image (the bottom image), this is because the imaging is slightly worse in the deeper planes. Nevertheless, the position of the boundary can be clearly measured, giving an estimate of the crystallinity of the sample.

rest of the image. Whilst a 3% difference does not seem huge, in fact there is a sharp delineation between the crystal regions and the liquid regions, see Figure 5.10. From fitting the coexistence line in Fig. 5.10, we find $\Phi_f = 0.293$ and $\Phi_m = 0.330$ for this system.

It is therefore possible to measure the crystallinity of the heterogeneously nucleating samples, and therefore arrive at an estimate of the volume fraction. However, as discussed previously, it is unlikely that our particles will crystallise at the theoretical hard-sphere volume fraction. This is due to several factors, most notably charge and polydispersity. The particles are around 7% polydisperse, which will shift the phase boundaries by several percent[134]. The charge, meanwhile, will cause the particles to have slightly increased effective diameters, which will mean that the measured volume fractions from the experimental preparation will be too low. As the volume fraction increases with the diameter cubed, even small changes in the effective diameter can shift the volume fractions very substantially. It's therefore necessary to rescale our measured volume fractions to the freezing line of hard spheres, as was done in the scattering literature.

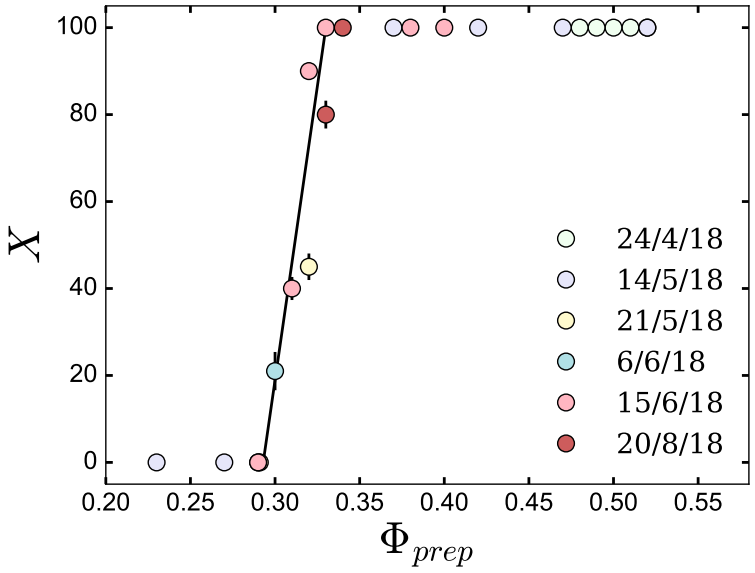

Figure 5.11: The measured crystallinities of samples with their prepared volume fraction. Colours show separate experimental runs and the dates on which they were performed. Samples above $\Phi = 0.45$ were a mixture of crystal regions and amorphous glass, and are shown here for completeness.

Figure 5.11 shows the measured crystallinity of samples with increasing volume fraction. As expected, there is a sharp transition from a liquid to a solid state, with an intermediary coexistence zone, in which the amount of crystal varies linearly with volume fraction. The volume fractions here are quoted from the experimental preparation, which explains the difference from the theoretical phase boundaries. The freezing line at $\Phi = 0.30$ is fairly similar to that of Gasser *et al.*[32], who observed freezing to begin at $\Phi = 0.38$. The error bars show the standard deviation on the measured crystallinities for all of the samples for each prepared volume fraction point.

Clearly the errors on our measurement are worse than described in section 5.5.1. Instead of a crystallinity error of 0.3%, we instead see errors on the order of 5%. This increased error likely results from nucleation elsewhere in the sample than the section that we measure. Even with the crystal nucleating preferentially from one wall, heterogenous nucleation will likely take place throughout the sample, and so the procedure from section 5.5.1 will underestimate the true crystallinities. The are other sources of error as well, such as defects in the crystal region which will increase the measured volume.

Table 5.1: The Yukawa parameters for the $\sigma = 392nm$ PMMA particles

ϵ_r	λ_B	κ	$\beta\epsilon_Y$
5.6	1.00×10^{-8}	1.98×10^{7}	58.92

5.5.3 Understanding The Phase Diagram

As mentioned, Figure 5.11 is not in agreement with the hard sphere phase diagram, which has a freezing line at $\Phi = 0.494$ and a melting line at $\Phi = 0.545$. To some extent, this can be explained by systematic errors in our preparation as discussed in section 2.5. These are not large enough to fully explain a 19% change in the freezing line, however. We therefore explore two possibilities to explain this change, polydispersity and charge.

Polydispersity does change the freezing and melting lines of hard spheres, but it pushes them in the wrong direction. A polydispersity of 7% should increase the coexistence lines by about 0.02[189]. It might be thought that the polydispersity itself could change the measured volume fractions, but as we measure the solid mass of PMMA (rather than say, the number of particles), volume fractions of samples prepared using our method should be insensitive to the polydispersity.

To account for charge, we repeat the analysis of section 3.2.5.2 to find the relevant Hard Core Yukawa parameters for our particle system. As the chemistry is identical, with PMMA in a density/refractive index matching binary mixture of cis-decalin and CHB, this means only changing the particle size. For particles with $\sigma = 392nm$ we expect the Yukawa parameters given in table 5.1.

These parameters give us some feel for where we would expect the phase boundaries to exist. We could perform a “mapping" of this system onto hard spheres, taking a Barker-Henderson effective Hard Sphere diameter, for example, as given in equation 5.3[205].

$$\sigma_{BH} = \int_0^\infty [1 - \exp(-\beta u(r))] dr \tag{5.3}$$

Performing this integration for the parameters given in Table 5.1 gives a final effective hard sphere diameter of 605nm. We would therefore expect a sample prepared at a volume fraction of 0.3 to have an effective volume fraction of more than 1.0, as particles with diameter 605nm have almost four times more volume than those with a diameter of 392nm. This is clearly not what we see, and there are two possible reasons for this.

To understand the first, we need to re-examine the preparation process. Particles of PMMA are centrifuged to a pellet at random close packing, $\Phi = 0.64$. This pellet is then weighed, and through the PMMA density we arrive at the volume of PMMA in the pellet. The pellet is then diluted with extra density matched solvent to reach the desired packing fraction. The key question is whether the particles truly pack to $\Phi = 0.64$, meaning that the centrifuge can push the particles through the Yukawa repulsion until they are separated by just the steric stabilisation layer, or whether the particles remain some further distance apart due to the Yukawa potential. In the former case, we expect that the particles to later expand to their effective size, and we'd expect an effective diameter scaling to be quite effective. In the latter case, however, it is unclear that an effective diameter scaling will work.

We can roughly calculate which of these two is likely. The negative of the derivative of the potential with respect to distance gives us the force needed to overcome the potential. The negative of the derivative of the Yukawa potential at contact is 1.660×10^{-18}N. This is the force needed. The force exerted on the particle by the centrifuge can be found simply using $F = ma$, with $a = (2\pi n)^2 r^{206}$. The apparent mass of the particles depends on the size of the density difference between them and the solvent. They are density matched, but a small amount of heating breaks the matching by altering the densities of the solvent. Data quoting density as a function of temperature for CHB is difficult to find, but data for cis-decalin[207] shows a 1.5% change in density from 20 to 30 degrees Celsius, similar to our conditions. This gives a final force on each particle equal to around 6.21×10^{-18}N. We'd therefore expect the centrifuge to be able to overcome the Yukawa potential, but only by around half an order of magnitude. Indeed, smaller particles which are located close to the tip of the centrifuge (and therefore feel a smaller acceleration), may not entirely meet at the steric length scale.

Given these calculations, we wouldn't expect every particle to be perfectly close-packed, and therefore our supernatant will not be at $\Phi = 0.64$. We therefore are unable to simple scale to a Barker-Henderson effective volume fraction, as our initial volume fractions will likely be wrong due to the Yukawa repulsion.

The second reason to be sceptical of a Barker-Henderson style scaling is that we are by no means certain that the parameters quoted in Table 5.1 are correct. The same solvent was used for these experiments as those in Chapter 3, and we saw a substantially smaller degree of electrostatic interaction to the theoretical prediction. In fact, there's another good reason to be sceptical of these numbers. We can cross

reference with the work of Auer and Frenkel[25] and Hynninen and Dijkstra[208], who measured the positions of the phase boundaries for hard-core Yukawa particles with different parameter choices. The values given in Table 5.1 result in substantially lower positions of the phase boundaries, with freezing occurring closer to $\Phi = 0.2$ than $\Phi = 0.3$. A freezing line at $\Phi = 0.3$ would require $\beta\epsilon_Y \approx 15$ for a $1/\kappa\sigma = 0.13$, as in Table 5.1, or $1/\kappa\sigma \approx 0.5$ for $\beta\epsilon_Y = 58.92$. If we leave the empirical rule of thumb for the surface charge of $Z\lambda_B/\sigma = 6$[76], and alter only the degree of dissociation of the salt to match the phase boundaries, we find an increase to 3.5% from the 2% measured by Leunissen[172]. This would also explain the results from section 3.2.5.2, if the salt is dissociating to this extent then the Barker-Henderson diameter for the CHB rich system will be 2.15µm, whilst for the cis-decalin rich system it is 2.07µm, a difference of around 4% which will be difficult to resolve using the radial distribution function. This argument is only indicative, and it is likely that the cause of the electrostatics being weaker than expected is a combination of the ionic strength of the solvent[76,172,175], a different degree of surface charging than predicted by the empirical rule[76], and alteration of the electrostatics on increasing volume fraction[209–211].

We therefore proceed not by mapping to an effective hard sphere diameter, but by quoting just the prepared volume fractions. If we wish later to compare to other weakly charged systems, or hard spheres, we can compare using the distances from the freezing line. This is in line with the procedure followed by Pusey *et al.* when studying nucleation of polydisperse hard spheres, and Auer and Frenkel[25] when studying nucleation of weakly charged colloids. This will preclude measuring nucleation rates which can be directly compared to the simulations of Fig. 1.3. However, we can still directly compare to the weakly charged rates given by Auer and Frenkel[25], who measure an incredibly steep dependence of the nucleation rate on the packing fraction, similar to the hard sphere case. A similar discrepancy exists in the weakly charged case, with Gasser *et al.*[32] measuring a much weaker dependence.

5.6 NUCLEATION BARRIERS - RESULTS

We perform the full nuclei size analysis on three samples in the coexistence regime. These are the data from the 6th June 2018 ($\Phi_{prep} = 0.30$), 21st May 2018 ($\Phi_{prep} = 0.31$) and 20th August 2018 ($\Phi_{prep} = 0.32$). These three samples are chosen as they give a good spread across the coexistence regime.

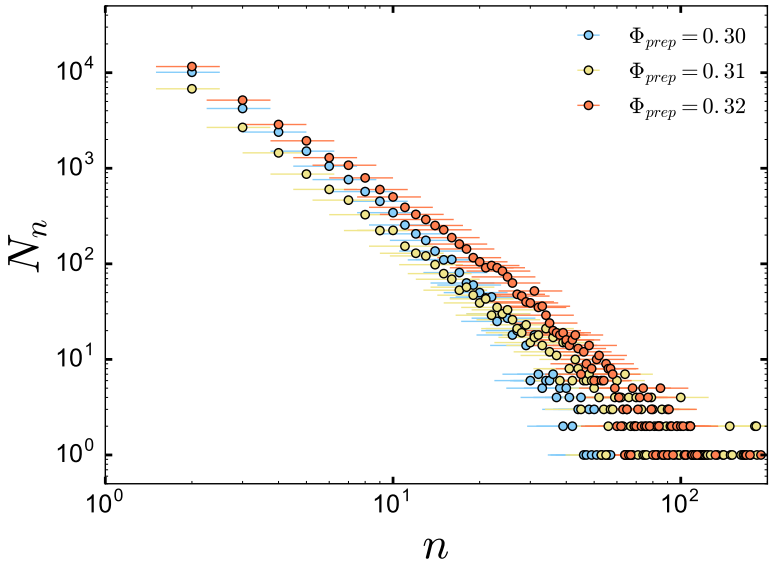

Figure 5.12: The distributions of the sizes of the detected nuclei in three experimental samples. The sizes are measured in units of number of constituent particles in each nucleus, n. The x-error bar shows the 25% error in the nucleus size, as determined in section 5.4

Fig. 5.12 shows the measured nuclei size distributions for these three samples. We see robust results up to around a nucleus size of $n = 30$, after which the measurement becomes more noisy, as we see fewer than 20 nuclei for each cluster size larger than this. Interestingly, the sample at $\Phi_{\mathrm{prep}} = 0.30$ contains more small nuclei than the sample at $\Phi_{\mathrm{prep}} = 0.31$, but fewer large nuclei. The sample at $\Phi_{\mathrm{prep}} = 0.32$ always contains many more nuclei at all sizes, than the other two samples, as expected. These results are similar to those of Bonn *et al.* but we see around 2 orders of magnitude more clusters for each size, and see clusters around 5 times larger than their maximum size.

In order to move from the distributions in Fig. 5.12 to nucleation barriers, we need to know the total number of particles[122]. This is found by multiplying the total volume of all of the samples by the prepared particle number density. Using equation 5.1 we can then calculate the barriers.

Fig 5.13 shows the measured nucleation barriers. The barriers for $\Phi_{\mathrm{prep}} = 0.30$ agrees reasonably well with the hard sphere result for $\Phi = 0.53$, whilst the other barriers are both curving below this result. A noticeable difference between our barriers and those of the simulations is that our barriers show a very sharp increase in the free energy for small nucleus sizes, sharper than even that for the deeply supercooled $\Phi_{\mathrm{HS}} = 0.52$. This may be due to a systematic error in our

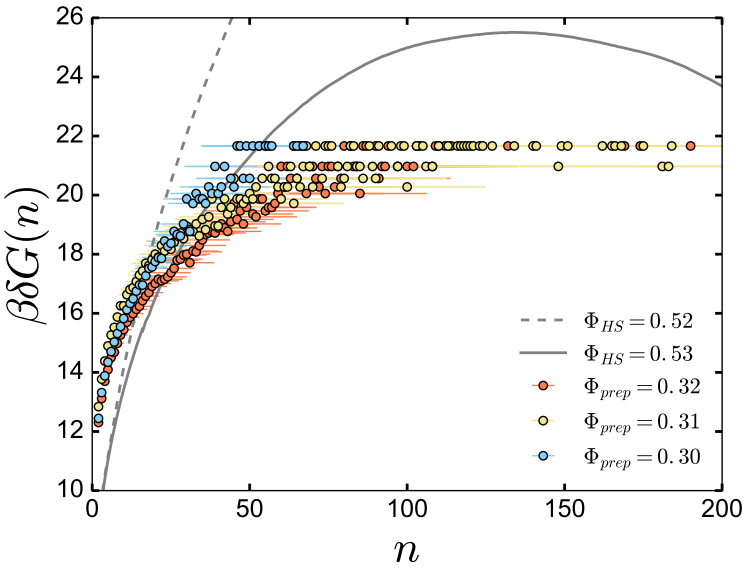

Figure 5.13: The measured nucleation barriers for three experimental samples. The x-error bar shows the 25% error in the nucleus size, as determined in section 5.4. Dashed and filled lines are hard sphere umbrella sampling results for comparison (as previously shown in Fig. 3.11)

measured nucleus sizes. This could have occurred due if the fit in Fig. 5.9 erred on the side of underestimating the nucleus sizes. Future work could attempt to improve this by taking more samples and obtaining a better fit in Fig. 5.9.

We can use the CNT form of the nucleation barrier to estimate the barrier heights. This form is given in equation 5.4, where ρ_s is the number density of the solid, $\Delta\mu$ is the chemical potential difference between the liquid and the solid, and γ is the liquid–solid surface tension.

$$\delta G = \tfrac{4}{3}\pi R^3 \rho_s \Delta\mu + 4\pi R^2 \gamma \tag{5.4}$$

ρ_s and $\Delta\mu$ are taken from Auer and Frenkel[25], using $\kappa = 5$ and $\beta\epsilon = 20$, which gives coexistence lines reasonably close to those measured in these experiments. γ is taken as a free fitting parameter. We perform the fit for the $\Phi_{prep} = 0.30$ data for all clusters $n < 40$, and for the $\Phi_{prep} = 0.30, 0.32$ data for clusters $n < 50$. This avoids fitting to the very noisy regions which are dominated by small fluctuations in the counted number of clusters. We found that reasonable CNT fits could only be obtained after scaling the experimental nucleation barriers to coincide with the simulation n when $\beta\delta G(n) = 13$. These changes mean the final barrier heights are purely indicative. Our

Φ_{prep}	$\beta\delta G(max)$
0.30	21.6
0.31	20.9
0.32	19.7

Table 5.2: Estimated barrier heights for our experimental samples.

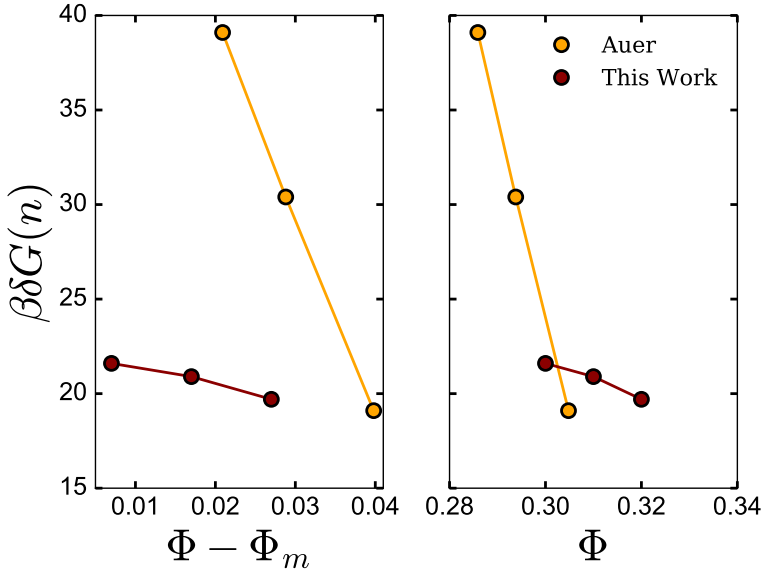

Figure 5.14: A comparison of our nucleation barrier heights and those of Frenkel and Auer[25] for similar Yukawa parameters $\kappa = 5, \beta\epsilon = 20$. **Left.** Barrier heights with the distance from the freezing line. Ref[25] does not give a freezing line for their system, instead we take the freezing line from ref[208] for the same set of parameters. **Right.** Barrier heights with the raw liquid volume fraction.

results for γ were clustered around $0.16 k_B T/\sigma^2$. This result is in line with literature measurements for hard spheres, which range between $0.11 k_B T/\sigma^2$ and $0.78 k_B T/\sigma^2$[32,92,105,212–214]. We show the final barrier heights in Table 5.2.

As shown in Fig 5.14, we do not observe the very sharp dependence of the nucleation barrier on the volume fraction, as we would expect in both the hard sphere case[88] and in the Yukawa case[25]. This is the same result as observed by Bonn *et al.*, who found little dependence of the nucleation barrier on the local volume fraction. However, this measurement goes further, indicating that the barrier does not depend strongly on the global volume fraction either. We have therefore failed to resolve the nucleation problem, even using very small particles which should be almost unaffected by sedimentation, and using a

technique which is completely independent of the original scattering results.

5.7 CONCLUSION

In this section, a novel method for taking and analysing confocal data of crystallising systems has been developed. This real space-reciprocal space technique allows for far larger systems to be analysed, and therefore much rarer events can be studied than was previously possible[32,132] We also adapt the original scattering methods for establishing precise volume fractions to confocal methods, and use this technique to measure volume fractions within the coexistence region with an error of around 0.25%. This is much more precise than was previously believed possible[63,88].

These techniques have been applied to studying the nucleation barriers of a colloidal system at a variety of supercooled volume fractions. We find similar results to previous scattering and real-space measurements, with the height of the nucleation barrier depending far more weakly on the supersaturation than it measured in simulations. However, the particles used were not true hard spheres, and exhibit noticeable polydispersity and charging, which will both affect the nucleation rates. We can therefore not clearly compare these results to the simulation work on hard spheres, and the simulation work on weakly charged spheres is less abundant, meaning a true like for like comparison is difficult. Further work should use more monodisperse, less charged colloids, which could be adequately compared with the hard sphere simulations.

6

CONCLUSION

The aim of this thesis has been to address the huge gap in hard sphere nucleation rate densities between experiments and simulations. This gap has been outstanding for nearly 20 years, since the original umbrella sampling work of Auer and Frenkel[105]. The size of the gap (13 orders of magnitude at worst) has been described as the second worse outstanding discrepancy in physics[112]. This work has failed to resolve the discrepancy, but it has shed light on several potential causes that have been discussed in the literature.

6.1 THE EFFECT OF SEDIMENTATION ON THE STRUCTURE OF HARD SPHERE FLUIDS

Our first results chapter probed the local structure of hard sphere fluids on inducing sedimentation. The small amount of sedimentation that exists in experiment has been discussed as a promising avenue for explaining the nucleation discrepancy[88]. In fact, sedimentation is the only clear experimental imperfection which remains outstanding. Charge[25], polydispersity[29], steric softness[114], hydrodynamics[121] and simulation methodology[99] have all been tested and fail to resolve the discrepancy.

We performed carefully controlled, particle resolved experiments to test whether sedimentation could explain the nucleation rate density gap. Inspired by the long tradition of examining five-fold symmetry when considering crystallisation, we used the Topological Cluster Classification to measure the population of the defective icosahedra structure. We saw a pronounced decline in populations when sedimentation was induced. By running experiments in which the particles moved both upwards as well as downwards, we isolated the cause of this effect to the sedimentation.

We then moved to determine the importance of the population decline on the nucleation rate density. By matching the decline seen in our experiments to biased simulations, we could prepare simulation configurations that had the same populations of five-fold symmetric structures as our experiments. Umbrella sampling simulations (performed by Dr John Russo) gave the nucleation barriers for these biased simulations.

We saw a huge decline in the nucleation barriers. This decline was enough to account for around five orders of magnitude in the nucleation discrepancy, essentially resolving the discrepancy for the weakly sedimenting experiments. However, our experiments were run at a high Peclét number, 1.5. This meant that the decrease in barrier height in the literature experiments would not be as large as that we measured, and so the discrepancy remains. Sedimentation remains a highly promising avenue for future work, and we are currently running simulations uniting hydrodynamics and sedimentation in order to understand if it may be coupling to a parameter other than five fold symmetry.

6.2 DENSITY FLUCTUATIONS IN EXPERIMENTAL HARD SPHERE FLUIDS

Following on from the work previously described, we attempted to measure the effect of the sedimentation on the density fluctuations in the hard sphere liquid. We developed a measurement technique which found the standard deviation of the local densities of each particle as a proxy for the density fluctuations. Very little change between density matched and sedimenting experiments was seen. However, we found a substantial and surprising increase in fluctuations in all of our experiments in comparison to simulations. This was itself a possible explanation for the nucleation rate gap, and so we attempted to isolate the cause.

We first studied a variety of experimental imperfections which might have been creating the anomalous fluctuations. These included imaging parameters such as the laser power and image averaging, changes in the chemistry such as particle charge and polydispersity, and problems with our simulations, such as errors handling particles at the boundary or a finite size effect. None of these proved explanatory. It was only after attempting to match the fluctuations in quasi-2d that we turned our attention to the particle tracking.

Particle tracking is arguably the most crucial step in confocal experiments, as it is the bridge from the experimental output, the images, to the analysable data. After carefully simulating images that match real confocal images, we were able to show that the tracking alone is responsible for the enhanced fluctuations. This means that the tracking was substantially affecting our measured configurations, in ways which were invisible to global order parameters like the radial distribution function and even the local analysis of the TCC. Further work could explore the exact mechanism of the fluctuations, this is now

possible as simulated images allow for the comparison between the true particle positions and those identified by the tracking.

6.3 MEASURING NUCLEATION RATE DENSITIES IN CONFOCAL MICROSCOPY

Almost all previous experimental work on the nucleation rate density discrepancy was done with scattering techniques. These are incredibly powerful techniques, in that they are able to average over an entire sample which contains many billions of particles. On the other hand, they are hampered by having to infer information about complex processes like nucleation from quite crude measurements, like the heights and widths of Bragg peaks. Particle resolved studies allow for a much more detailed examination of the crystal nuclei themselves, and this has shed light on aspects of nucleation that are off limits to scattering[32,38].

Unfortunately, the limitations of particle tracking make measurements of nucleation rate densities very difficult when the formation of a crystal nucleus becomes a truly rare event. This is also the crucial region, where the largest part of the discrepancy exists. We therefore developed an entirely new technique to take measurements of nucleation rate densities, returning to a reciprocal-space technique, which nevertheless gives detailed data about real-space quantities. In doing so, we were able to increase the number of particles measured by several orders of magnitude in comparison to conventional particle tracking techniques. This in turn allowed for the first measurement of nucleation rate barriers where the discrepancy exists, using a methodology completely independent from that of the scattering experiments.

Unfortunately, we found very similar results to previous experimental work. We measured only a very weak dependence of the nucleation barrier height on the volume fraction. Future work could attempt to repeat this work on particles which have an interaction potential that is closer to hard spheres

BIBLIOGRAPHY

1. Chaikin, P. M. & Lubensky, T. C. *Principles of Condensed Matter Physics* (Cambridge University Press, 1995).
2. Dyre, J. C. Simple liquids' quasiuniversality and the hard-sphere paradigm. *Journal of Physics: Condensed Matter* **28,** 323001 (2016).
3. Verlet, L. Computer "Experiments" on Classical Fluids. II. Equilibrium Correlation Functions. *Phys. Rev.* **165,** 201–214 (1 1968).
4. López-Flores, L., Ruíz-Estrada, H., Chávez-Páez, M. & Medina-Noyola, M. Dynamic equivalences in the hard-sphere dynamic universality class. *Phys. Rev. E* **88,** 042301 (4 2013).
5. Hansen, J.-P. & Macdonald, I. *Theory of Simple Liquids* (Academic, London, 1976).
6. Hoover, W. & Ree, F. Melting Transition and Communal Entropy for Hard Spheres. *J. Chem. Phys.* **46,** 3609–3617 (1958).
7. Davidchack, R. L. & Laird, B. B. Simulation of the hard-sphere crystal–melt interface. *The Journal of Chemical Physics* **108,** 9452–9462 (1998).
8. Noya, E, Vega, C. & de Miguel, E. Determination of the melting point of hard spheres from direct coexistence simulation methods. *The Journal of chemical physics* **128,** 154507 (2008).
9. Palberg, T., Bartsch, E., Beyer, R., Hofmann, M., Lorenz, N., Marquis, J., Niu, R. & Okubo, T. To make a glass—avoid the crystal. *Journal of Statistical Mechanics: Theory and Experiment* **2016,** 074007 (2016).
10. Dullien, F. *Porous Media (Second Edition)* (ed DULLIEN, F.) Second Edition, 5 –115 (Academic Press, San Diego, 1992). ISBN: 978-0-12-223651-8.
11. Berryman, J. G. Random close packing of hard spheres and disks. *Phys. Rev. A* **27,** 1053–1061 (2 1983).
12. Scott, G. & Kilgour, D. The density of random close packing of spheres. *Journal of Physics D Applied Physics* **2,** 863–866 (1969).
13. Lubensky, T. Soft condensed matter physics. *Solid State Communications* **102.** Highlights in Condensed Matter Physics and Materials Science, 187 –197. ISSN: 0038-1098 (1997).
14. *Phase transformations in solids* (eds Smoluchowski, R., Mayer, J. & Weyl, W.) (J. Wiley and Sons, Inc., New York, 1952).

15. Alder, B. & Wainwright, T. Phase Transition for a Hard Sphere System. *J. Phys. Chem.* **27,** 1208–1209 (1957).

16. Wood, W. W. & Jacobson, J. D. Preliminary Results from a Recalculation of the Monte Carlo Equation of State of Hard Spheres. *J. Chem. Phys.* **27,** 1207–1208 (1957).

17. Percus, J. K. *The many-body problem : proceedings of the Symposium on the many-body problem held at Stevens institute of technology, Hoboken, New Jersey, January 28-29, 1957* (New York : Interscience, 1963).

18. Mareschal, M. Early years of Computational Statistical Mechanics. *The European Physical Journal H* **43,** 293–302 (2018).

19. Oxtoby, D. W. Nucleation of First-Order Phase Transitions. *Accounts of Chemical Research* **31,** 91–97 (1998).

20. Debenedetti, P. G. *Metastable Liquids Concepts and Principles* (Princeton University Press, Princeton, 1996).

21. Laaksonen, A., Talanquer, V. & Oxtoby, D. W. Nucleation: Measurements, Theory, and Atmospheric Applications. *Annual Review of Physical Chemistry* **46,** 489–524 (1995).

22. Sosso, G. C., Chen, J., Cox, S. J., Fitzner, M., Pedevilla, P., Zen, A. & Michaelides, A. Crystal Nucleation in Liquids: Open Questions and Future Challenges in Molecular Dynamics Simulations. *Chemical Reviews* **116,** 7078–7116 (2016).

23. (auth.), V. K. *Nucleation Theory* 1st ed. ISBN: 978-90-481-3642-1,978-90-481-3643-8 (Springer Netherlands, 2013).

24. Sear, R. P. Nucleation: theory and applications to protein solutions and colloidal suspensions. *J. Phys.: Condens. Matter* **19,** 033101 (2007).

25. Auer, S. & Frenkel, D. Crystallization of weakly charged colloidal spheres: a numerical study. *J. Phys.: Condens. Matter* **14,** 7667–7680 (2002).

26. Sear, R. P. On the Interpretation of Quantitative Experimental Data on Nucleation Rates Using Classical Nucleation Theory. *The Journal of Physical Chemistry B* **110.** PMID: 17064163, 21944–21949 (2006).

27. Kelton, K. (eds Ehrenreich, H. & Turnbull, D.) 75 –177 (Academic Press, 1991).

28. Russo, J. & Tanaka, H. Nonclassical pathways of crystallization in colloidal systems. *MRS Bulletin* **41,** 369–374 (2016).

29. Auer, S. & Frenkel, D. Suppression of crystal nucleation in polydisperse colloids due to increase of the surface free energy. *Nature* **413,** 711–713 (2001).

30. Gránásy, L. & Pusztai, T. Diffuse interface analysis of crystal nucleation in hard-sphere liquid. *The Journal of Chemical Physics* **117,** 10121–10124 (2002).

31. Hickey, J. & L'Heureux, I. Classical nucleation theory with a radius-dependent surface tension: A two-dimensional lattice-gas automata model. *Phys. Rev. E* **87,** 022406 (2 2013).

32. Gasser, U., Weeks, E. R., Schofield, A., Pusey, P. N. & Weitz, D. A. Real-space imaging of nucleaction and growth in colloidal crystallization. *Science* **292,** 258–262 (2001).

33. Prestipino, S., Laio, A. & Tosatti, E. Shape and area fluctuation effects on nucleation theory. *The Journal of Chemical Physics* **140,** 094501 (2014).

34. Schilling, T., Schoepe, H. J., Oettel, M., Opletal, G. & Snook, I. Precursor-mediated crystallization process in suspensions of hard spheres. *Phys. Rev. Lett.* **105,** 025701 (2010).

35. Kawasaki, T. & Tanaka, H. Formation of a crystal nucleus from liquid. *Proc. Nat. Acad. Sci.* **107,** 14036–14041 (2010).

36. Russo, J. & Tanaka, H. The microscopic pathway to crystallization in supercooled liquids. *Sci. Rep.* **2,** 505 (2012).

37. Berryman, J. T., Anwar, M., Dorosz, S. & Schilling, T. The early crystal nucleation process in hard spheres shows synchronised ordering and densification. *The Journal of Chemical Physics* **145,** 211901 (2016).

38. Tan, P., Xu, N. & Xu, L. Visualizing kinetic pathways of homogeneous nucleation in colloidal crystallization. *Nature Physics* **10,** 73 (2013).

39. Gránásy, L. & Tóth, G. Crystallization: Colloidal suspense. *Nat Phys* **10,** 12–13 (2014).

40. Evans, R. The nature of the liquid-vapour interface and other topics in the statistical mechanics of non-uniform, classical fluids. *Adv. Phys.* **28,** 143–200 (1979).

41. Oxtoby, D. W. & Evans, R. Nonclassical nucleation theory for the gas–liquid transition. *The Journal of Chemical Physics* **89,** 7521–7530 (1988).

42. Zeng, X. C. & Oxtoby, D. W. Gas–liquid nucleation in Lennard-Jones fluids. *The Journal of Chemical Physics* **94,** 4472–4478 (1991).

43. Talanquer, V. & Oxtoby, D. W. Dynamical density functional theory of gas–liquid nucleation. *The Journal of Chemical Physics* **100,** 5190–5200 (1994).

44. Feynman, R. P. *Statistical Mechanics* (Westview press, 1998).

45. Chandler, D. *Introduction to Modern Statistical Mechanics* (Oxford University Press, 1987).

46. Frisch, H. L. & Lebowitz, J. L. *Equilibrium Theory of Classical Fluids* (W.A. Benjamin, Inc., 1964).

47. De Haro, M. L. & Robles, M. The structure factor and equation of state of hard-sphere fluids. *Journal of Physics: Condensed Matter* **16,** S2089–S2096 (2004).

48. Werthiem, M. S. Exact solution of the Percus-Yevick integral equation for hard spheres. *Phys. Rev.* **10,** 321–322 (1963).

49. Wertheim, M. S. Analytic Solution of the PercusYevick Equation. *Journal of Mathematical Physics* **5,** 643–651 (1964).

50. Tanemura, M., Hiwatari, Y., Matsuda, H., Ogawa, T., Ogita, N. & Ueda, A. Geometrical Analysis of Crystallization of the Soft-Core Model. *Prog. Theo. Phys.* **58,** 1079–1095. ISSN: 0033-068X (1977).

51. Honeycutt, J. D. & Andersen, H. C. Molecular dynamics study of melting and freezing of small Lennard-Jones clusters. *J. Phys. Chem.* **91,** 4950–4963 (1987).

52. Steinhardt, P. J., Nelson, D. R. & Ronchetti, M. Bond-Orientational Order In Liquids And Glasses. *Phys. Rev. B* **28,** 784–805 (1983).

53. Malins, A., Williams, S. R., Eggers, J. & Royall, C. P. Identification of Structure in Condensed Matter with the Topological Cluster Classification. *J. Chem. Phys.* **139,** 234506 (2013).

54. Malins, A. *A Structural Approach to Glassy Systems* PhD thesis (University of Bristol, 2013).

55. Franzblau, D. S. Computation of ring statistics for network models of solids. *Phys. Rev. B* **44,** 4925–4930 (1991).

56. Williams, S. R. Topological Classification of Clusters in Condensed Phases. *ArXiV:cond-mat,* 0705.0203 (2007).

57. Malins, A., Eggers, J., Tanaka, H. & Royall, C. P. Lifetimes and lengthscales of Structural Motifs in a Model Glassformer. *Faraday Discussions* **167,** 405–423 (2013).

58. Meissner, M., Dong, J., Eggers, J., Seddon, A. M. & Royall, C. P. Oil-in-water microfluidics on the colloidal scale: new routes to self-assembly and glassy packings. *Soft Matter* **13,** 788–794 (4 2017).

59. Razali, A., Fullerton, C. J., Turci, F., Hallett, J. E., Jack, R. L. & Royall, C. P. Effects of vertical confinement on gelation and sedimentation of colloids. *Soft Matter* **13,** 3230–3239 (17 2017).

60. Hallett, J. E. J. E., Turci, F. & Royall, C. P. Local structure in deeply supercooled liquids exhibits growing lengthscales and dynamical correlations. *accepted by Nature Comms.* (2018).

61. Taffs, J. & Patrick Royall, C. The role of fivefold symmetry in suppressing crystallization. *Nature Communications* **7,** 13225 (2016).

62. Taffs, J., Williams, S. R., Tanaka, H. & Royall, C. P. Structure and kinetics in the freezing of nearly hard spheres. *Soft Matter* **9,** 297–305 (2013).

63. Poon, W. C. K., Weeks, E. R. & Royall, C. P. On measuring colloidal volume fractions. *Soft Matter* **8,** 21–30 (2012).

64. Burwell, R. L. *Manual of Symbols and Terminology for Physicochemical Quantities and Units Appendix II* (ed Burwell, R. L.) 74 –86 (Pergamon, 1976). ISBN: 978-0-08-021360-6.

65. Lewis, R. J. & Hawley, G. G. *Hawley's Condensed Chemical Dictionary.* (2007).

66. Hiemenz, P & Rajagopalan, R. *Principles of Colloid and Surface Chemistry, Third Edition* (CRC Press, 1997).

67. Perrin, J. *Les Atomes* (Felix Alcan, 1913).

68. Poon, W. C. K. Colloids as big atoms: the genesis of a paradigm. *Journal of Physics A: Mathematical and Theoretical* **49,** 401001 (2016).

69. McMillan, W. G. & Mayer, J. E. The Statistical Thermodynamics of Multicomponent Systems. *The Journal of Chemical Physics* **13,** 276–305 (1945).

70. Kirkwood, J. G. & Buff, F. P. The Statistical Mechanical Theory of Solutions. I. *The Journal of Chemical Physics* **19,** 774–777 (1951).

71. Zaccarelli, E. Colloidal Gels: Equilibrium and non-equilibrium routes. *J. Phys.: Condens. Matter* **19,** 323101 (2007).

72. Poon, W. Colloidal glasses. English. *Mrs bulletin* **29,** 96–99. ISSN: 0883-7694 (2004).

73. Yethiraj, A. Tunable colloids: control of colloidal phase transitions with tunable interactions. *Soft Matter* **3,** 1099–1115 (9 2007).

74. Pusey, P. & van Megen, W. Phase behaviour of concentrated suspensions of nearly hard colloidal spheres. *Nature* **320,** 340 (1986).

75. Mahajan, S. *Encyclopedia of Materials: Science and Technology* (Pergamon, 2001).

76. Royall, C. P., Poon, W. C. K. & Weeks, E. R. In search of colloidal hard spheres. *Soft Matter* **9,** 17–27 (2013).

77. Jones, R. A. L. *Soft Condensed Matter* (Oxford University Press, 2002).

78. Eastman, J. *Colloid Science* 36–49 (John Wiley and Sons, Ltd, 2009). ISBN: 9781444305395.

79. Ivlev, A., Löwen, H, Morfill, G. E. & Royall, C. P. *Complex Plasmas and Colloidal Dispersions: Particle-resolved Studies of Classical Liquids and Solids* (World Scientific Publishing Co., Singapore Scientific, 2012).

80. Lebovka, N. I. *Polyelectrolyte Complexes in the Dispersed and Solid State I: Principles and Theory* (ed Muller, M.) 57–96 (Springer Berlin Heidelberg, Berlin, Heidelberg, 2014). ISBN: 978-3-642-40734-5.

81. Royall, C., van Roij, R. & van Blaaderen, A. Extended sedimentation profiles in charged colloids: the gravitational length, entropy, and electrostatics. *J. Phys.: Condens. Matter* **17,** 2315–2326 (2005).

82. Waggett, F., Shafiq, M. D. & Bartlett, P. Failure of Debye-Hückel Screening in Low-Charge Colloidal Suspensions. *Colloids and Interfaces* **2.** ISSN: 2504-5377 (2018).

83. Vissers, T., Imhof, A., Carrique, F., Ángel V. Delgado & van Blaaderen, A. Electrophoresis of concentrated colloidal dispersions in low-polar solvents. *Journal of Colloid and Interface Science* **361,** 443 –455. ISSN: 0021-9797 (2011).

84. Van der Linden, M. N., Stiefelhagen, J. C. P., Heessels-Gürboğa, G., van der Hoeven, J. E. S., Elbers, N. A., Dijkstra, M. & van Blaaderen, A. Charging of Poly(methyl methacrylate) (PMMA) Colloids in Cyclohexyl Bromide: Locking, Size Dependence, and Particle Mixtures. *Langmuir* **31.** PMID: 25535669, 65–75 (2015).

85. Tadros, T. *Colloid Stability* 1–22 (John Wiley and Sons, Ltd, 2011). ISBN: 9783527631070.

86. Bryant, G., Williams, S. R., Qian, L., Snook, I. K., Perez, E. & Pincet, F. How hard is a colloidal 'hard-sphere' interaction? *Phys. Rev. E.* **66,** 060501 (2002).

87. Aastuen, D. J. W., Clark, N. A., Swindal, J. C. & Muzny, C. D. Determination of the colloidal crystal nucleation rate density. *Phase Transitions* **21,** 139–155 (1990).

88. Palberg, T. Crystallization kinetics of colloidal model suspensions: recent achievements and new perspectives. *J Phys.: Condens Matter* **26,** 333101 (2014).

89. Schätzel, K & Ackerson, B. J. Density Fluctuations during Crystallisation of Colloidal Suspensions. *Physical Review E* **48,** 3766, 3777 (1993).

90. He, Y., Ackerson, B. J., van Megen, W., Underwood, S. M. & Schätzel, K. Dynamics of crystallization in hard-sphere suspensions. *Phys. Rev. E* **54,** 5286–5297 (5 1996).

91. Sinn, C, Heymann, A, Stipp, A & Palberg, T. Solidification Kinetics of Hard Sphere Colloidal Suspensions. *Progress in Colloid and Polymer Science* **118,** 266–275 (2001).

92. Harland, J. L. & van Megen, W. Crystallization kinetics of suspensions of hard colloidal spheres. *Phys. Rev. E.* **55,** 3054–3067 (1997).

93. Iacopini, S., Palberg, T. & Schöpe, H. J. Ripening-dominated crystallization in polydisperse hard-sphere-like colloids. *Phys. Rev. E* **79,** 010601 (1 2009).

94. Heymann, A., Stipp, A. & Schätzel, K. Scaling in colloidal crystallization. *Il Nuovo Cimento D* **16,** 1149–1157. ISSN: 0392-6737 (1994).

95. Pusey, P. N., van Megen, W, Underwood, S. M., Bartlett, P & Ottewill, R. H. Colloidal fluids, crystals and glasses. *Journal of Physics: Condensed Matter* **2,** SA373–SA377 (1990).

96. Palberg, T. Crystallization kinetics of repulsive colloidal spheres. *J. Phys.: Condens. Matter* **11,** R323–R360 (1999).

97. Beyer, R., Franke, M., Schöpe, H. J., Bartsch, E. & Palberg, T. From nuclei to micro-structure in colloidal crystallization: Investigating intermediate length scales by small angle laser light scattering. *The Journal of Chemical Physics* **143,** 064903 (2015).

98. Van Duijneveldt, J. S. & Frenkel, D. Computer simulation study of free energy barriers in crystal nucleation. *The Journal of Chemical Physics* **96,** 4655–4668 (1992).

99. Filion, L., Ni, R., Frenkel, D. & Dijkstra, M. Simulation of nucleation in almost hard-sphere colloids: The discrepancy between experiment and simulation persists. *J. Chem. Phys* **134,** 134901 (2011).

100. Espinosa, J. R., Vega, C., Valeriani, C. & Sanz, E. Seeding approach to crystal nucleation. *The Journal of Chemical Physics* **144,** 034501 (2016).

101. Abrams, C. & Bussi, G. Enhanced Sampling in Molecular Dynamics Using Metadynamics, Replica-Exchange, and Temperature-Acceleration. *Entropy* **16,** 163–199 (2014).

102. Torrie, G. M. & Valleau, J. P. Monte Carlo free energy estimates using non-Boltzmann sampling: Application to the sub-critical Lennard-Jones fluid. *Chemical Physics Letters* **28,** 578 –581. ISSN: 0009-2614 (1974).

103. Auer, S. & Frenkel, D. Numerical prediction of absolute crystallization rates in hard-sphere colloids. *The Journal of Chemical Physics* **120,** 3015–3029 (2004).

104. Ten Wolde, P.-R., Ruiz-Montero, M. J. & Frenkel, D. Simulation of homogeneous crystal nucleation close to coexistence. *Faraday Discuss.* **104,** 93–110 (0 1996).

105. Auer, S. & Frenkel, D. Prediction of absolute crystal nucleation rate in hard-sphere colloids. *Nature* **409,** 1020–1023 (2001).

106. Allen, R. J., Warren, P. B. & ten Wolde, P. R. Sampling Rare Switching Events in Biochemical Networks. *Phys. Rev. Lett.* **94,** 018104 (1 2005).

107. Escobedo, F. A., Borrero, E. E. & Araque, J. C. Transition path sampling and forward flux sampling. Applications to biological systems. *Journal of Physics: Condensed Matter* **21,** 333101 (2009).

108. Allen, R. J., Valeriani, C. & ten Wolde, P. R. Forward flux sampling for rare event simulations. *J. Phys. Cond. Matt.* **21,** 463102 (2009).

109. Filion, L., Hermes, M., Ni, R. & Dijkstra, M. Crystal nucleation of hard spheres using molecular dynamics, umbrella sampling, and forward flux sampling: A comparison of simulation techniques. *The Journal of Chemical Physics* **133,** 244115 (2010).

110. Kawasaki, T. & Tanaka, H. Correction for Kawasaki and Tanaka, Formation of a crystal nucleus from liquid. *Proceedings of the National Academy of Sciences* **108,** 6335–6335. ISSN: 0027-8424 (2011).

111. Schilling, T., Dorosz, S., Schoepe, H. J. & Opletal, G. Crystallization in suspensions of hard spheres: a Monte Carlo and molecular dynamics simulation study. *J. Phys.: Condens. Matter* **23,** 194120 (2011).

112. Russo, J., Maggs, A. C., Bonn, D. & Tanaka, H. The interplay of sedimentation and crystallization in hard-sphere suspensions. *Soft Matter* **9,** 7369–7383 (30 2013).

113. Barrat, J. L., Gotze, W & Latz, A. The liquid-glass transition of the hard-sphere system. *Journal of Physics: Condensed Matter* **1,** 7163 (1989).

114. Auer, S., Poon, W. C.-K. & D., F. Phase behavior and crystallization kinetics of poly-12-hydroxystearic-coated polymethylmethacrylate colloids. *Phys. Rev. E* **67,** 020401(R) (2003).

115. Strivens, T. The shear thickening effect in concentrated dispersion systems. *Journal of Colloid and Interface Science* **57,** 476 –487. ISSN: 0021-9797 (1976).

116. Van Megen, W. & Underwood, S. M. The motions of particles in concentrated dispersions as observed by dynamic light scattering. *Langmuir* **6,** 35–42 (1990).

117. Ramaswamy, S. Issues in the statistical mechanics of steady sedimentation. *Advances in Physics* **50,** 297–341 (2001).

118. Rotne, J. & Prager, S. Variational Treatment of Hydrodynamic Interaction in Polymers. *The Journal of Chemical Physics* **50,** 4831–4837 (1969).

119. Satoh, A. *Introduction to Molecular-Microsimulation of Colloidal Dispersions* (2003).

120. Mizerski, K. A., Wajnryb, E., Zuk, P. J. & Szymczak, P. The Rotne-Prager-Yamakawa approximation for periodic systems in a shear flow. *The Journal of Chemical Physics* **140,** 184103 (2014).

121. Radu, M. & Schilling, T. Solvent hydrodynamics speed up crystal nucleation in suspensions of hard spheres. *EPL (Europhysics Letters)* **105,** 26001 (2014).

122. Auer, S. & Frenkel, D. Quantitative Prediction of Crystal-Nucleation Rates for Spherical Colloids: A Computational Approach. *Annu. Rev. Phys. Chem.* **55,** 333–61 (2004).

123. Chu, X. L., Nikolov, A. D. & Wasan, D. T. Effects of Particle Size and Polydispersity on the Depletion and Structural Forces in Colloidal Dispersions. *Langmuir* **12,** 5004–5010 (1996).

124. Jensen, G. V. & Barker, J. G. Effects of multiple scattering encountered for various small-angle scattering model functions. *Journal of Applied Crystallography* **51,** 1455–1466 (2018).

125. Kimmel, R. M. & Uhlmann, D. R. Effects of High Pressure on Amorphous Polymers: Densification of Polymethyl Methacrylate. *Journal of Applied Physics* **41,** 2917–2927 (1970).

126. Franke, M., Lederer, A. & Schoepe, H. J. Heterogeneous and homogeneous crystal nucleation in colloidal hard-sphere like microgels at low metastabilities. *Soft Matter* **7,** 11276 (2011).

127. Russell, W., Saville, D. & Schowalter, W. *Colloidal Dispersions* (Cambridge Univ. Press, Cambridge, 1989).

128. Franke, M. Thesis. *Thesis, Mainz* (2014).

129. *Colloidal dispersions* (ed W. B. Russel, D. A. S. . W. R. S.) (Cambridge University Press, Cambridge, UK, 1989).

130. Padding, J. T. & Louis, A. A. Hydrodynamic and Brownian fluctuations in sedimenting suspensions. *Phys. Rev. Lett.* **93,** 220601 (2004).

131. Iacopini, S., Palberg, T. & Schope, H. J. Crystallization kinetics of polydisperse hard-sphere-like microgel colloids: Ripening dominated crystal growth above melting. *J. Chem. Phys* **130,** 084502 (2009).

132. Ketzetzi, S., Russo, J. & Bonn, D. Crystal nucleation in sedimenting colloidal suspensions. *The Journal of Chemical Physics* **148,** 064901 (2018).

133. Pusey, P. N., Zaccarelli, E., Valeriani, C., Sanz, E., Poon, W. C. K. & Cates, M. E. Hard spheres: crystallization and glass formation. *Philosophical Transactions of the Royal Society A: Mathematical, Physical and Engineering Sciences* **367,** 4993–5011 (2009).

134. Fasolo, M. & Sollich, P. Equilibrium Phase Behavior of Polydisperse Hard Spheres. *Phys. Rev. Lett.* **91,** 068301 (6 2003).

135. Paulin, S. E. & Ackerson, B. J. Observation of a phase transition in the sedimentation velocity of hard spheres. *Phys. Rev. Lett.* **64,** 2663–2666 (22 1990).

136. Yethiraj, A & van Blaaderen, A. A colloidal model system with an inteaction tunable from hard sphere to soft and dipolar. *Nature* **421,** 513–517 (2003).

137. Bosma, G., Pathmamanoharan, C., de Hoog, E. H. A., Kegel, W. K., van Blaaderen, A. & Lekkerkerker, H. N. W. Preparation of monodisperse, fluorescent PMMA-latex colloids by dispersion polymerization. *J. Coll. Interf. Sci.* **245,** 292–300 (2002).

138. Wohlfarth, C. *Supplement to IV/6* (ed Lechner, M.) 465–465 (Springer Berlin Heidelberg, Berlin, Heidelberg, 2008). ISBN: 978-3-540-75506-7.

139. Heston, W. M., Hennelly, E. J. & Smyth, C. P. Dielectric Constants, Viscosities, Densities, Refractive Indices and Dipole Moment Calculations for Some Organic Halides1. *Journal of the American Chemical Society* **72,** 2071–2075 (1950).

140. Kurita, R. & Weeks, E. Experimental study of random close packed colloidal particles. *Physical review. E, Statistical, nonlinear, and soft matter physics* **82,** 011403 (2010).

141. Wouterse, A. *Random packing of colloids and granular matter* PhD thesis (Utrecht Universiteit, 2008).

142. Baranau, V. & Tallarek, U. Random-close packing limits for monodisperse and polydisperse hard spheres. *Soft Matter* **10,** 3826–3841 (21 2014).

143. Kodger, T., Guerra, R. & Sprakel, J. Precise colloids with tunable interactions for confocal microscopy. *Scientific Reports* **5,** 14635 (2015).

144. Prasad, V., Semwogerere, D. & Weeks, E. R. Confocal Microscopy of Colloids. *J. Phys.: Condens. Matter* **19,** 113102 (2007).

145. Minsky, M. Memoir on inventing the confocal scanning microscope. *Scanning* **10,** 128–138 (1988).

146. Paddock, S. W. Confocal Laser Scanning Microscopy. *BioTechniques* **27,** 992–1004 (1999).

147. Muller, M. Introduction to Confocal Fluorescence Microscopy. *Journal of The American Medical Informatics Association - J AMER MED INFORM ASSOC* (2002).

148. Crocker, J. C. & Grier, D. G. Methods of Digital Video Microscopy for Colloidal Studies. *J. Coll. Interf. Sci.* **179,** 298–310 (1995).

149. Crocker, J. C. & Grier, D. G. Microscopic measurement of the Pair Interaction Potential of Charge-Stablized Colloids. *Phys. Rev. Lett.* **81,** 352–355 (1994).

150. Leocmach, M. & Tanaka, H. A novel particle tracking method with individual particle size measurement and its application to ordering in glassy hard sphere colloids. *Soft Matter* **9,** 1447–1457 (2013).

151. Lowe, D. G. Distinctive Image Features from Scale-Invariant Keypoints. *International Journal of Computer Vision* **60,** 91–110 (2004).

152. Leocmach, M. *The colloid toolkit* 2015.

153. Turnbull, D. Kinetics of Heterogeneous Nucleation. *The Journal of Chemical Physics* **18,** 198–203 (1950).

154. Heni, M. & Lowen, H. Interfacial free energy of hard-sphere fluids and solids near a hard wall. *Phys. Rev. E.* **60,** 7057–7065 (2000).

155. Sandomirski, K., Walta, S., Dubbert, J., Allahyarov, E., Schofield, A., Löwen, H., Richtering, W. & Egelhaaf, S. Heterogeneous crystallization of hard and soft spheres near flat and curved walls. *The European Physical Journal Special Topics* **223,** 439–454. ISSN: 1951-6401 (2014).

156. Allahyarov, E., Sandomirski, K, Egelhaaf, S. & Löwen, H. Crystallization seeds favour crystallization only during initial growth. *Nature Communications* **6,** 7110 (2015).

157. Ziese, F, Maret, G & Gasser, U. Heterogeneous nucleation and crystal growth on curved surfaces observed by real-space imaging. *Journal of Physics: Condensed Matter* **25,** 375105 (2013).

158. Mampallil, D. & Eral, H. B. A review on suppression and utilization of the coffee-ring effect. *Advances in Colloid and Interface Science* **252,** 38 –54. ISSN: 0001-8686 (2018).

159. Gompper, G., Ihle, T., Kroll, D. & Winkler, R. Multi-particle collision dynamics: A particle-based mesoscale simulation approach to the hydrodynamics of complex fluids. *Advanced Computer Simulation Approaches for Soft Matter Sciences III,* 1–87 (2009).

160. Padding, J. T. & Louis, A. A. Interplay between hydrodynamic and Brownian fluctuations in sedimenting colloidal suspensions. *Phys. Rev. E* **77,** 011402 (2008).

161. Jenkins, M. C. & Egelhaaf, S. U. Confocal microscopy of colloidal particles: Towards reliable, optimum coordinates. *J. Coll. Interf. Sci.* **136,** 65–92 (2008).

162. Frank, F. C. Supercooling of Liquids. *Proc. R. Soc. A.* **215,** 43–46 (1952).

163. Nelson, D. R. *Defects and Geometry in Condensed Matter Physics* 392 (Cambridge University Press, 2002).

164. Bernal, J. D. A geometrical approach to the structure of liquids. *Nature* **183,** 141–147 (1959).

165. Finney, J. L. Random packings and the structure of simple liquids. I. The geometry of random close packings. *Proc. R. Soc. A* **319,** 479–493 (1970).

166. Karayiannis, N., Malshe, R., de Pablo, J. & Laso, M. Fivefold symmetry as an inhibitor to hard-sphere crystallization. *Physical review. E, Statistical, nonlinear, and soft matter physics* **83,** 061505 (2011).

167. Royall, C. P., Eggers, J., Furukawa, A. & Tanaka, H. Probing Colloidal Gels at Multiple Length Scales: The Role of Hydrodynamics. *Phys. Rev. Lett.* **114,** 258302 (2015).

168. Royall, C. P. & Kob, W. Locally favoured structures and dynamic length scales in a simple glass-former. *J. Stat. Mech.: Theory and Experiment,* 024001 (2017).

169. Royall, C. P., Malins, A., Dunleavy, A. J. & Pinney, R. Strong geometric frustration in model glassformers. *J. Non-Cryst. Solids* **407,** 34–43 (2014).

170. Peng, B., van der Wee, E., Imhof, A. & van Blaaderen, A. Synthesis of Monodisperse, Highly Cross-Linked, Fluorescent PMMA Particles by Dispersion Polymerization. *Langmuir* **28.** PMID: 22500982, 6776–6785 (2012).

171. Piazza, R. Settled and unsettled issues in particle settling. *Rep* **77,** 056602 (2014).

172. Leunissen, M. *Manipulating Colloids with Charge and Electric Fields* PhD thesis (Utrecht Universiteit, 2006).

173. Sedgwick, H., Egelhaaf, S. U. & Poon, W. C. K. Clusters and gels in systems of sticky particles. *J. Phys.: Condens. Matter* **16,** S4913–S4922 (2004).

174. Campbell, A. I., Anderson, V. J., van Duijneveldt, J. S. & Bartlett, P. Dynamical arrest in attractive colloids: The effect of long-range repulsion. *Phys. Rev. Lett.* **94,** 208301 (2005).

175. Royall, C. P., Leunissen, M. E., Hyninnen, A.-P., Dijkstra, M. & van Blaaderen, A. Re-entrant melting and freezing in a model system of charged colloids. *J. Chem. Phys.* **124,** 244706 (2006).

176. Royall, C. P., Leunissen, M. E. & van Blaaderen, A. A new colloidal model system to study long-range interactions quantitatively in real space. *J. Phys.: Condens. Matter* **15,** S3581–S3596 (2003).

177. Buzzaccaro, S., Tripodi, A., Rusconi, R., Vigolo, D. & Piazza, R. Kinetics of sedimentation in colloidal suspensions. *Journal of Physics: Condensed Matter* **20,** 494219 (2008).

178. Royall, C. P., Dzubiella, J., Schmidt, M. & van Blaaderen, A. Nonequilibrium Sedimentation of Colloids on the Particle Scale. *Phys. Rev. Lett.* **98,** 188304 (2007).

179. Hoogenboom, J. P., Vergeer, P. & van Blaaderen, A. A real-space analysis of colloidal crystallization in a gravitational field at a flat bottom wall. *The Journal of Chemical Physics* **119,** 3371–3383 (2003).

180. Davis, K. E., Russel, W. & Glantschnig, W. J. Disorder-to-Order Transition in Settling Suspensions of Colloidal Silica: X-ray Measurements. eng. *Science (New York, N.Y.)* **245.** ISSN: 0036-8075 (1989).

181. Segre, P., E., H. & Chaikin, P. Long-Range Correlations in Sedimentation. *Phys. Rev. Lett.* **79,** 2574–2577 (1997).

182. Guazzelli, E. Evolution of particle-velocity correlations in sedimentation. *Physics of Fluids* **13,** 1537–1540 (2001).

183. Snabre, P., Pouligny, B., Metayer, C. & Nadal, F. Size segregation and particle velocity fluctuations in settling concentrated suspensions. *Rheologica Acta* **48,** 855–870. ISSN: 1435-1528 (2009).

184. Guazzelli, E. & Hinch, J. Fluctuations and Instability in Sedimentation. *Annual Review of Fluid Mechanics* **43,** 97–116 (2011).

185. Tee, S.-Y., Mucha, P. J., Cipelletti, L., Manley, S., Brenner, M. P., Segre, P. N. & Weitz, D. A. Nonuniversal Velocity Fluctuations of Sedimenting Particles. *Phys. Rev. Lett.* **89,** 054501 (5 2002).

186. Brenner, M. P. Screening mechanisms in sedimentation. *Physics of Fluids* **11,** 754–772 (1999).

187. Fishman, R. S., Hill, E. F., Storsved, T. K. & Bierwagen, G. P. Density fluctuations in hard sphere systems. *Journal of Applied Physics* **79,** 729–735 (1996).

188. Bannerman, M. N., Sargant, R. & Lue, L. DynamO: A free O(N) general event-driven simulator. *J. Comp. Chem.* **32,** 3329–3338 (2011).

189. Fasolo, M. & Sollich, P. Fractionation effects in phase equilibria of polydisperse hard-sphere colloids. *Phys. Rev. E* **70,** 041410 (4 2004).

190. Kremer, K., Robbins, M. O. & Grest, G. S. Phase Diagram of Yukawa Systems: Model for Charge-Stabilized Colloids. *Phys. Rev. Lett.* **57,** 2694–2697 (21 1986).

191. Malins, A., Williams, S. R., Eggers, J., Tanaka, H. & Royall, C. P. Geometric frustration in small colloidal clusters. *J. Phys.: Condens. Matter* **21,** 425103 (2009).

192. Allan, D. B., Caswell, T., Keim, N. C. & van der Wel, C. M. trackpy: Trackpy v0.4 (Version v0.4). *Zenodo.*

193. Baumgartl, J. & Bechinger, C. On the limits of digital video microscopy. *Europhys. Lett.* **71,** 487–493 (2005).

194. Taffs, J., Malins, A, Williams, S. R. & Royall, C. P. A structural comparison of models of colloid-polymer mixtures. *J. Phys.: Condens. Matter* **22,** 104119 (2010).

195. Metropolis, N., Rosenbluth, A. W., Rosenbluth, M. N., Teller, A. H. & Teller, E. Equation of State Calculations by Fast Computing Machines. *The Journal of Chemical Physics* **21,** 1087–1092 (1953).

196. Dinsmore, A. D., Weeks, E. R., Prasad, V., Levitt, A. C. & Weitz, D. A. Three-dimensional confocal microscopy of colloids. *Appl. Opt.* **40,** 4152–4159 (2001).

197. Brandel, C. & ter Horst, J. H. Measuring induction times and crystal nucleation rates. *Faraday Discuss.* **179,** 199–214 (0 2015).

198. Bednarczyk, D., Mash, E. A., Aavula, B. R. & Wright, S. H. NBD-TMA: a novel fluorescent substrate of the peritubular organic cation transporter of renal proximal tubules. *Pflugers Archiv* **440,** 184–192 (2000).

199. Campbell, A. I. & Bartlett, P. Fluorescent hard-sphere colloids for confocal microscopy. *J. Coll. Interf. Sci.* **256,** 325–330 (2002).

200. Van der Walt, S., Schönberger, J. L., Nunez-Iglesias, J., Boulogne, F., Warner, J. D., Yager, N., Gouillart, E., Yu, T. & the scikit-image contributors. scikit-image: image processing in Python. *PeerJ* **2,** e453. ISSN: 2167-8359 (2014).

201. Jones, E., Oliphant, T., Peterson, P., *et al. SciPy: Open source scientific tools for Python* 2001.

202. Wadell, H. Volume, Shape, and Roundness of Quartz Particles. *The Journal of Geology* **43,** 250–280 (1935).

203. Plimpton, S. Fast Parallel Algorithms for Short-Range Molecular Dynamics. *J. Comp. Phys.* **117,** 1 –19. ISSN: 0021-9991 (1995).

204. Weeks, J. D., Chandler, D. & Andersen, H. C. Role of Repulsive Forces in Determining the Equilibrium Structure of Simple Liquids. *J. Chem. Phys.* **54,** 5237. ISSN: 00219606 (1971).

205. Barker, J. A. & Henderson, D. Perturbation Theory and Equation of State for Fluids. II. A Successful Theory of Liquids. *The Journal of Chemical Physics* **47,** 4714–4721 (1967).

206. Antonopoulou, E., Rohmann-Shaw, C. F., Sykes, T. C., Cayre, O. J., Hunter, T. N. & Jimack, P. K. Numerical and experimental analysis of the sedimentation of spherical colloidal suspensions under centrifugal force. *Physics of Fluids* **30,** 030702 (2018).

207. Zeberg-Mikkelsen, C. K., Baylaucq, A., Barrouhou, M. & Boned, C. The effect of stereoisomerism on dynamic viscosity: A study of cis-decalin and trans-decalin versus pressure and temperature. *Phys. Chem. Chem. Phys.* **5,** 1547–1551 (8 2003).

208. Hynninen, A. P. & Dijkstra, M. Phase diagrams of hard-core repulsive Yukawa particles. *Phys. Rev. E* **68,** 021407 (2003).

209. Trizac, E., Bocquet, L. & Aubouy, M. Simple approach for charge renormalization in highly charged macroions. *Phys. Rev. Lett.* **89,** 248301. ISSN: 1079-7114 (2002).

210. Trizac, E. & Levin, Y. Renormalized jellium model for charge-stabilized colloidal suspensions. *Phys. Rev. E* **69,** 031403 (3 2004).

211. Bocquet, L., Trizac, E. & Aubouy, M. Effective charge saturation in colloidal suspensions. *J. Chem. Phys.* **117,** 8138 (2002).

212. Laird, B. B. & Davidchack, R. L. Direct Calculation of the Crystal-Melt Interfacial Free Energy via Molecular Dynamics Computer Simulation. *The Journal of Physical Chemistry B* **109,** 17802–17812 (2005).

213. Davidchack, R. L. & Laird, B. B. Crystal Structure and Interaction Dependence of the Crystal-Melt Interfacial Free Energy. *Phys. Rev. Lett.* **94,** 086102 (8 2005).

214. Warshavsky, V. B. & Song, X. Fundamental-measure density functional theory study of the crystal-melt interface of the hard sphere system. *Phys. Rev. E* **73,** 031110 (3 2006).

ACKNOWLEDGMENTS

Thank you to the EPSRC for funding this work under grant code EP/M506473/1.

Thank you to Prof. Paddy Royall, my supervisor, for his continual support throughout this work. I was very lucky to have found such a caring and dedicated person to supervise me, both through my Master's degree and my PhD. I always left your office feeling buoyed, usually with a dozen papers to read and a clutch of new ideas to explore.

Thank you to Dr Francesco Turci, who consistently gave up large parts of his day to help me. This included discussions on the science, but also a great deal of help with programming. You've made me a better scientist and coder, thank you.

Thank you to Dr John Russo who was incredibly efficient in providing umbrella sampling results for Chapter 3.

Thanks to everyone in G39, who created a wonderful atmosphere in which to work. Three people are owed special thanks. Dr Ioatzin Rios de Anda helped me regularly with preparing and characterising my colloids. You're probably the most hardworking and competent person I know, thank you. Dr Peter Crowther provided a great deal of help with programming. Your sharp wit during group meetings and our conversations about non-scientific topics were a very welcome break, thank you. Joshua Robinson also helped me write code, and gave up time to clarify some finer points of statistical mechanics. Mostly though, I want to thank him for being a wonderful person.

Thank you to the amazing, generous people I've lived with throughout my PhD: Andreas, Sam, Leo, Rory, Ben, Marion, Alex and Dylan.

My parents have helped me in so many ways throughout my life, but I need to give them special thanks for their love and support throughout the final stages of writing this thesis. This might never have been finished without you. I love you both.

Finally, Ailsa, I always knew that I have a wonderful partner who will love me regardless of whether or not I have a doctorate. That was my greatest comfort throughout writing this. I love you.